

DISS. ETH NO. 24752

**INTERTWINED DEGREES OF FREEDOM IN
THE SERIES $\text{Nd}_{1-x}\text{Ce}_x\text{CoIn}_5$**

A thesis submitted to attain the degree of
DOCTOR OF SCIENCES of ETH ZURICH

(Dr. sc. ETH Zurich)

presented by

DANIEL GABRIEL MAZZONE

MSc ETH Physics
born on the 15.12.1988
citizen of Zermatt

accepted on the recommendation of

Prof. Dr. J. F. Mesot, examiner
Prof. Dr. M. Sigrist, co-examiner
Dr. J. L. Gavilano, co-examiner
Prof. Dr. M. Kenzelmann, co-examiner

2017

FÜR FABIENNE

ABSTRACT

Strongly correlated electron systems are quantum materials that reveal a deep intertwining between different electronic charge, orbital, spin and lattice degrees of freedom. The interaction among them can stabilize ground states that feature novel collective phenomena and that potentially contribute to the development of future technical applications, if they are understood on a microscopic level.

Particular complex quantum phenomena occur in systems containing rare earth elements, where the conduction electrons either screen or couple the magnetic moments of partially filled electronic f -states. The subtle balance between these energy scales yields strong electronic fluctuations that trigger a rich diversity of ground states, including unconventional superconductivity, antiferromagnetism or correlated insulating, metallic and topological protected states.

CeCoIn₅ is a model heavy-fermion d -wave superconductor that is believed to be mediated by magnetic fluctuations. Superconductivity is Pauli limited and features an additional phase at very low temperatures and large magnetic fields. This so-called Q-phase reveals magnetic order that only survives inside the superconducting condensate and directly couples to it.

Here, we show that the substitution of the local-moment element Nd for Ce in CeCoIn₅ tunes the hybridization between the $4f$ -electrons and the conduction band, such that the system is driven into an antiferromagnetic state arising from a small Fermi surface. We demonstrate that the Q-phase is stable under a small perturbation represented by a Nd doping of 5%. The high-field phase is separated from a low-field antiferromagnetic state via a magnetic instability that may originate from a field-induced quantum phase transition. Intriguingly, both phases display an identical magnetic symmetry, which prevents the emergence of a primary order parameter of magnetic nature in the Q-phase. The detailed investigation of the magnetic order in the two phases shows that the spin-density modulation directions are affected differently by a rotation of the magnetic field inside the tetragonal plane. While the anisotropic spin susceptibility in both phases arises from intertwined spin and orbital degrees of freedom, the coupling between superconductivity and magnetism is altered in the high-field state. These results suggest that the field-induced quantum phase transition triggers the emergence of an auxiliary superconducting order parameter in the Q-phase that couples magnetic order with d -wave superconductivity. In contrast, we suggest that magnetism and superconductivity are decoupled in the low-field phase. This conclusion is based on the investigation of the low-energy excitation spectrum of Nd_{0.05}Ce_{0.95}CoIn₅ at zero field. We observe magnetic fluctuations that are related to the superconducting condensate, but which are not affected by magnetic order. We suggest that the superconducting resonance consists of Ising-like fluctuations along the direction of static magnetic order.

ZUSAMMENFASSUNG

Stark korrelierte Elektronensysteme sind Quantenmaterialien, in welchen elektronische Ladungs-, orbitale, Spin- und strukturelle Freiheitsgrade intrinsisch verflochten sind. Die Wechselwirkungen zwischen diesen Parametern können Grundzustände stabilisieren, die neue kollektive Phänomene hervorrufen, welche wiederum für die Entwicklung zukünftiger technischer Anwendungen relevant sein könnten, falls sie auf einer mikroskopischen Ebene verstanden werden.

Besonders komplexe Quantumphänomene tauchen in Systemen mit seltenen Erden auf. In diesen Materialien schirmen die Leitungselektronen die magnetischen Momente der teilweise besetzten elektronischen f -Zuständen ab oder vermitteln diese. Das subtile Gleichgewicht dieser Energieskalen führt zu starken elektronischen Fluktuationen, die verschiedene Grundzustände, wie unkonventionelle Supraleitung, Antiferromagnetismus oder korrelierte isolatorische, metallische und topologisch geschützte Zustände hervorrufen können.

CeCoIn₅ ist ein Vorzeigesystem der schweren Fermionen mit d -Wellen Supraleitung, von welcher man glaubt, dass sie durch magnetische Fluktuationen induziert wird. Die supraleitende Phase ist Pauli limitiert und verfügt über einen zusätzlichen Zustand bei tiefen Temperaturen und hohen magnetischen Feldern. Diese sogenannte Q-Phase ist charakterisiert durch eine magnetische Ordnung, welche nur innerhalb des supraleitenden Kondensats überlebt und direkt an dieses koppelt.

Die vorliegende Arbeit zeigt, dass die Substitution des lokalen Momentes von Nd für Ce in CeCoIn₅ die Hybridisation zwischen den $4f$ -Elektronen und dem Leitungsband verändert, sodass das System in einen antiferromagnetischen Zustand getrieben wird, der sich in einer kleinen Fermioberfläche bildet. Wir demonstrieren, dass die Q-Phase stabil bleibt, wenn sie durch eine 5% Nd Konzentration gestört wird. Die Hochfeldphase wird durch eine magnetische Instabilität, welche durch einen Quantenphasenübergang hervorgerufen werden könnte, von einem antiferromagnetischen Zustand bei tiefen Feldern getrennt. Interessanterweise zeigen beide Phasen dieselbe magnetische Symmetrie, was einen primären magnetischen Ordnungsparameter am Ursprung der Q-Phase ausschliesst. Die detaillierte Untersuchung der magnetischen Ordnung beider Phasen offenbart, dass die Modulationsrichtungen der spin-dichte Welle von einem rotierenden magnetischen Feld in der tetragonalen Ebene unterschiedlich beeinflusst werden. Während die anisotropische Spin-suszeptibilität beider Phasen von einer Verflechtung von Spin und orbitalen Freiheitsgraden herrührt, verändert sich die Kopplung zwischen der Supraleitung und dem Magnetismus in der Hochfeldphase. Diese Resultate suggerieren, dass der feldinduzierte Quantenphasenübergang einen zusätzlichen supraleitenden Ordnungsparameter in der Q-Phase hervorruft, der die magnetische Ordnung mit der d -Wellen Supraleitung verbindet. Im Gegensatz dazu denken wir, dass Magnetismus und Supraleitung in der Tiefelfeldphase voneinander unabhängig bleiben. Dies schliessen wir aus der Untersuchung des Anregungsspektrums von Nd_{0.05}Ce_{0.95}CoIn₅ bei verschwindendem Feld, in welchem wir magnetische Fluktuationen beobachten, die zur Supraleitung gehören, aber nicht von der magnetischen Ordnung beeinflusst werden. Wir interpretieren dies als supraleitende Resonanz, welche ising'sche Fluktuationen aufweist, die entlang des statischen magnetischen Momentes polarisiert sind.

Contents

Contents	v
List of Figures	ix
List of Tables	xi
1 Introduction	1
2 Strongly Correlated Electron Systems	3
2.1 Magnetism	3
2.1.1 Localized Moment Magnetism	3
2.1.2 Itinerant Magnetism	5
2.2 Heavy-Fermion Systems	6
2.2.1 The Kondo Lattice	6
2.2.2 Competing Energy Scales and Quantum Criticality	8
2.2.3 The Global Phase Diagram of Heavy-Fermion Metals	10
2.3 Superconductivity	11
2.3.1 The Symmetry of the Superconducting Order Parameter	12
2.3.2 The Superconducting Pairing Interaction	13
2.3.3 The Superconducting Spin Resonance	15
2.3.4 The Question of a Microscopic Model for Unconventional Superconductivity	15
2.4 Interplay between Superconductivity and Magnetism	16
2.4.1 Conventional Superconductors	16
2.4.2 Heavy-Fermion Superconductors	17
2.4.3 Theoretical Models of Superconductivity-induced Magnetism	19
3 Neutron Scattering	23
3.1 Neutron Sources	23
3.2 Scattering Theory	24
3.2.1 Nuclear Scattering	24
3.2.2 Magnetic Scattering	26
3.3 Magnetic Structure Determination	28
3.3.1 Magnetic Moment and Wave-Vector	28
3.3.2 Representational Analysis	29

3.4	Absorption and Extinction	30
3.5	Experimental Techniques	31
3.5.1	Powder Diffraction	31
3.5.2	Single Crystal Diffraction	32
3.5.3	Inelastic Neutron Scattering	34
3.6	Sample Environment	35
3.6.1	Cryostats and Cryogenic Magnets	36
3.6.2	³ He Inserts and Dilution Refrigerators	36
4	The Pauli-Limited Heavy-Fermion <i>d</i>-wave Superconductor CeCoIn₅	39
4.1	Heavy-Fermion Properties	39
4.2	Pauli-Limited Superconductivity near a SDW Quantum Critical Point	41
4.3	The Q-phase of CeCoIn ₅	44
4.4	Pressurized and Substituted CeCoIn ₅	46
5	Intertwined Degrees of Freedom in the Series Nd_{1-x}Ce_xCoIn₅	49
5.1	Chemical Synthesis and Sample Quality	49
5.2	The Magnetic Phase Diagram of Nd _{1-x} Ce _x CoIn ₅ at Zero Field	52
5.2.1	Experimental Details	52
5.2.2	Ising-like Structure in Nd dominated Nd _{1-x} Ce _x CoIn ₅	53
5.2.3	Spin-Density Wave in Ce dominated Nd _{1-x} Ce _x CoIn ₅	54
5.2.4	Competing Energy Scales	57
5.2.5	Summary	59
5.3	The Q-phase in 5% Nd doped CeCoIn ₅	60
5.3.1	Macroscopic Measurements	60
5.3.2	Experimental Details	60
5.3.3	Two Distinct Magnetic Phases with Identical Symmetry inside the Superconducting Condensate	61
5.3.4	Evidence for a Novel Quantum Phase Transition	64
5.3.5	Summary	66
5.4	Distinct Domain Switching in Nd _{0.05} Ce _{0.95} CoIn ₅ at Low and High Magnetic Fields	67
5.4.1	Experimental Details	67
5.4.2	Domain Switching in the SDW-phase	67
5.4.3	Domain Switching in the Q-phase	70
5.4.4	Evidence for Spin-Orbit Interactions with Modified Magneto - Superconducting Coupling	71
5.4.5	A Spatially-Modulated Cooper Pair-Density Wave at the Origin of the Q-phase	73
5.4.6	Summary	73
5.5	The Spin Resonance in Nd _{0.05} Ce _{0.95} CoIn ₅	74
5.5.1	Experimental Details	74
5.5.2	Observation of the Spin Resonance	76
5.5.3	Decoupling of Magnetic Order and Antiferromagnetic Fluctuations	76
5.5.4	Summary	79

6 Conclusion and Outlook	81
Bibliography	85

List of Figures

2.1	Macroscopic Transport Properties of a Heavy-Fermion Metal	6
2.2	Microscopic Development of the Heavy-Fermion Ground State	7
2.3	Doniach Phase Diagram and Quantum Critical Phase Transition	9
2.4	Global Phase Diagramm of Heavy-Fermion Metals	10
2.5	Possible Gap Symmetries	13
2.6	Possible Superconducting Pairing Interactions	14
2.7	Interplay between Superconductivity and Magnetism in Heavy-Fermion Systems	18
2.8	Spatially-Modulated Superconducting Order Parameter	20
3.1	Powder and Four-Circle Diffractometer	32
3.2	Lifting-Counter Two-Axis Diffractometer and Triple-Axis Spectrometer	33
3.3	The Triple-Axis Spectrometer RITA-II	34
3.4	Cryostats, Cryogenic Magnets and Dilution Refrigerators	37
4.1	Crystal Structure and Fermi Surface	40
4.2	Angle-Resolved Photoemission Spectroscopy on CeCoIn ₅	41
4.3	<i>HT</i> -phase Diagram of CeCoIn ₅	42
4.4	The Q-phase of CeCoIn ₅	43
4.5	Switching of the Multicomponent Ground State in CeCoIn ₅	45
4.6	Pressure and Doping Dependence of CeCoIn ₅	46
5.1	<i>xT</i> -Phase Diagram of Nd _{1-x} Ce _x CoIn ₅	50
5.2	X-ray Powder Diffraction of Nd _{1-x} Ce _x CoIn ₅	51
5.3	Macroscopic Results of Nd _{1-x} Ce _x CoIn ₅	53
5.4	Neutron Powder Diffraction on Nd _{1-x} Ce _x CoIn ₅	54
5.5	Single Crystal Neutron Diffraction on Nd _{1-x} Ce _x CoIn ₅	56
5.6	Updated <i>xT</i> -Phase Diagram of Nd _{1-x} Ce _x CoIn ₅	58
5.7	Field dependent Upper Critical Field of Nd _{0.05} Ce _{0.95} CoIn ₅	61
5.8	Two distinct Magnetic Phases in Nd _{0.05} Ce _{0.95} CoIn ₅	62
5.9	A Field-induced Magnetic Instability inside the Superconducting Condensate .	63
5.10	Temperature dependent Magnetic Intensity in the Critical Region	64
5.11	<i>HT</i> -phase Diagram of Nd _{0.05} Ce _{0.95} CoIn ₅	65
5.12	Field dependent Intensity in the SDW-phase	68
5.13	Field-induced Domain Imbalance	68
5.14	Switching in the SDW-phase	69

5.15	Switching in the Q-phase	70
5.16	Domain Population in the Q-phase	71
5.17	Free Energy of the Spin-Orbit coupled Landau Model	72
5.18	Two Coexisting Magnetic Wave-Vectors	75
5.19	Spin Resonance of $\text{Nd}_{0.05}\text{Ce}_{0.95}\text{CoIn}_5$	77
5.20	Decoupling of Static Order and Antiferromagnetic Fluctuations	77

List of Tables

3.1	Coherent, Incoherent and Absorption Cross Sections of Nd, Ce, Co and In . . .	25
5.1	Representational Analysis of $\text{Nd}_{1-x}\text{Ce}_x\text{CoIn}_5$ with $\mathbf{Q}_{CM} = (1/2, 0, 1/2)$	55
5.2	Representational Analysis of $\text{Nd}_{1-x}\text{Ce}_x\text{CoIn}_5$ with $\mathbf{Q}_{ICM} = (0.45, 0.45, 1/2)$. .	57

Chapter 1

Introduction

The ground state of a thermodynamic system condenses into one of four different states of matter denoted as solids, liquids, gases and plasmas. These states can be modified by temperature, such as a solid material that melts into a liquid where it recovers the broken rotational and translational symmetry. Temperature-induced phase transitions are commonly referred as classical, because they are driven by thermal fluctuations [1, 2]. They are in contrast to phase transitions that arise from quantum mechanical fluctuations, which are governed by Heisenberg's uncertainty principle. These so-called quantum phase transitions appear in the zero temperature limit and are tuned by external parameters, such as pressure, chemical substitution or magnetic field.

Most quantum phase transitions occur in solids, as it is the state of matter that stabilizes at low temperatures. Here, the atoms can arrange in well-defined structures that are classified in two hundred thirty space groups, which obey certain symmetry properties [3]. Intriguingly, the interaction among the chemical elements in crystalline structures can trigger quantum phases including magnetism [4, 5], superconductivity [6], multiferroicity [7] and many more. These states yield macroscopic properties that may be relevant for future technical applications, but many of their fundamental properties are not understood yet and require detailed investigations.

Superconducting condensates are particularly interesting, because they feature a coherent ground state over macroscopic length scales and reveal zero electrical resistance [8]. Thus, superconducting wires have the potential to substantially decrease mankind's power consumption, if they were usable at room temperatures. Superconductivity, however, has not been observed above one hundred thirty Kelvins at ambient pressure yet [9]. A widespread intention among physicists is focussed on the microscopic understanding of these so-called unconventional superconductors. This insight may serve as basis to synthesize room temperature superconductors.

Unconventional superconductors are different from the well-understood phonon-driven superconducting phases. It is believed that they emerge from magnetic fluctuations, which are known to be particularly strong in the vicinity of quantum critical phase transitions [6, 10, 11]. The drawback of these high-temperature superconductors is that they reveal complex ground states, which are robust under macroscopic constraints. In fact, they are tunable only via chemical substitution, if commercially available magnetic field and pressure devices are used.

Fortunately, another family of compounds, so-called heavy-fermion superconductors, also feature superconducting condensates that are thought to be driven by magnetism [11]. These materials reveal energy scales that are much smaller than in high-temperature superconductors,

such that the ground state properties typically occur below a few Kelvins. In consequence, these compounds are highly tunable via magnetic field or pressure that is of the order of several Teslas or Gigapascals, respectively [2, 12, 13].

Neutron scattering is an excellent technique, by which the microscopic properties of a system can be investigated under extreme conditions [14–16]. The particle is charge neutral and features a magnetic moment. Thus, it cannot only easily penetrate complex sample environments, but it gives also access to the lattice and magnetic degrees of freedom on an atomic scale.

CeCoIn₅ is an exceptional heavy-fermion superconductor that can be synthesized in a very clean form and that is naturally placed in an environment of strong magnetic fluctuations [17–20]. Its ground state is highly susceptible to external perturbations and it reveals field-induced magnetic order that couples directly to superconductivity [21–25]. This cooperative magneto-superconducting state is in contrast to the generally observed competition between superconductivity and magnetism and it is unclear under which circumstances such phases occur. Moreover, despite the fact that this so-called Q-phase has been discussed for the last fifteen years, its microscopic origin remains elusive [25].

The intertwined degrees of freedom in the Q-phase may be decoupled when chemical substitution is used as an auxiliary tuning parameter. The field-induced phase, however, appears to be highly sensitive upon doping, and found to be suppressed at extremely small impurity concentrations [26]. Here, we study the effect of Nd substitution on the Ce-site of CeCoIn₅ that gives rise to a competition between localized moment magnetism and heavy-fermion properties [27]. The application of magnetic field supplementary to 5% Nd doping on the Ce-site demonstrates that the Q-phase remains stable under a small Nd-induced perturbation to the CeCoIn₅ ground state [28]. Thus, the series displays both a competition and a cooperation between superconductivity and magnetism under substitution and magnetic field, respectively.

The phase diagram of Nd_{0.05}Ce_{0.95}CoIn₅ against magnetic field and temperature further suggests a quantum phase transition inside the superconducting phase that is driven by fluctuations related to the superconducting condensate [28]. The meticulous investigation of the magnetic order for different magnetic field directions provides evidence for an intertwining among spin and orbital degrees of freedom and suggests the emergence of an auxiliary superconducting order parameter in the Q-phase [29]. Finally, we find evidence for magnetic fluctuations that are related to superconductivity, which may show fluctuations along the ordered magnetic moment at zero field [30].

The thesis is structured as follows: chapter 2 provides the background of localized and itinerant magnetism, heavy-fermion physics, quantum criticality, superconductivity and its interplay with magnetic order. The theoretical content of neutron scattering, instrumentation, magnetic structure determination as well as insight in the data analysis is given in chapter 3. Chapter 4 introduces the compound CeCoIn₅ and describes the state-of-the-art research in the field. The presentation and discussion of the studies on the series Nd_{1-x}Ce_xCoIn₅ is carried out in chapter 5. It is noted that these results are partly adopted from the manuscripts published in Ref. [28–30]. Finally, the thesis is summarized in chapter 6, where also possible future investigations are suggested.

Chapter 2

Strongly Correlated Electron Systems

A crystal defines a solid material consisting of $N \sim 10^{23}$ atoms or molecules that are arranged in a regular lattice in three dimensional space. The electronic Eigenstates are calculated by Bloch's theorem, which models the electrons as non-interacting quasiparticles in a static periodic potential [31]. Taking into account Pauli's exclusion principle, the chemical composition of the crystal and its space group symmetry [3], the approach leads to the description of the electronic band structure.

The concept shows that quantum mechanics can be used to illustrate collective phenomena in condensed matter physics and provides a microscopic description of fundamental material properties, such as metals or insulators. Band theory, however, ignores the coupling between different electronic (charge, spin and orbit) and/or lattice (phonon, defects and strain) degrees of freedom.

In strongly correlated electron systems a deep intertwining among these degrees of freedom leads to novel macroscopic properties that are not understood within band theory [32]. As examples, a strong electron-phonon coupling can stabilize charge-density wave order [33], crystal defects can cause Anderson localization [34] or the interaction among electrons can trigger magnetism [4, 5]. In order to disentangle the microscopic interactions of novel quantum phases with emergent macroscopic phenomena, active theoretical and experimental research is conducted on a multitude of strongly correlated electron systems. This includes unconventional superconductors [6], geometrically frustrated systems [35], quantum magnetic or topological insulators [36, 37], multiferroic materials [7] or heavy fermions [12, 23, 38–41].

2.1 MAGNETISM

Magnetic order in crystalline structures is a collective phenomenon that arises purely from quantum mechanical effects [5]. The magnetic interaction that is mediated among the electrons originates from orbital and/or spin degrees of freedom. Depending on the mobility of the magnetic moment carriers, both localized and itinerant electrons can give rise to magnetic order in metallic materials.

2.1.1 Localized Moment Magnetism.

The electrons in a partially filled atomic shell cause a non-vanishing total angular momentum $\mathbf{J} = \mathbf{L} + \mathbf{S}$ that is composed of the angular momentum, \mathbf{L} , and the spin degree of freedom

S. A single Ce^{3+} ion, for instance, contains an unpaired electron in the $4f^1$ -shell that yields $L = 3$, $S = 1/2$ and $J = L - S = 5/2^*$. The ground state consists of $2J + 1 = 6$ degenerate orbitals with an associated effective moment $\mu_{eff} = 2.54\mu_B$ that is calculated via [5]:

$$\mu_{eff} = g_J \mu_B \sqrt{J(J+1)}, \quad (2.1)$$

where $\mu_B = 9.27401 \cdot 10^{-24}$ J/T is the Bohr magneton. g_J describes the Landé splitting factor that is given by [5]:

$$g_J = \frac{3}{2} + \frac{S(S+1) - L(L+1)}{2J(J+1)}. \quad (2.2)$$

Localized moments that are embedded into a crystalline structure reveal a splitting of the $2J + 1$ fold degeneracy that arises from the influence of the crystalline environment [5]. The strength and spacial symmetry of this crystal field effect heavily depends on the structure and chemical composition of the considered material. The reduced local magnetic moments can still interact and may lead to collective static magnetic order below an ordering temperature T_N . It is noted that in a time-reversal symmetric system the ground state crystal field multiplet is at least doubly degenerate, when an odd number of electrons per magnetic ion is considered [42].

The exact form of the exchange interaction is influenced by several parameters including the distance between the magnetic ions, the crystal field anisotropy and the magnetic moment strength. A direct exchange occurs in materials, where the partially filled orbitals of two neighboring magnetic ions overlap. The Pauli exclusion principle and the Coulomb repulsion give rise to a local two-particle Hamiltonian $\hat{H}_{1,2} = -2J\hat{S}_1\hat{S}_2$ [5]. $\hat{S}_{1,2}$ are the two spin operators and J the isotropic exchange integral, which is ferromagnetic for $J > 0$ and antiferromagnetic for $J < 0$. In materials that contain rare-earth elements direct exchange can be neglected, because the spatial extend of the $4f$ orbitals is very limited.

Magnetic moments can also interact via their dipolar magnetic field, but in general this coupling is weak. It requires magnetic moments of the order of $\mu = 7\mu_B$ to realize $T_N \approx 0.65$ K when a distance $d \approx 4$ Å between two magnetic ions is assumed [43].

In most metallic systems consisting of rare-earth elements, localized moment magnetism mediated over large distances is driven by an indirect exchange process. A localized magnetic moment can polarize the surrounding conduction electrons, which yields an induced spin-density modulation that interacts with the nearest neighbor localized moment [5]. This so-called Rudermann-Kittel-Kasuya-Yoshida (RKKY) interaction is similar to superexchange in insulating materials and can trigger ordering temperatures up to room temperature [5, 43–46]. The exchange interaction can be written in the form of an Heisenberg-like[†] spin Hamiltonian with a spatially-dependent coupling term, $J(\mathbf{r})$, that is given by [5, 43]:

$$J_{RKKY}(\mathbf{r}) = 12\pi v |J|^2 N(E_F) \frac{\sin(2\mathbf{k}_F \mathbf{R}) - 2\mathbf{k}_F \mathbf{R} \cos(2\mathbf{k}_F \mathbf{R})}{(2\mathbf{k}_F \mathbf{R})^4} \quad (2.3)$$

Here, v denotes the number of conduction electrons per ion, $|J|$ is the exchange integral, $N(E_F)$ represents the density of states at the Fermi surface and \mathbf{k}_F is the Fermi wave-vector. The

*The quantum numbers are determined by Hund's rule, where S and L are maximized. In addition, spin-orbit coupling leads to $J = |L-S|$ and $L+S$ for less and more than half-filled shells, respectively [5].

[†]Similar to the direct exchange interaction $\hat{H} = -\sum_{i \neq j} J_{i,j} \hat{S}_i \hat{S}_j$.

equation reveals an effective exchange interaction that depends on the distance between two adjacent moments defining the sign of the magnetic interaction [44–46].

It is noted that other exchange interactions among localized moments can be relevant in insulating or non-centrosymmetric systems, such as superexchange, double exchange or the Dzaloshinskii-Moria interaction [5]. Since this thesis focuses on metallic materials, they are not considered here.

2.1.2 Itinerant Magnetism.

Magnetic order in metals can also arise via an instability of the Fermi liquid state [5, 47]. In certain cases it may be favorable for the material to align the electronic spins of the conduction band, because it can reduce the contribution of the Coulomb repulsion. In general, ferromagnetic metals, such as Fe, Co and Ni are distinguished from spin-density waves (SDWs), as found in Cr and Mn [47]. In both cases the Hamiltonian of the system is described by mobile electrons that feature a repulsive contact interaction, U , and that reads [47];

$$\hat{H} = \sum_{k,s} \epsilon_k \hat{c}_{k,s}^\dagger \hat{c}_{k,s} + U \int \hat{\rho}_\uparrow(\mathbf{r}) \delta(\mathbf{r} - \mathbf{r}') \hat{\rho}_\downarrow(\mathbf{r}') d^3 r d^3 r'. \quad (2.4)$$

The sum runs over all conduction electrons, where ϵ_k is the band energy at wave-vector \mathbf{k} in reciprocal space and $\hat{c}_{k,s}^\dagger$ ($\hat{c}_{k,s}$) the creation (annihilation) operator of a quasiparticle with spin s . $\hat{\rho}_s(\mathbf{r}) = \hat{\Psi}_s^\dagger(\mathbf{r}) \hat{\Psi}_s(\mathbf{r})$ is the electron density with spin s that is described by the electron field operators $\hat{\Psi}_s^\dagger(\mathbf{r}) = 1/\sqrt{V} \sum_{k,s} \hat{c}_{k,s}^\dagger \exp(-i\mathbf{k}\mathbf{r})$ and $\hat{\Psi}_s(\mathbf{r}) = 1/\sqrt{V} \sum_k \hat{c}_{k,s} \exp(i\mathbf{k}\mathbf{r})$, where V is the volume of the system.

The effective exchange interaction among the electrons induces a spin polarization that acts as a local field. The resulting spacial, \mathbf{q} , and frequency, ω , dependent spin susceptibility is derived in a random phase approximation approach [47]:

$$\chi(\mathbf{q}, \omega) = \frac{\chi_0(\mathbf{q}, \omega)}{1 - \frac{U}{2\mu_B} \chi_0(\mathbf{q}, \omega)}, \quad (2.5)$$

where $\chi_0(\mathbf{q}, \omega)$ is the bare susceptibility that is described by the Lindhard function [47]:

$$\chi_0(\mathbf{q}, \omega) = -\frac{g\mu_B^2}{V} \sum_k \frac{n_{\mathbf{k}+\mathbf{q},\uparrow} - n_{\mathbf{k},\downarrow}}{\epsilon_{\mathbf{k}+\mathbf{q}} - \epsilon_{\mathbf{k}} - \hbar\omega + i\hbar\eta}. \quad (2.6)$$

Here, g denotes the Landé splitting factor, $n_{k,s}$ are the number of electrons at the reciprocal wave-vector \mathbf{k} and spin s , \hbar is the reduced Planck constant $\hbar/2\pi = 1.055 \cdot 10^{-34}$ Js and the term $i\hbar\eta$ takes into account causality.

A magnetic instability is represented by the divergence of the susceptibility which appears at the generalized Stoner criterium $U/(2\mu_B^2)\chi_0(\mathbf{q}, \omega) = 1$. Itinerant ferromagnetic metals feature an instability at $\mathbf{q} = 0$, whereas an arbitrary wave-vector can be realized in SDWs that depends heavily on the band structure [47].

A crucial ingredient for the stabilization of a SDW at $\mathbf{q} = \mathbf{Q}$ is so-called nesting close to the Fermi surface that features an energy ϵ_F . The major contribution to $\chi_0(\mathbf{Q}, 0)$ arises from Fermi surface areas that satisfy $\epsilon_{\mathbf{k}+\mathbf{Q}} - \epsilon_F = \epsilon_F - \epsilon_{\mathbf{k}}$ [4, 47]. Below the ordering temperature T_N these parts of the Fermi surface gap[‡] and stabilize magnetic order along \mathbf{Q} . While a SDW-instability

[‡]The Néel temperature $T_N \propto \exp(-2/(UN(\epsilon_F)))$ depends on the Coulomb repulsion, U , and the density of states at the Fermi level $N(\epsilon_F)$. The gap size in the zero temperature limit reveals $|\Delta| = 2\epsilon_F \exp(-1/(UN(\epsilon_F)))$ [4, 47].

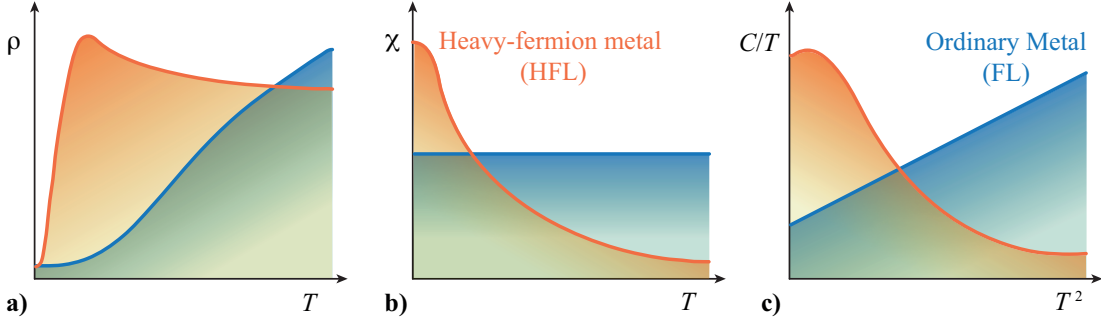


FIGURE 2.1: Macroscopic Transport Properties of a Heavy-Fermion Metal. Temperature dependent **a)** electrical resistivity $\rho(T)$, **b)** magnetic susceptibility $\chi(T)$ and **c)** electronic specific heat $C(T)$ of a HF metal (orange) when compared to the normal Fermi liquid behavior (blue). Taken from [24].

yields a metal-to-insulator transition in an one-dimensional material, the Fermi surface is only partly gapped in two or three dimensions.

2.2 HEAVY-FERMION SYSTEMS

Heavy-fermion (HF) systems are intermetallic compounds containing partially-filled f -bands that strongly interact with the conduction electrons [12]. The correlated ground state features a renormalized Fermi liquid behavior that is reflected in the macroscopic transport properties, such as electronic resistivity, magnetic susceptibility and electronic specific heat (see Fig. 2.1). The low-temperature attributes are directly related to the effective mass, m^* , which is two to three orders of magnitude larger in HF metals when compared to ordinary conductors [12, 47].

2.2.1 The Kondo Lattice.

The essence of the HF ground state is the Kondo effect that describes the antiferromagnetic exchange coupling of a single localized moment impurity, $\hat{\mathbf{S}}_f$, with the conduction electrons. It reads [48, 49]:

$$\hat{H} = \sum_{k,s} \varepsilon_k \hat{c}_{k,s}^\dagger \hat{c}_{k,s} - J \hat{\Psi}_s^\dagger(0) \boldsymbol{\sigma} \hat{\Psi}_s(0) \hat{\mathbf{S}}_f \quad (2.7)$$

with ε_k , $\hat{c}_{k,s}^{(\dagger)}$ and $\hat{\Psi}_s^{(\dagger)}(\mathbf{r})$ as defined in Eq. 2.4. $\boldsymbol{\sigma} = (\sigma_x, \sigma_y, \sigma_z)$ denotes the vector of Pauli matrices and $J < 0$ the antiferromagnetic contact interaction strength. It reveals a logarithmical temperature dependence that has a large impact on the low temperature properties of the system [48].

Below the single-ion Kondo temperature, $T_K \sim \exp(-1/|J|)$, the interaction between the impurity and the conduction electrons cannot longer be treated perturbatively [38]. The strong coupling triggers an effective screening of the localized moment via the conduction electrons and entangles them into a singlet state (see Fig. 2.2a).

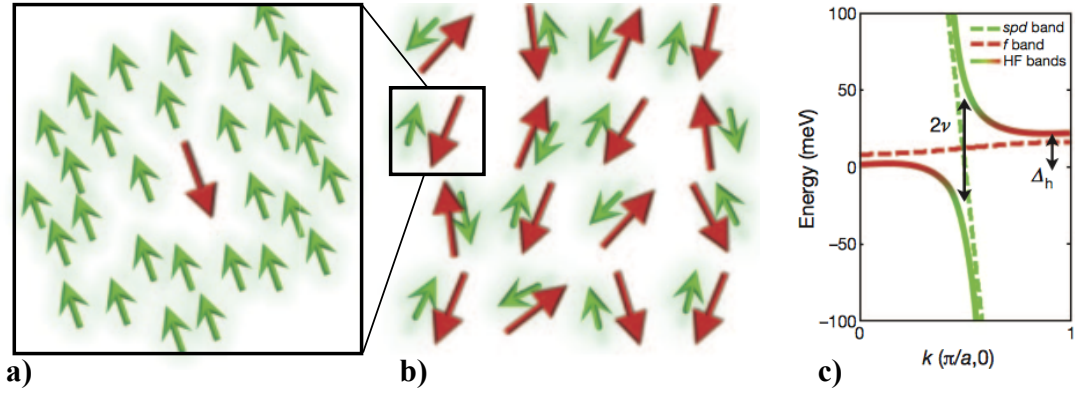


FIGURE 2.2: Microscopic Development of the Heavy-Fermion Ground State. **a)** Representation of a Kondo singlet and **b)** the Kondo lattice. **c)** Electronic bands from band theory (dashed lines) and hybridized bands (solid lines). Modified from [50].

In HF materials the partially filled f -shells are arranged in a periodic array that transforms the Kondo singlet into a lattice (see Fig. 2.2b) [38, 49]. The momentum conservation in the crystalline structure gives rise to a coherent ground state below a characteristic Kondo coherence temperature that equals several tens of Kelvins. The material features localized f -bands that actively contribute to the Fermi surface, modifying the band structure.

Figure 2.2c displays a flat f -band and a dispersing conduction band. While in the non-interacting band theory they remain separated, the Kondo interaction leads to a band hybridization with low-energy admixed quasiparticles [50]. The resulting f -band contribution to the Fermi surface gives rise to large effective masses that feedback into the macroscopic response (see Fig. 2.1). The avoided band crossing reconstructs the Fermi surface and opens a direct gap, $\nu \approx 20\text{-}30$ meV [51], that appears upon cooling the system below the Kondo coherence temperature. Kondo insulators, such as SmB_6 or YbB_6 , establish a fully gapped Fermi surface with an accompanying metal-to-insulator transition [52, 53], whereas in a HF metal, such as in CeCoIn_5 , the Fermi surface is only partly gapped [54].

Kondo insulators are currently heavily investigated, because spin-orbit coupling can cause a band inversion that stabilizes topological protected surface states [38, 52, 53]. In metals, a rich diversity of ground states, such as unconventional superconductivity and antiferromagnetism have been discovered since the investigation of the first HF material in 1975 [55]. This variety of possible ground states arises mainly from two reasons. Firstly, the Kondo interaction competes with the RKKY-exchange interaction [44–46]. Secondly, the low energy scales of these quantum ground states are tunable with external parameters, such as pressure, chemical substitution or magnetic field [2, 10, 12, 13].

It is noted that the description of the HF ground state reveals some similarities to the Hubbard model, which is often used to treat strongly correlated d -electron systems such as

transition-metal oxides [12]. In the isotropic limit it is given by [47]:

$$\hat{H} = -t \sum_{\langle i,j \rangle, s} (\hat{c}_{i,s}^\dagger \hat{c}_{j,s} + c.c.) + U \sum_i \hat{n}_{i,\uparrow} \hat{n}_{i,\downarrow}, \quad (2.8)$$

where, the sum runs over all nearest neighbor lattice sites i, j and spin configurations s . $c.c.$ is the complex conjugate, $\hat{c}_{i,s}^{(\dagger)}$ are the real-space field operators and $\hat{n}_{i,s} = \hat{c}_{i,s}^\dagger \hat{c}_{i,s}$ is the density operator. t denotes the hopping integral that enables the electron to move to adjacent sites and U is the contact Coulomb repulsion. The ratio U/t leads to either an insulating or a correlated metallic ground state. The difference between doped Mott insulators and HFs arises from the characterization of the correlated itinerant electrons [12]. While in HF materials the f -band couples to the conduction band, d -electrons in the transition-metal oxides become itinerant because of nearest neighbor interactions.

2.2.2 Competing Energy Scales and Quantum Criticality.

The Kondo interaction screens the magnetic moments via the surrounding conduction electrons, giving rise to the hybridized ground state [12, 57, 58]. The resulting contribution of the f -electrons to the conduction band forms a so-called large Fermi surface. In contrast, the RKKY interaction is an indirect exchange coupling between localized moments, where long-range magnetic order is established. In this case, the volume of the Fermi surface remains invariant and is denoted as small Fermi surface. The competition between these rivalry microscopic mechanisms yields a rich phase diagram that was studied first by Doniach in 1977 [59]. He considered a one dimensional insulating Kondo lattice, where the conduction band is replaced by a lattice of coupled spins. The characteristic temperatures, T_{RKKY} and T_K , depend on the coupling parameters, J , with $T_{RKKY} \sim J^2$ and $T_K \sim \exp(-1/|J|)$ for the RKKY and the Kondo[§] interaction, respectively. The interplay between both mechanisms results in a JT -phase diagram that is shown in Fig. 2.3a. Small J s yield a dominating RKKY interaction that triggers magnetic long-range order, whereas a heavy-fermion ground state is stabilized when the localized moments are strongly hybridized. At a critical interaction strength, J_c , long-range magnetic order and heavy-fermion properties are suppressed in a second order phase transition at zero temperature [59].

Although the Doniach phase diagram arises from an oversimplified model, it shows that the competition between the RKKY and Kondo interaction can trigger quantum phase transitions (QPTs) [1, 2]. They define phase transitions at zero temperature driven by quantum fluctuations that are governed by Heisenberg's uncertainty principle. These transitions are, thus, different from classical phase transitions at finite temperatures, which are induced by thermal fluctuations. However, they are partly described within the same theory.

Classical phase transitions are treated in Landau's theory that is based on the concept of spontaneous symmetry breaking at the second order phase transition [60]. The change of symmetry is illustrated by an order parameter with an associated correlation length ξ . While the order parameter is present in one phase, it is suppressed in the other one and emerges or collapses at the phase boundary where ξ diverges. The spatial fluctuations of the order parameter are described within a field theoretical ϕ^4 -model in d dimensions [61]. As an example, a stag-

[§]Here, the Kondo coherence temperature is set to the single ion Kondo temperature T_K . In general, this is not correct and an open theoretical question [49].

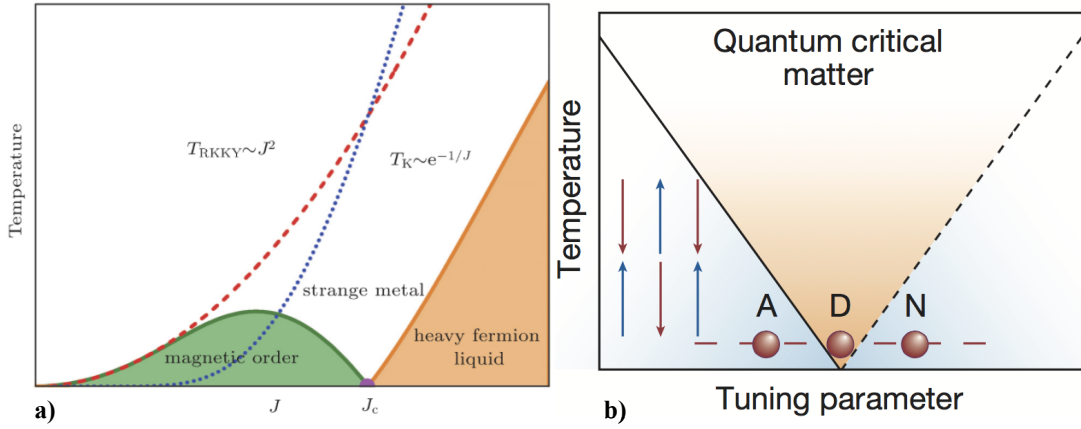


FIGURE 2.3: Doniach Phase Diagram and Quantum Critical Phase Transition. a) Schematic illustration of the Doniach phase diagram that treats the competition between Kondo and RKKY-exchange interaction. b) Schematic illustration of a quantum phase transition between a Fermi liquid (N) and an antiferromagnetically ordered state (A). A fan shaped region is established around the quantum critical point, where quantum fluctuations dominate the finite temperature properties. Taken from [2, 56].

gered magnetic field with diverging magnetic correlation length emerges as an order parameter at the phase boundary between a paramagnetic and an antiferromagnetically ordered phase.

The standard representation of a QPT follows the phenomenological model of a classical order parameter (see Fig. 2.3b) [1, 62, 63]. However, in addition to spatial fluctuations a critical slowing down is considered that is associated to imaginary time fluctuations. The correlation time, τ_0 , is connected via the critical dynamic exponent, z , to the correlation length $\tau_0 \propto \xi^z$. Depending on z the effective dimension in the ϕ^4 -model is modified to $d_{\text{eff}} = d + z$. For instance, it has been shown that an antiferromagnetic quantum critical instability features $z = 2$ [62, 63]. A three-dimensional system $d_{\text{eff}} = 5$, thus, exceeds the critical dimension $d_u > 4$, for which the Ginzburg-Landau theory is valid even close to phase transitions. In consequence, mean-field critical exponents are expected close to so-called spin-density wave quantum critical points. In the vicinity of the critical point quantum fluctuations dominate the finite temperature properties and give rise to a typical fan-shaped critical region, where non-Fermi liquid behavior is expected (see Fig. 2.3b).

As a result of the classical approach, the Landau theory cannot describe phase transitions that arise from inherent quantum effects. Such transitions are observed, for instance, in quantum magnets and some HFs [12, 36], where quantum fluctuations can destroy the Kondo lattice. In consequence, a quantum critical Kondo breakdown involves a major reconstruction of the Fermi surface from a large to a small extent. The origin of the attributed quantum fluctuations is currently an open question. Popular theories include fluctuations of localized moments [57, 58], spin-charge separation [64] or the formation of a spin liquid among the localized mo-

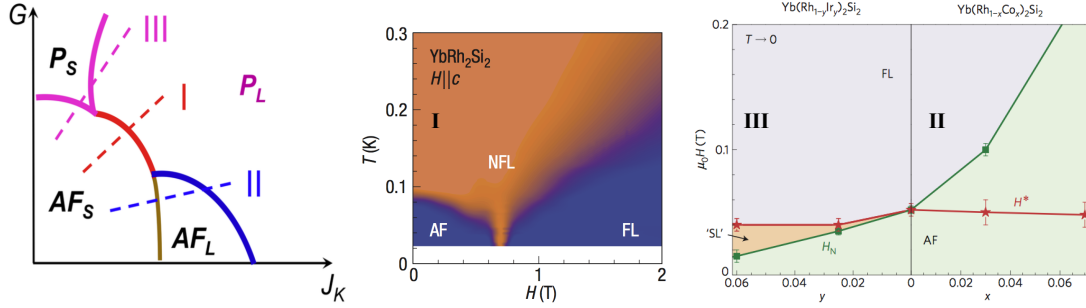


FIGURE 2.4: Global Phase Diagram of Heavy-Fermion Metals. Schematic illustration of the possible magnetic ground states in HF metals as a function of the localized-moment fluctuations, G , and the relevant Kondo scale J_K . P_L denotes a paramagnetic phase with a large Fermi surface, P_S a paramagnetic phase with a small Fermi surface, AF_L antiferromagnetic order with a large Fermi surface and AF_S antiferromagnetic order with a small Fermi surface. Experimental realizations for three possible trajectories are shown in I, II and II. Modified from [12, 13, 67].

ments [65, 66].

2.2.3 The Global Phase Diagram of Heavy-Fermion Metals.

The interplay between magnetic and Kondo fluctuations is captured in the global phase diagram that is depicted in Fig. 2.4. It is parameterized by the two relevant exchange parameters J_K and G , where the latter is a measure of the fluctuations assigned to localized-moment magnetism [13]. It may represent the degree of frustration, the nearest-neighbor interaction, the effective dimensionality or the spatial anisotropy. The probability that the system develops magnetic order decreases for an increasing G . The Kondo coupling strength, $J_K = |J|/W$, is directly correlated to the degree of hybridization between the f -electrons and the conduction band and is divided by the conduction bandwidth W . The phase diagram depicts four distinct regions AF_S , AF_L , P_S and P_L . AF_S denotes the antiferromagnetic phase within the small Fermi surface, where magnetic order is mediated via the RKKY interaction. P_L is the heavy-fermion paramagnetic large Fermi surface, where a fully developed Kondo lattice is established. AF_L represents the antiferromagnetically ordered ground state with a large Fermi surface. Here, magnetism emerges either from unscreened localized moments attributed to AF_S or from P_L via a SDW instability triggered by nested Fermi surface regions. P_S is the paramagnetic metallic state within a small Fermi surface, where the broken rotational symmetry of AF_S is recovered.

The QPTs between P_L and AF_L as well as P_S and AF_S can be modeled within Landau's theory of spin-density wave quantum critical points [62, 63]. The transition between P_L and AF_S , however, represents a quantum critical Kondo breakdown that is referred either to localized moment fluctuations or to spin-charge separation [57, 58, 64]. The transition across P_L and P_S is believed to originate either from the formation of a spin liquid among the localized moments

or via a transition from a spin Peilers state to a HF-liquid [65, 66].

The low energy scales of these ground states allow to effectively tune G and J via external tuning parameters [2, 10, 12, 13]. The ground state of YbRh_2Si_2 , for instance, is tuned over a quantum critical Kondo breakdown by means of a magnetic field (see trajectory I in Fig. 2.4) [68]. A similar QPT is achieved in $\text{CeCu}_{6-x}\text{Au}_x$ by chemical substitution [69], or in CeRhIn_5 via pressure [70]. However, more complex trajectories across the global phase diagram are found in nature (see trajectories II and III in Fig. 2.4). The field dependence of $\text{Yb}(\text{Rh}_{1-x}\text{Co}_x)_2\text{Si}_2$, for instance, reveals a case where AF_S is modified to P_L upon crossing AF_L for increasing magnetic fields [67]. In contrast, the field dependence of $\text{Yb}(\text{Rh}_{1-y}\text{Ir}_y)_2\text{Si}_2$ shows first a magnetic QPT from AF_S to P_S and a subsequent Kondo breakdown towards P_L for sequential field increments [67]. One challenge of the current research in the field is the assignment of the observed phase transitions to the different sections in the global phase diagram. This may allow to disentangle the interactions among the various degrees of freedom in HF systems.

Hitherto, there exists no unified theory that can predict all aspects of the global phase diagram. A widespread approach to interpret the observed experimental data is provided by the phenomenological two-fluid model, which deals with a two-component system of coexisting fluids [71–74]. One fluid represents the large Fermi surface of itinerant conduction electrons that hybridize with f -electrons below the Kondo coherence temperature. The other fluid considers the residual unscreened local moments of the small Fermi surface that works antithetically to the first fluid. The key idea of this approach is evidenced by the hybridization order parameter, $f(T)$, that defines the relative fraction of the two fluids. This temperature dependent variable is tunable via external parameters. The fluid of the large Fermi surface is dominating for $f(0) > 1$, where the system features a HF liquid ground state. In contrast, the overall Fermi surface remains small if $f(0)$ is smaller than unity and $f(0) = 1$ characterizes the critical value, where a quantum critical Kondo breakdown occurs. Both liquids can stabilize an antiferromagnetic ground state that can be modeled within Landau’s theory using a magnetic order parameter.

Within this framework it is straightforward to reproduce the global phase diagram of Fig. 2.4. AF_S and P_S define cases with $f(0) < 1$ and where antiferromagnetic order originates from the predominant small Fermi surface of unscreened localized moments [74]. P_L and AF_L depict the scenario in which $f(0) > 1$ and where a major fraction of the f -bands are hybridized with the conduction electrons. Here, magnetic order can arise either from a SDW instability of the fluid representing the large Fermi surface or via the RKKY interaction of the uncompensated local moments in the fluid describing the small Fermi surface.

The multitude of possible QPTs in the global phase diagram of HF metals provide an environment with strong electronic fluctuations. They can stabilize strongly correlated ground states that interact with the HF ground state, and in which the contributing electronic degrees of freedom are further intertwined. The most prominent one is superconductivity that was found in this class of materials in 1979 [75].

2.3 SUPERCONDUCTIVITY

Superconductivity characterizes a ground state, in which electrons near the Fermi surface condense into a macroscopically coherent bosonic ground state [84, 85]. The superconducting

phase transition breaks the global Gauge symmetry and is accompanied by a gap opening, $\Delta(\mathbf{k})$, at the Fermi surface that is usually of the order of a few meV. Below the critical temperature, T_c , the bosonic state is established by electron pairs, coupled via an attractive exchange interaction that overcomes the screened Coulomb repulsion. The macroscopic properties that emerge from the quantum liquid feature zero resistance and perfect diamagnetism.

Superconductivity was discovered in 1911 [8]. In 1950 Fröhlich proposed that the convolution of electronic and lattice degrees of freedom acts as a glue between the paired electrons [76]. The key idea originates from a moving electron that is attracted by the excess of positive charges, arising from ions that are polarized by an other electron. In 1956 Cooper found that the two-electron bound state with minimal energy corresponds to a so-called Cooper pair with vanishing center of motion $(\mathbf{k}, -\mathbf{k})$ [77]. The microscopic mean-field description of the phonon-mediated superconducting ground state was provided in 1957 by Bardeen, Cooper and Schrieffer (BCS) and could account for the emergent macroscopic properties [78]. Starting from the 70's novel types of superconducting materials were found that could not be explained in the scope of the BCS theory [79]. Most referred classes include the HF superconductors [11, 80], the high- T_c cuprates [81], the iron pnictides [82] and several organic materials [83].

2.3.1 The Symmetry of the Superconducting Order Parameter.

The derivation of the superconducting gap using a general attractive interaction potential in reciprocal space (\mathbf{k} and spin dependent) yields four spin dependent components that are given by [84]:

$$\begin{pmatrix} \Delta_{\uparrow\uparrow}(\mathbf{k}) & \Delta_{\uparrow\downarrow}(\mathbf{k}) \\ \Delta_{\downarrow\uparrow}(\mathbf{k}) & \Delta_{\downarrow\downarrow}(\mathbf{k}) \end{pmatrix} = i(\Delta_k I + \mathbf{d}(\mathbf{k})\boldsymbol{\sigma})\sigma_y = \begin{pmatrix} -d_x(\mathbf{k}) + id_y(\mathbf{k}) & \Delta_k + d_z(\mathbf{k}) \\ -\Delta_k + d_z(\mathbf{k}) & d_x(\mathbf{k}) + id_y(\mathbf{k}) \end{pmatrix}. \quad (2.9)$$

Here, $\boldsymbol{\sigma}$ denotes the vector of Pauli matrices and I is the unity matrix. The equation represents a mixture of spin-singlet and spin-triplet pairing that is distinguishable by the parity properties $\Delta_k = \Delta_{-k}$ for singlet and $\mathbf{d}(\mathbf{k}) = -\mathbf{d}(-\mathbf{k})$ for triplet pairing, respectively. In experimental realizations only one parity solution is expected, because a mixture will lead to two different critical temperatures for which a considered pairing mechanism, most probably, favors only one solution. It is possible to expand the respective gap components in spherical harmonics, which results in [84]:

$$\Delta_k = \sum_{l,m} \eta_{lm} Y_{lm}(\theta_k, \phi_k) \quad (2.10a)$$

$$d_v(\mathbf{k}) = \sum_{l,m} \eta_{vlm} Y_{lm}(\theta_k, \phi_k). \quad (2.10b)$$

$v = x, y, z$ accounts for the three vector components of $\mathbf{d}(\mathbf{k})$ and the quantum numbers equal $l = 0, 1, 2, \dots$ and $m = -l, \dots, l$. The parity properties ensure that only even l s contribute to spin-singlet pairing, while odd values are allowed in the spin-triplet case. In principle several angular momenta can contribute to the symmetry of the superconducting gap and this is believed to be the case in UPt₃ [86]. However, usually only the most dominant term is stabilized, because a multitude of l contributions would trigger several critical temperatures within the same compound.

The superconducting order parameter features an isotropic gap for $l = 0$ (see Fig. 2.5a), which stays invariant under all symmetry operations of the respective crystallographic point

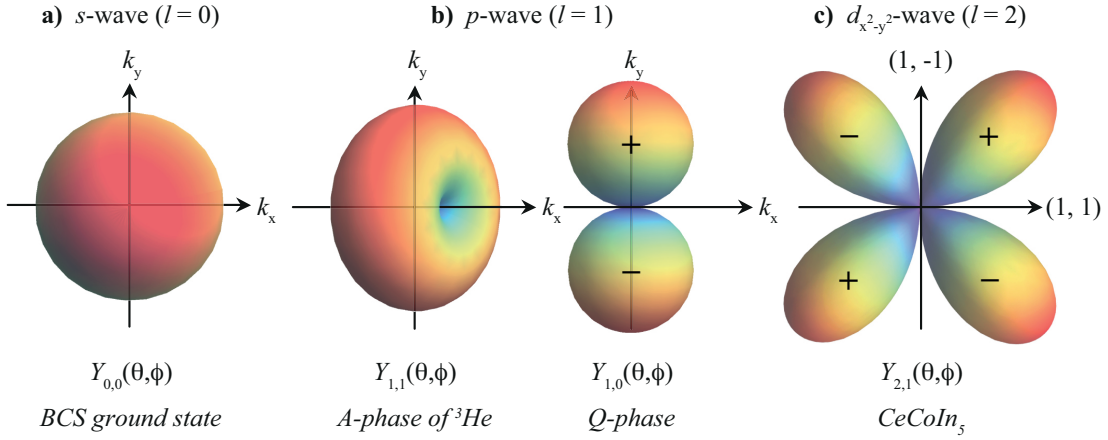


FIGURE 2.5: Possible Gap Symmetries. Illustration of various spherical harmonics assigned to $\Delta(\mathbf{k})$. **a)** BCS ground state with spin-singlet superconductivity and isotropic gap [84, 85]. **b)** Spin-triplet superconductivity as found in superfluid ^3He and in the Q-phase of CeCoIn₅ [79, 88]. **c)** Spin-singlet superconductor with $d_{x^2-y^2}$ symmetry as observed in the main superconducting phase of CeCoIn₅ [18, 19]. Taken from [24].

group [84, 85]. This case is derived by the BCS theory and is defined as conventional superconductivity. Along these lines superconductivity is called unconventional for $l > 0$, which breaks at least one symmetry operation of the crystal point group symmetry. A multitude of unconventional spin-singlet and spin-triplet superconducting order parameters that are observed in nature are shown in Fig. 2.5b-c.

2.3.2 The Superconducting Pairing Interaction.

One of the major questions regarding the superconducting ground state concerns the origin of the attractive pairing interaction between two electrons at \mathbf{k} and \mathbf{k}' . In general, free electrons reveal a repelling Coulomb interaction of the form $U(\mathbf{q}) = 4\pi e^2/|\mathbf{q}|^2$ with $\mathbf{q} = \mathbf{k} - \mathbf{k}'$ [85]. Electrons in a metal are, however, described by quasiparticles that possess a reduced repulsion, as they move in a dielectric medium. The effective Coulomb force is screened over the Thomas Fermi length $1/k_s \approx 1 \text{ \AA}$, which substitutes $|\mathbf{q}|^2$ with $|\mathbf{q}|^2 + |\mathbf{k}_s|^2$ in $U(\mathbf{q})$.

An attractive interaction may arise via a virtual phonon with momentum $\hbar\mathbf{q}$ that is created by one electron and absorbed from the other one (see Fig. 2.6a). This yields a final electron-electron interaction of the form [84, 85]:

$$U(\mathbf{q}, \omega) = \frac{4\pi e^2}{|\mathbf{q}|^2 + |\mathbf{k}_s|^2} + \frac{4\pi e^2}{|\mathbf{q}|^2 + |\mathbf{k}_s|^2} \frac{\omega_q^2}{\omega^2 - \omega_q^2}, \quad (2.11)$$

where $\hbar\omega_q$ is the energy of the virtual phonon. Although the model is oversimplified[¶], it

[¶]The model does not include the band structure of the material and the interaction is suppressed for $\omega = 0$.

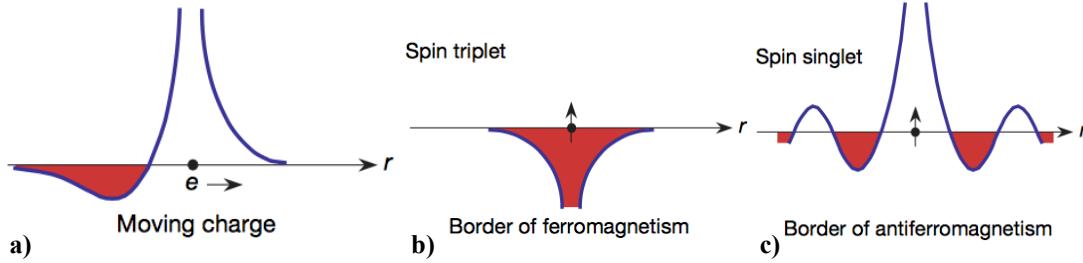


FIGURE 2.6: Possible Superconducting Pairing Interactions. Illustration of attractive interaction potentials among electrons as a function of distance r . **a)** denotes the case of phonon mediated superconductivity as proposed by Fröhlich [76]. **b)** and **c)** show scenarios of attractive spin-spin interaction potentials on the border of ferromagnetism and antiferromagnetism. Taken from [6].

shows that the phonon-mediated interaction is of the same order as the Coulomb repulsion and attractive for $\omega < \omega_q$.

The original BCS model is derived from a \mathbf{q} -independent effective interaction potential $-U$, where the phonon frequency, ω_{eff} , is of the order of the Debye frequency [78, 85]. The superconducting ground state features a spin-singlet order parameter with isotropic s -wave symmetry (see Fig. 2.5a). In the weak-coupling limit $N(\epsilon_F)U \ll 1$, where $N(\epsilon_F)$ is the density of states at the Fermi level, the superconducting order parameter equals $\Delta_{BCS} = 2\hbar\omega_{eff}\exp(-2/(N(\epsilon_F)U))$.

Most of the superconducting materials that are found in nature can be described by the BCS theory of conventional superconductors. In contrast, this points towards the open question of the attractive pairing interaction in unconventional superconductors. Historically this question was addressed first in ^3He , which becomes superfluid below 2-3 mK [79]. Since the phase is characterized by a fluid, there exist no phonons that can generate an attractive interaction among the fermions. However, ^3He may be located close to ferromagnetic order and features strong van der Waals forces [10]. Ferromagnetic fluctuations would trigger an attractive interaction for spin-triplet superconductivity (see Fig. 2.6b) and experimental evidence for a $l = 1$ p -wave gap has been found (see Fig. 2.5b) [79].

In crystalline solids unconventional superconductivity has been observed in HF materials [11, 80], the high- T_c cuprates [81], the iron pnictides [82], several organic materials [83] and conceivably in other material classes [87]. Similarly to ^3He , it is possible to tune most unconventional superconductors over QPTs into other correlated ground states (c.f. Fig. 2.4 for HF materials). Several superconducting phases feature maximal critical temperatures at specific points in phase space, where electronic fluctuations are strongest [6, 10, 11, 25]. Therefore, ferromagnetic, antiferromagnetic or other electronic fluctuations, such as of Kondo-type, are proposed as attractive pairing interactions for unconventional superconductivity [6, 10, 11, 25, 80, 89].

2.3.3 The Superconducting Spin Resonance.

Several cuprates, HFs and pnictides feature a characteristic spin-1 excitation that occurs below the critical temperature [91, 92, 104]. The energy of this so-called spin resonance scales linearly with the size of the superconducting order parameter and is independent on the material class. This suggests that magnetic excitations play a major role in the formation of these spin-singlet Cooper pairs [93].

A magnetic excitation causes an enhanced dynamic susceptibility, $\chi(\mathbf{q}, \omega)$, that is shown in Eq. 2.5 for an itinerant paramagnet. The emergence of the superconducting gap yields modifications of the Lindhard function, $\chi_0(\mathbf{q}, \omega)$, and the quasiparticle interaction $U(\mathbf{q}, \omega)$ [94, 95].

A widespread interpretation of the superconducting resonance is the spin exciton that originates from a feedback effect of the superconducting ground state on the excitation spectrum [94–96]. Similar to an electron-hole exciton in an insulator, the spin exciton in an unconventional superconductor represents a collective bound state inside the superconducting gap. As a result of the superconducting condensate, the Lindhard function features an auxiliary coherence factor and reads [97]:

$$\chi_0(\mathbf{q}, \omega) = -\frac{g\mu_B^2}{V} \sum_{\mathbf{k}} \underbrace{\left(1 - \frac{\Delta_{\mathbf{k}}\Delta_{\mathbf{k}+\mathbf{q}} + \epsilon_{\mathbf{k}}\epsilon_{\mathbf{k}+\mathbf{q}}}{E_{\mathbf{k}}E_{\mathbf{k}+\mathbf{q}}}\right)}_{\text{Coherence factor}} \frac{n_{\mathbf{k}+\mathbf{q},\uparrow} + n_{\mathbf{k},\downarrow} - 1}{E_{\mathbf{k}+\mathbf{q}} - E_{\mathbf{k}} - \hbar\omega + i\hbar\eta}. \quad (2.12)$$

g , V , $n_{\mathbf{k},s}$ and $\epsilon_{\mathbf{k}}$ are defined as in Eq. 2.6. $E_{\mathbf{k}} = \sqrt{\Delta_{\mathbf{k}}^2 + \epsilon_{\mathbf{k}}^2}$ is the quasiparticle dispersion of the superconducting condensate that acquires a spin-singlet gap $\Delta_{\mathbf{k}}$. The coherence factor triggers a maximal $\chi_0(\mathbf{q}, \omega)$ at the characteristic wave-vector \mathbf{Q} , where the superconducting order parameter satisfies $\Delta_{\mathbf{k}+\mathbf{Q}} = -\Delta_{\mathbf{k}}$. This is in agreement with an enhanced quasiparticle interaction along the node of the superconducting order parameter and results in a peaked $\chi(\mathbf{q}, \omega)$ [94, 95].

It is noted that the resonance has also been described as a magnon-like excitation in HF systems, which is connected to the hybridization between the f - and the conduction band [98–100]. In the normal state this excitation decays rapidly into the conduction electrons as a result of Landau overdamping. The opening of the superconducting gap suppresses the damping term and triggers an enhancement of the excitation. The conclusion for either of the models is complicated, because it is thought that the superconducting ground state is stabilized by the hybridized electrons in HF systems [73].

2.3.4 The Question of a Microscopic Model for Unconventional Superconductivity.

Hitherto, there exists no unified microscopic theory for unconventional superconductivity, which may arise particularly from the high complexity of the correlated many-body problem [10, 87]. The minimal description of the cuprates, for instance, is thought to be reduced to the Hubbard model that is shown in Eq. 2.8. However, already for the potentially insufficient case of a single d -orbital, Quantum Monte Carlo simulations show conflicting results [10]. In contrast, multiband models are unavoidable in most cases including HF materials, pnictides and probably cuprates. Additional complexity arises from the fact that the electron-electron interaction cannot be treated in a perturbative approach. Even the phonon-mediated exchange in the BCS theory is not analytic in the zero interaction limit [85]. In consequence, the potential

is not expandable in a power law, which may be one of the reasons that delayed the development of the theory. Theoretical models for unconventional superconductivity have tried to work around this problem but have revealed only limited success so far [10].

The situation is further complicated because there is no general agreement on the type of fluctuations among the different material classes [87]. While in most HFs, pnictides and organic superconductors the pairing interaction is thought to arise from antiferromagnetic fluctuations [87, 101–106], this is controversial in the cuprates [6, 87, 107, 108]. Based on the large Hubbard repulsion, ferromagnetic fluctuations have been proposed in this class of materials by Phil Anderson [108]. Moreover, several HF materials, such as CeCu_2Si_2 , CeCu_2Ge_2 as well as CeRhIn_5 under pressure and, as it will be discussed in chapter 5.3, $\text{Nd}_{1-x}\text{Ce}_x\text{CoIn}_5$ for $x = 1$ and 0.95 under magnetic field feature superconducting phases that may arise from non-magnetic fluctuations [28, 70, 80, 109, 110].

Further insight in the microscopic nature of unconventional superconductors may be gained from the interaction with magnetic order, which is discussed in the following section for conventional superconductors and HF materials.

2.4 INTERPLAY BETWEEN SUPERCONDUCTIVITY AND MAGNETISM

The interplay between magnetism and superconductivity has been studied initially by Ginzburg in 1956 [111]. He considered the possibility of a ferromagnetic superconductor, concluding that magnetic impurities will suppress the bosonic ground state. Experimental evidence for this prediction was found first in La, where the BCS ground state is destroyed by a 1-2% intercalation of Gd impurities and ferromagnetism emerges for concentrations larger than about 3% [112]. In this case the exchange field between the magnetic impurity moments and the bound spin-singlet states triggers Cooper pair breaking effects.

2.4.1 Conventional Superconductors.

Starting from the early 70's coexistent magnetic order and superconductivity has been observed in the Chevrel phases (RMO_6S_8 and RMO_6Se_8), the rhodium borides (RRh_4B_4) and the borocarbides ($\text{RNi}_2\text{B}_2\text{C}$) [113–119]. R are selected rare-earth elements. The materials feature conventional superconductivity within a small Fermi surface (see Fig. 2.4). Magnetic order among the localized moments is mediated via the indirect RKKY interaction, which strongly reduces the direct exchange with the Cooper pairs [120, 121]. Here, a coexistence between magnetism and superconductivity is established, unless electron pairs are separated by magneto-static or Fermi surface effects.

In this respect, non-destructive ferromagnetic superconductivity is found in cases where the internal field, arising from the localized moments, is smaller than the lower critical field H_{c1} [120, 121]. An exceeding internal field causes orbital supercurrents that break up Cooper pairs, destabilizing the superconducting ground state. At internal fields above the upper critical field,

^{||}One distinguishes between type-I and type-II superconductors. A type-I superconductor shows perfect diamagnetism until the increasing magnetic field strength surpasses the binding energy of the Cooper pairs. In a type-II superconductor magnetic fields can penetrate the superconducting state in quantized flux lines (vortices) above H_{c1} and below the upper critical field H_{c2} . This so-called mixed state reveals non-superconducting vortex cores that are of the order of the Cooper pair coherence length, ξ , and screened by orbital supercurrents [84].

H_{c2} , superconductivity is lost and a reentrant ferromagnetic phase occurs, such as observed in ErRh_4B_4 [122, 123].

In an antiferromagnetic superconductor with an internal field that is fluctuating on a length scale shorter than the coherence length of the Cooper pairs, the suppression of superconductivity does not originate from magneto-static interactions [122, 123]. In these cases the competition originates mainly from conflicting electron states because both the RKKY interaction and superconductivity involve quasiparticles close to the Fermi surface. Conventional superconductivity reveals an isotropic gap that gives rise to exotic phenomena, such as anomalous upper critical fields resulting from pair-breaking effects.

2.4.2 Heavy-Fermion Superconductors.

The superconducting state in HF materials results from a large Fermi surface [11, 74]. Here, the superconducting gap symmetry features points or line nodes, where low-energy quasiparticles can mediate magnetic order without competing directly with the condensate. In addition, these ground states often emerge in an environment with strong electronic fluctuations, where the application of external parameters may trigger phases that display novel physical phenomena [6, 10, 11, 25, 80, 89].

CeCu_2Si_2 is the HF superconductor that has been discovered first and which is located close to a quantum critical point at ambient pressure [75, 124]. Depending on the exact Cu content, experimental realizations show either antiferromagnetic, superconducting or coexistent phases [125]. In the latter case, the ordered states are spatially separated and competitive [125, 126]. This is consistent with a superconducting order parameter that features a gap along the magnetic ordering vector [127–129]. Under pressure the antiferromagnetic order is suppressed and superconductivity emerges in a two dome-shaped structure, such as in isostructural CeCu_2Ge_2 [130]. While the superconducting dome at lower pressure is thought to arise from antiferromagnetic fluctuations, the pairing mechanism of the high-pressure phase is debated [80, 109, 110]. Leading theories argue either in the direction of Kondo fluctuations, as found in pressurized CeRhIn_5 [39, 70, 80], or along the lines of orbital fluctuations [109, 110].

A microscopically coexisting and competing magneto-superconducting state is observed in other HF superconductors. This includes the cases of CePd_2Si_2 , CeIn_3 , UPd_2Al_3 and UNi_2Al_3 [131, 132], for which the generic temperature, T , and tuning parameter, g , phase diagram is depicted in Fig. 2.7a. CePd_2Si_2 and CeIn_3 show antiferromagnetic order at ambient pressure that reveals a linearly decreasing ordering temperature, T_N , as the pressure is increased. Unconventional superconductivity emerges in a dome centered around the critical pressure, p_c , where a spin-density wave quantum critical point is expected [131, 132]. In UPd_2Al_3 and UNi_2Al_3 a superconducting phase emerges within an antiferromagnetic phase. Upon increasing pressure T_c remains constant in UPd_2Al_3 up to $p = 6.5$ GPa and then linearly decreases, whereas superconductivity is rapidly suppressed in UNi_2Al_3 [131, 132].

These materials show only moderately enhanced effective masses at ambient pressure and magnetic order that may be attributed to localized-moment magnetism [131]. This suggests a globally small Fermi surface with partially screened localized moments that can be described within the two-fluid model by a non-vanishing large Fermi surface fluid (see chapter 2.2.3). Thus, the application of pressure in CePd_2Si_2 and CeIn_3 may increase the hybridization, which results in a decreasing small Fermi surface fraction. In consequence, the magnetic moment is reduced until the superconducting state is established. Experimental evidence for a continuous

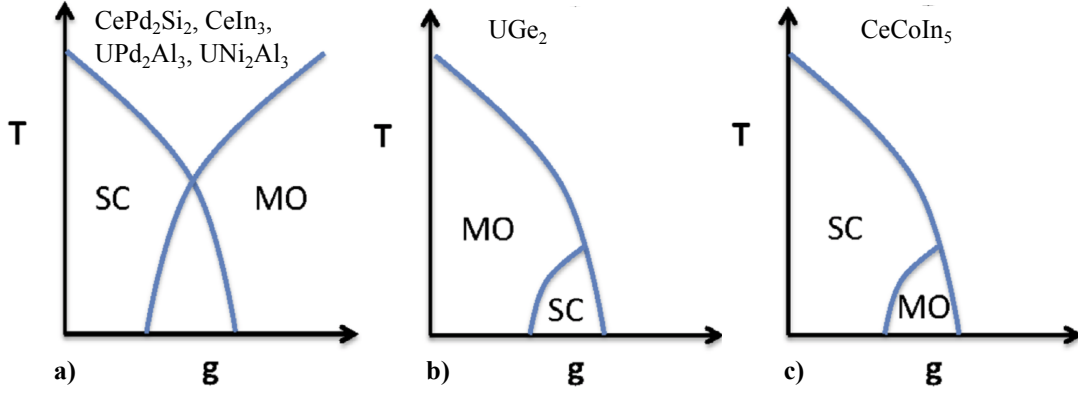


FIGURE 2.7: Interplay between Superconductivity and Magnetism in Heavy-Fermion Systems. Generic temperature, T , and tuning parameter, g , phase diagram of magnetic order (MO) and superconductivity (SC) in HF systems. **a)** Coexisting competition as observed in CePd₂Si₂, CeIn₃, UPd₂Al₃ and UNi₂Al₃. **b)** MO-induced superconductivity that occurs in UGe₂. **c)** SC-induced magnetic order as found in CeCoIn₅. Modified from [25].

Fermi surface reconstruction from a small Fermi surface at low pressure to a large Fermi surface above p_c has been observed in CeIn₃ under field [133]. Similarly, several experimental probes suggest a dual system in UPd₂Al₃, in which one of the three uranium $5f$ -bands is hybridized with the conduction band and the other two remain localized [134].

In contrast to systems where magnetic order and superconductivity compete, there exist cases in which both phenomena are intertwined into a cooperative ground state [25, 131]. In these materials a magnetic phase can stabilize only inside the superconducting phase or, vice versa, a superconducting state is caused by magnetic order. The only known experimental realization where magnetic order induces superconductivity is UGe₂, whose generic phase diagram is shown in Fig. 2.7b [25, 131]. The HF features ferromagnetic order below $T_c = 52$ K at ambient pressure with a reduced magnetic moment that is consistent with itinerant $5f$ -electronic states [135]. Inside the ferromagnetic phase an anomaly of the electrical resistivity at $T_x \approx 25$ K is observed that is accompanied with an increasing ferromagnetic moment [136, 137]. This suggests the existence of two distinct ferromagnetic phases in UGe₂. Under pressure, T_c and T_x monotonically decrease, whereas the ferromagnetic transition becomes first order above $p_x \approx 1.2$ GPa and the phase boundary collapses at $p_c = 1.6$ GPa [138–140]. The lower ferromagnetic phase is expected to vanish at p_x , where the center of a superconducting dome is found. Superconductivity is most probably of spin-triplet p -wave type that enables a coexistence with the ferromagnetic ground state [131, 132]. Intriguingly, the superconducting ground state exists only within the ferromagnetic phase and collapses simultaneously with magnetic order at $p_c = 1.6$ GPa [138–140]. This provides direct evidence for a strongly correlated ground state, in which the presence of magnetic order triggers an unconventional superconducting

phase. Hitherto, the origin of the QPT at p_x is unsolved, but it has been suggested to arise from orbital moment fluctuations [141].

The opposite scenario in which magnetic order is only stabilized within a superconducting phase is observed in CeCoIn₅ (see Fig. 2.7c). The material features unconventional superconductivity with a well-established $d_{x^2-y^2}$ -gap symmetry at zero magnetic field and ambient pressure [17–19]. Antiferromagnetic order emerges in a field-induced quantum phase transition above $\mu_0 H = 9.8$ T and collapses in a first-order transition at the upper critical field together with superconductivity [23, 88, 144–146]. Magnetic order is populated along the d -wave node providing direct evidence for a microscopic coexistence of both phases that arise from a multicomponent ground state [23]. Further information on the properties of CeCoIn₅ is shown in chapter 4.

2.4.3 Theoretical Models of Superconductivity-induced Magnetism.

The microscopic origin of a magnetic phase that is induced by the superconducting condensate has been studied by several theoretical approaches over the last years [147–158]. A multitude of them require Pauli-limited superconducting condensates, in which the bound electron-pairs are separated via field-induced Zeeman splitting**. In HFs the effective masses that contribute to superconductivity substantially increase the critical field, for which orbital supercurrents destroy the Cooper pairs††. In consequence, Pauli paramagnetic pair breaking effects gain in importance in spin-singlet HF superconductors, making CeCoIn₅ a prime candidate to test some of the proposed theories.

A relative direct way to couple antiferromagnetic order and unconventional superconductivity is the condensation of the spin resonance into the ground state of the system [147]. The spin resonance arises from magnetic fluctuations and appears only inside the superconducting state (see chapter 2.3.2). Thus, in a scenario where the gap of the spin resonance is suppressed, static magnetic order is present only inside the superconducting phase and couples directly to it. Theoretically it was shown that a superconducting spin exciton can become soft under magnetic field in a two-dimensional material that features Pauli-limited $d_{x^2-y^2}$ -wave superconductivity [147].

Other models rely on so-called pair-density waves (PDWs) that represent spatially-modulated superconducting order parameters [148–153]. Their existence was predicted first by Fulde, Ferrel, Larkin and Ovchinnikov, who studied the emergence of a PDW in a Pauli-limited s -wave superconductor [148, 149]. Their theory, however, is also relevant for other spin-singlet superconducting gap symmetries, such as d -wave superconductors. A strong magnetic field can cause Zeeman-split, spin-polarized conduction bands. In cases where the orbital limited field is much larger than the Pauli limiting field, the field-induced energy imbalance between spin-up and spin-down conduction electrons results in spin-singlet Cooper pairs for which the center of motion does not longer vanish (see Fig. 2.8a). They feature a net momentum $\mathbf{q} = \mathbf{k}_\uparrow - \mathbf{k}_\downarrow$ that is proportional to the magnetic field strength and SDW order can arise from Andreev bound states in the nodal directions of the superconducting order parameter at low temperatures [155]. A

**The Pauli limiting field of a superconductor is calculated by the size of the superconducting gap, Δ , and the Landé splitting factor, g , by means of $\mu_0 H_{c_2}^P = \Delta/\sqrt{g}$ [143].

††The orbital limiting field is calculated from the critical field at which two vortex cores overlap and is given by $\mu_0 H_{c_2}^{orb} = \Phi_0/2\pi\xi^2 \propto m^{*2}$, where Φ_0 is the magnetic flux quantum, ξ the Cooper pair coherence length and m^* the effective mass [142].

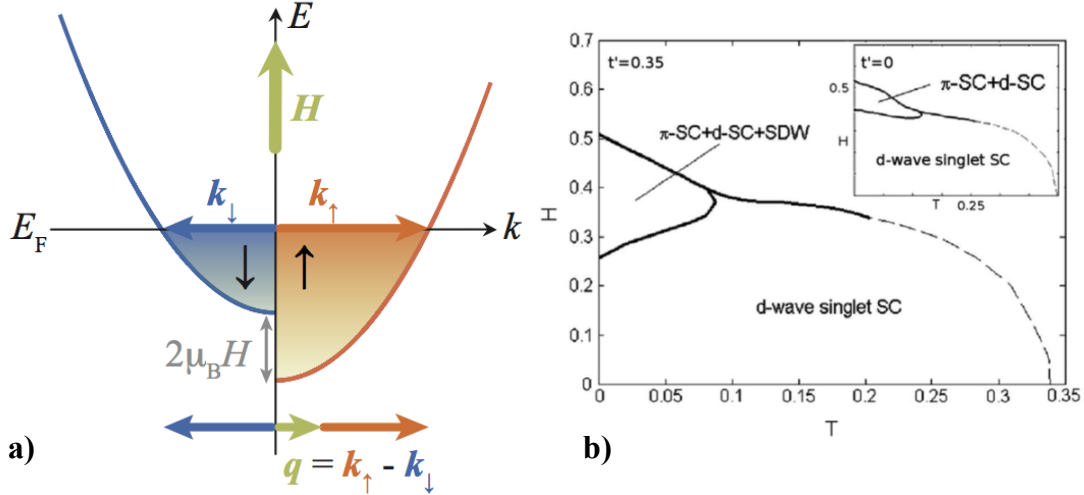


FIGURE 2.8: Spatially-Modulated Superconducting Order Parameter. **a)** Creation of a Cooper pair in a FFLO-phase via Zeeman split, spin polarized electronic bands. **b)** HT -phase diagram of a spin-singlet d -wave superconductor that features an additional superconducting phase, where a SDW is coupled to superconductivity via a spin-triplet PDW. Taken from [24, 153].

spatially-modulated spin-singlet superconducting phase is commonly referred as FFLO-phase and separated from the main superconducting phase ($k_\uparrow = -k_\downarrow$) by either a first or a second order phase transition [154, 155].

In contrast to FFLO-superconductivity, other theoretical models predict PDWs that feature a spin-triplet state [150–153]. The general structure of a superconducting gap that arises from a generic k and spin dependent attractive interaction potential, describes a mixture of spin-singlet and spin-triplet Cooper pairs (see Eq. 2.9). Although in most cases only one parity solution is realized, a simultaneous occurrence of both symmetries is predicted in the case where superconductivity and magnetic order emerge from the same electrons [150]. An admixed spin-singlet spin-triplet superconducting condensate is supported by a study that considers the scenario where the attractive interaction potential is mediated by antiferromagnetic fluctuations in two dimensions [151]. This theory shows that a singlet state is realized at zero magnetic field, but weakened by Pauli paramagnetic effects at high fields where a spin-triplet pairing is favored. The coexistence of both parity solutions is particularly enhanced when Pauli limiting and orbital critical fields are of the same order [152]. In this study it was also found that the mixed ground state breaks spin-rotational symmetry and features spin-triplet Cooper pairs that are oriented perpendicular to the field direction. Later, numerical calculations of a mean-field model Hamiltonian that accounts for a superconducting d -wave, a SDW and a spin-triplet PDW order parameter revealed a phase diagram as shown in Fig. 2.8 [153]. In

addition to d -wave superconductivity, another phase is suggested below the upper critical field that features a SDW induced by a primary spin-triplet PDW order parameter. In contrast, it has also been argued recently that the SDW arising from FFLO-superconductivity can trigger a secondary spin-triplet superconducting order parameter [158].

Chapter 3

Neutron Scattering

Strongly correlated electron systems feature a deep intertwining among various degrees of freedom [32]. The emergent transport properties can be characterized by macroscopic probes, such as electrical resistivity, magnetic susceptibility or heat capacity (see Fig. 2.1). A detailed study of the microscopic interactions on an atomic scale is, however, needed for a fundamental understanding of the underlying physics in these materials. Scattering techniques based on particle beams consisting of photons or neutrons have proven to be particularly potent in the field of condensed matter [7, 23, 36, 37, 39]. X-ray and neutron scattering are two highly complementary techniques, which are often combined to progress in an open scientific question.

Investigations of magnetic interactions at low temperatures (sub-Kelvin) and large magnetic fields are particularly suited for neutron scattering [14–16]. The particle is a charge neutral stable fermion with spin $S = 1/2$ [159]. Since no Coulomb barrier needs to be overcome, the neutron is scattered from the nuclear forces in the bulk of the material [14–16]. Thus, the technique can be used to distinguish isotopes and chemical elements with comparable atomic numbers. The weak interaction with their surrounding has two additional advantages. Firstly, neutrons can easily penetrate sample environments, such as dilution refrigerators, pressure cells or cryogenic magnets that are required for experiments under extreme conditions. Secondly, slow neutrons only weakly perturb the ground state of the system, such that a linear-response theory accurately models the scattering process. Cold and thermal neutrons ($\lambda = 1 - 10 \text{ \AA}$) feature length scales comparable with the interatomic distances in a crystal and energies in the range of their elementary excitations. Therefore, the technique allows to investigate dynamic processes that are related to the ground state properties of the material. Finally, the neutron carries a magnetic moment, which enables a direct study of magnetic order and correlations in experimental realizations [14–16].

3.1 NEUTRON SOURCES

Neutrons that can be used for scientific research are produced either by a nuclear reactor or by a spallation source. While reactor facilities use the spontaneous fission process of ^{235}U , neutrons are generated via proton collision in spallation sources [14]. The results presented in this thesis were mainly carried out at the High Flux Reactor of the Institut Laue-Langevin (ILL), Grenoble France and at the Swiss Spallation Source (SINQ) of the Paul Scherrer Institut, Villigen Switzerland. The research reactor in France delivers a neutron flux of

$I \approx 1.5 \cdot 10^{15}$ neutrons/(cm²s) with a thermal power of $W \approx 58.3$ MW, whereas SINQ is based on a 590 MeV proton cyclotron with accelerator frequency of $\tau = 50.63$ MHz [160, 161]. In the latter case a quasi-continuous proton beam is guided on a neutron target that is made of an array of lead rods enclosed in zircaloy tubes [162].

Irrespective of their production the energy spectrum of the neutrons released from the source is in the range of several MeV [14]. Moderator tanks filled with deuterium or an admixture of heavy and light water are used to shift the initial energy of the neutrons to $E = 0.5 - 5$ or $5 - 100$ meV in a cold or thermal source, respectively. Finally, the neutrons are directed to the instruments using total reflection on supermirrors that are mounted inside lead-shielded neutron guides [163].

3.2 SCATTERING THEORY

Prior to the scattering process with a sample placed on the instrument, neutrons with an identical wave-vector \mathbf{k}_i are obtained from a velocity selector or from a monochromator (see chapter 3.5). The initial energy of the neutron is given by $E_i = \hbar^2/(2m)|\mathbf{k}_i|^2$ and its spin is denoted as s_i . \hbar is the reduced Planck constant and $m = 1.675 \cdot 10^{-27}$ kg represents the neutron mass [15]. The interaction of the neutron with the sample is described by the potential U and yields the state \mathbf{k}_f with E_f and s_f , accordingly.

The partial differential cross section defines the number of neutrons that are scattered into the infinitesimal small solid angle $d\Omega$ with an energy transfer $d\omega$ and is normalized by the incident neutron flux. For a general interaction operator, \hat{U} , it can be calculated using Fermi's golden rule [14–16]:

$$\frac{d^2\sigma}{d\Omega d\omega} = \left(\frac{m}{2\pi\hbar^2}\right)^2 \frac{k_f}{k_i} \sum_{\lambda_f s_f} \sum_{\lambda_i s_i} p_{\lambda_i} p_{s_i} \underbrace{|\langle \lambda_f, \mathbf{k}_f, s_f | \hat{U} | \lambda_i, \mathbf{k}_i, s_i \rangle|^2}_{\text{Matrix element}} \underbrace{\delta(E_{\lambda_i} - E_{\lambda_f} + \hbar\omega)}_{\text{Energy conservation}}, \quad (3.1)$$

where $|\lambda_i\rangle$ and $|\lambda_f\rangle$ denote the quantum states of the sample before and after the scattering process, respectively. E_{λ_i} and E_{λ_f} are the associated energies, p_{λ_i} is the thermal population factor of $|\lambda_i\rangle$ and p_{s_i} the spin polarization probability. The nuclear forces responsible for the scattering process have an interaction radius that is about ten thousand times smaller than the neutron wave-length [15]. Thus, the incident and scattered neutrons can be described as plane waves $|\mathbf{k}_{i,f}\rangle = \exp(i\mathbf{k}_{i,f}\mathbf{r})$.

3.2.1 Nuclear Scattering.

The scattering process between neutrons and atoms that are fixed at discrete positions \mathbf{R}_j is approximated by the Fermi pseudopotential [14–16]:

$$\hat{U}(\mathbf{r}) = \frac{2\pi\hbar^2}{m} \sum_j b_j \delta(\mathbf{r} - \mathbf{R}_j). \quad (3.2)$$

b_j defines the interaction radius of the nuclear forces at position \mathbf{R}_j . Since these radii are much smaller than the neutron wave-length, the scattering takes place at the atomic site and is independent on the modulus of reciprocal space position* ($|\mathbf{Q}|$ -independent). The general

*This is in contrast to an X-ray experiment, where the photons interact with the spatially extended electron cloud [15].

	σ_{coh}	σ_{inc}	σ_{abs}
Nd	7.43	9.2	50.5
Ce	2.94	0.001	0.63
Co	0.779	4.8	37.18
In	2.08	0.54	193.8

TABLE 3.1: Coherent, Incoherent and Absorption Cross Sections of Nd, Ce, Co and In. Cross sections of the chemical elements that are relevant for this thesis. The values are given in barns, 1 barn = 10^{-28} m² [164].

nuclear cross section is derived by substituting \hat{U} into Eq. 3.1 and reads [14–16]:

$$\frac{d^2\sigma}{d\Omega d\omega} = \frac{1}{2\pi\hbar} \frac{k_f}{k_i} \sum_{j,j'} b_j b_{j'} \int_{-\infty}^{\infty} \underbrace{\langle e^{-i\mathbf{Q}\mathbf{R}_{j'}(0)} e^{i\mathbf{Q}\mathbf{R}_j(t)} \rangle}_{\langle \hat{A} \rangle = \sum_{\lambda} p_{\lambda} \langle \lambda | \hat{A} | \lambda \rangle} e^{-i\omega t} dt, \quad (3.3)$$

where $\mathbf{Q} = \mathbf{k}_f - \mathbf{k}_i$.

A system consisting of one single chemical element is described by the nuclear scattering lengths, b_j , at \mathbf{R}_j that depend on the considered isotope and its nuclear spin quantum state. Since there is no correlation between the scattering length of atom j and j' , we derive the averaged values $\langle b_j b_{j'} \rangle = \langle b \rangle^2$ ($i \neq j$) and $\langle b_j b_j \rangle = \langle b^2 \rangle$. The resulting differential cross section decomposes in a pair-correlated (coherent) and self-correlated (incoherent) part [14–16]:

$$\begin{aligned} \left(\frac{d^2\sigma}{d\Omega d\omega} \right)_{coh}^{el} &= N \frac{k_f}{k_i} \frac{\sigma_{coh}}{4\pi} S_{coh}(\mathbf{Q}, \omega) \\ \left(\frac{d^2\sigma}{d\Omega d\omega} \right)_{inc}^{el} &= N \frac{k_f}{k_i} \frac{\sigma_{inc}}{4\pi} S_{inc}(\mathbf{Q}, \omega), \end{aligned} \quad (3.4)$$

where N is the total number of nuclei in the sample. The coherent cross section, $\sigma_{coh} = 4\pi \langle b \rangle^2$, represents the squared weighted average of the different scattering lengths. The incoherent cross section, $\sigma_{inc} = 4\pi(\langle b \rangle^2 - \langle b^2 \rangle)$, defines the statistical variation of σ_{coh} . The element specific coherent and incoherent cross sections are tabulated and the ones relevant for this thesis are shown in Tab. 3.1 [164]. $S_{coh}(\mathbf{Q}, \omega)$ and $S_{inc}(\mathbf{Q}, \omega)$ are the respective dynamical structure factors [14–16]:

$$\begin{aligned} S_{coh}(\mathbf{Q}, \omega) &= \frac{1}{2\pi\hbar N} \sum_{i \neq j} \int_{-\infty}^{\infty} \langle e^{-i\mathbf{Q}\cdot\mathbf{R}_j(0)} e^{i\mathbf{Q}\cdot\mathbf{R}_i(t)} \rangle e^{-i\omega t} dt \\ S_{inc}(\mathbf{Q}, \omega) &= \frac{1}{2\pi\hbar N} \sum_i \int_{-\infty}^{\infty} \langle e^{-i\mathbf{Q}\cdot\mathbf{R}_i(0)} e^{i\mathbf{Q}\cdot\mathbf{R}_i(t)} \rangle e^{-i\omega t} dt. \end{aligned} \quad (3.5)$$

The coherent dynamical structure factor, $S_{coh}(\mathbf{Q}, \omega)$, is the Fourier transformation of the space-time dependent pair correlation function, which is the most general description of static and dynamic processes in condensed matter on an atomic scale [14]. The incoherent dynamical structure factor, $S_{inc}(\mathbf{Q}, \omega)$, represents the self-correlation of one particle at different times.

The elastic differential cross section is obtained from the static part of Eq. 3.4. The time average yields [15]:

$$\begin{aligned} \left(\frac{d\sigma}{d\Omega}\right)_{\text{coh}}^{\text{el}} &= \frac{\sigma_{\text{coh}}}{4\pi} \sum_{i \neq j} e^{-i\mathbf{Q} \cdot (\mathbf{R}_j - \mathbf{R}_i)} \\ \left(\frac{d\sigma}{d\Omega}\right)_{\text{inc}}^{\text{el}} &= \frac{\sigma_{\text{inc}}}{4\pi} \sum_{i=j} e^{-i\mathbf{Q} \cdot (\mathbf{R}_j - \mathbf{R}_i)} = N \frac{\sigma_{\text{inc}}}{4\pi}. \end{aligned} \quad (3.6)$$

The incoherent elastic cross section leads to an isotropic background in neutron diffraction experiments, whereas the coherent elastic cross section provides information about the atomic arrangement in the sample.

So far, we limited ourself to a Bravais lattice that consists of one rigid chemical element. In contrast, a single crystal can feature different atoms per unit cell that reveal a thermally-induced displacement around their equilibrium position. If N_0 is the number of crystallographic unit cells in the sample and each cell consists of a volume V_0 , the coherent elastic cross section is generalized to [16]:

$$\left(\frac{d\sigma}{d\Omega}\right)_{\text{coh}}^{\text{el}} = N_0 \frac{(2\pi)^3}{V_0} \sum_{\mathbf{G}} |F_N(\mathbf{G})|^2 \delta(\mathbf{Q} - \mathbf{G}). \quad (3.7)$$

The delta function corresponds to Bragg's law and \mathbf{G} are the reciprocal lattice wave-vectors determined from the crystal lattice. $F_N(\mathbf{G})$ denotes the nuclear structure factor that depends on the atoms in the unit cell at positions \mathbf{d}_j , their coherent scattering length $\langle b_j \rangle$, and their mean-square displacement encoded in the Debye-Waller factor $\exp(-W_j)$ [16]:

$$F_N(\mathbf{G}) = \sum_j \langle b_j \rangle e^{i\mathbf{G} \cdot \mathbf{d}_j} e^{-W_j}. \quad (3.8)$$

Neutron diffraction, thus, allows to determine the nuclear structure and space group symmetry of a novel material and can refine the actual concentration of different chemical elements in substituted samples (see chapter 5.1). The technique is complementary to X-ray diffraction, where the scattering amplitude scales with the atomic number Z^\dagger .

3.2.2 Magnetic Scattering.

The neutron is a spin $S = 1/2$ fermion with a magnetic dipole moment that equals $\mu = -\gamma\mu_N\sigma$ [14–16]. $\gamma = 1.913$ is the gyromagnetic ratio, $\mu_N = 5.05078 \cdot 10^{-27}$ J/T denotes the nuclear magneton and σ represents the vector of Pauli matrices. The dipole moment of the neutron interacts with an electron via its magnetic field that arises from its spin and momentum (see chapter 2.1). The general interaction potential, U , at the position \mathbf{r} is given by [14]:

$$U(\mathbf{r}) = -\gamma\mu_N\sigma \left[\underbrace{\nabla \wedge \left(\frac{g\mu_B \mathbf{S} \wedge \mathbf{r}}{r^3} \right)}_{\text{spin part}} + \underbrace{\frac{e}{c} \frac{\mathbf{v}_e \wedge \mathbf{r}}{r^3}}_{\text{orbital part}} \right]. \quad (3.9)$$

[†]As a result X-rays are less sensitive to light elements and show little contrast among atoms with similar Z . A huge advantage of X-ray scattering is, however, the large photon flux with high coherence that is provided by 3rd generation synchrotrons.

The spin of the electron is denoted as S , g is the Landé splitting factor, v_e is the electron velocity, μ_B substitutes the Bohr magneton, $e = 1.602177 \cdot 10^{-19}$ C represents the elementary charge and $c = 299792458$ m/s is the speed of light. If we consider an experimental setup for unpolarized neutrons and a sample that consists of magnetic ions at positions \mathbf{r}_j with spin amplitude S_j arising from localized electrons ($v_e = 0$), Eq. 3.1 is expressed as [15]:

$$\frac{d^2\sigma}{d\Omega d\omega} = \left(\frac{\gamma r_0}{2}\right)^2 \frac{k_f}{k_i} \sum_{j,j'} e^{i\mathbf{Q} \cdot (\mathbf{r}_j - \mathbf{r}_{j'})} g_j g_{j'} f_j(\mathbf{Q}) f_{j'}^*(\mathbf{Q}) e^{-W_j} e^{-W_{j'}} |\mathbf{S}_{\perp,j,j'}|^2. \quad (3.10)$$

Here, r_0 is the classical electron radius, $\exp(-W_j)$ the Debeye-Waller factor of the magnetic ion j at \mathbf{r}_j and g_j its Landé splitting factor. The magnetic form factor, $f_j(\mathbf{Q})$, is the Fourier transformation of the unpaired spin density of atom j and features a spacial extension in real space. Thus, in contrast to the nuclear cross section, the magnetic form factor reveals a $|\mathbf{Q}|$ -dependence and decreases with increasing modulus. The magnetic interaction vector, $\langle \hat{\mathbf{S}}_{\perp,j} \rangle$, between the neutron and the magnetic ion at \mathbf{r}_j reads [16]:

$$\langle \hat{\mathbf{S}}_{\perp,j} \rangle = \frac{\mathbf{Q} \times \langle \hat{\mathbf{S}}_j \rangle \times \mathbf{Q}}{|\mathbf{Q}|^2} = \langle \hat{\mathbf{S}}_j \rangle - \frac{\mathbf{Q}(\mathbf{Q} \langle \hat{\mathbf{S}}_j \rangle)}{|\mathbf{Q}|^2} \quad (3.11)$$

and shows that only the spin component perpendicular to the scattering vector \mathbf{Q} is probed in a neutron experiment. The squared modulus of the magnetic interaction vector can be written in terms of the specific magnetic scattering function, $S_{j,j'}^{\alpha\beta}(\mathbf{Q}, \omega)$, representing the Fourier transformation of the time dependent magnetic correlation function between the moment j and j' . Using the cartesian coordinates $\alpha, \beta = x, y, z$ we find [14–16]:

$$|\mathbf{S}_{\perp,j,j'}|^2 = \sum_{\alpha,\beta} \left(\delta_{\alpha,\beta} - \frac{Q_\alpha Q_\beta}{|\mathbf{Q}|^2} \right) S_{j,j'}^{\alpha\beta}(\mathbf{Q}, \omega) \quad (3.12)$$

with

$$S_{j,j'}^{\alpha\beta}(\mathbf{Q}, \omega) = \frac{1}{2\pi\hbar} \int_{-\infty}^{\infty} \langle \hat{S}_j^\alpha(0) \hat{S}_{j'}^\beta(t) \rangle e^{-i\omega t} dt. \quad (3.13)$$

We note that the derivation of the neutron scattering process is more involved when the orbital angular momentum of the magnetic ions is not suppressed [14–16]. In this case the differential cross section is a combination of spin and orbital moments and can reveal an anisotropy in the magnetic form factor as well as a modified Landé splitting factor. The magnetic scattering function, $S^{\alpha\beta}(\mathbf{Q}, \omega) = \sum_{j,j'} S_{j,j'}^{\alpha\beta}(\mathbf{Q}, \omega) \exp[i\mathbf{Q} \cdot (\mathbf{r}_j - \mathbf{r}_{j'})]$, is related to the generalized magnetic susceptibility tensor, $\chi^{\alpha\beta}(\mathbf{Q}, \omega)$, via the fluctuation dissipation theorem [14–16]:

$$S^{\alpha\beta}(\mathbf{Q}, \omega) = \frac{N\hbar}{\pi} \left(1 - e^{-\frac{\hbar\omega}{k_B T}} \right)^{-1} \text{Im}[\chi^{\alpha\beta}(\mathbf{Q}, \omega)], \quad (3.14)$$

where N is the total number of magnetic ions. The real part of the magnetic susceptibility tensor is obtained via the Kramers-Kronig relation [16, 97]. Neutron scattering is, thus, a microscopic probe that allows to measure $\chi^{\alpha\beta}(\mathbf{Q}, \omega)$ in an energy and wave-vector resolved manner. This is in contrast to macroscopic magnetization measurements that probe the \mathbf{Q} -integrated susceptibility tensor.

3.3 MAGNETIC STRUCTURE DETERMINATION

Long-range static ($\hbar\omega = 0$) magnetic order in a crystal yields a magnetic structure with a unit cell volume, V_M , that may extend over several chemical cells. The derivation of the differential cross section is similar to the one of nuclear coherent elastic scattering (see Eq. 3.7) and reads [16]:

$$\left(\frac{d\sigma}{d\Omega}\right)_{\text{coh}}^{\text{el}} = N_M \left(\frac{\gamma r_0}{2}\right)^2 \frac{(2\pi)^3}{V_M} \sum_{\mathbf{G}_M} |F_M(\mathbf{G}_M)|^2 \delta(\mathbf{Q} - \mathbf{G}_M). \quad (3.15)$$

N_M refers to the number of magnetic unit cells and the delta function corresponds to Bragg's law at the reciprocal lattice positions \mathbf{G}_M . The magnetic structure factor, $F_M(\mathbf{G}_M)$, encodes the information on the magnetic structure and is given by:

$$F_M(\mathbf{G}_M) = \sum_j f_j(\mathbf{G}_M) e^{-W_j} g_j \langle \hat{\mathbf{S}}_{\perp,j} \rangle e^{i\mathbf{G}_M \mathbf{d}_j}, \quad (3.16)$$

where the sum runs over the magnetic atoms within the unit cell and may involve different chemical elements that can order independently. This happens, for instance, in TbMnO_3 , where the Mn^{3+} moments order below $T_{N_1} = 42$ K and the Tb^{3+} moments below $T_{N_1} = 8$ K [165]. Using the principle of superposition we can concentrate on magnetic order of one independent spin species only.

3.3.1 Magnetic Moment and Wave-Vector.

Static order reduces the crystalline space group symmetry, G_0 , that is compatible with the elements $g = \{h|\tau\}$, where h represents a rotation and τ a translation [166]. Magnetic Bragg peaks appear at reciprocal lattice positions \mathbf{G}_M that are related to the crystal structure (with lattice vectors \mathbf{G}) via the set of magnetic wave-vectors $\{\mathbf{k}\} = \min[\mathbf{G}_M - \mathbf{G}]$. It can be reduced to elements that do not transform into each other under h , *i.e.*, $\mathbf{k} \neq h\mathbf{k}$. The resulting minimal set of distinct wave-vectors is called star and each element represents one arm of it [166]. The doubling of the tetragonal $P4/mmm$ structure along the crystalline a and c -axis, for instance, reveals the star $\{\mathbf{k}\} = \{\mathbf{k}_1, \mathbf{k}_2\}$ with the two arms $\mathbf{k}_1 = (1/2, 0, 1/2)$ and $\mathbf{k}_2 = (0, 1/2, 1/2)$ (see chapter 5.2.2). The subgroup of G_0 that leaves an arm invariant is named little group and is essential for the magnetic structure determination.

The majority of experimental realizations that feature several distinct wave-vectors, consist of different domains that are represented by a single propagation vector (multi-domain structure) [166]. If higher-order exchange interactions, such as of quadropolar type or crystal electric-field effects have to be considered, the magnetic order may be realized by a multi- \mathbf{k} structure consisting of several arms in a single domain. Experimentally, both scenarios lead to identical diffraction patterns and it is only possible to distinguish them by the application of an external constraint. An external tuning parameter breaks the crystal symmetry on a macroscopic scale and can induce a change in the magnetic domain population (see chapter 5.4.1).

If we define the magnetic moment distribution of the atom j at \mathbf{r}_j as $\mu_j(\mathbf{r}_j) = \sum_{\{\mathbf{k}\}} g_j^{\mathbf{k}} \langle \hat{\mathbf{S}}_{\perp,j}^{\mathbf{k}} \rangle e^{i\mathbf{k}\mathbf{r}_j} = \sum_{\{\mathbf{k}\}} \mu_j^{\mathbf{k}} e^{i\mathbf{k}\mathbf{r}_j}$ [166], we can rewrite Eq. 3.15 as sum over the crystalline lattice, \mathbf{G} , with transformed magnetic structure factor:

$$F_M(\mathbf{G}) = \sum_j f_j(\mathbf{G} + \mathbf{k}) e^{-W_j} \mu_j(\mathbf{d}_j) e^{i\mathbf{G}\mathbf{d}_j}. \quad (3.17)$$

μ_j^k is the magnetic moment vector of atom j and arm k , which is forced to be real by the sum with its complex conjugate. This is necessary for incommensurate structures where $k \neq -k$.

3.3.2 Representational Analysis.

The little group, G_k , consists of all symmetry elements, $g = \{h|\tau\}$, that leave the magnetic wave-vector, k , invariant. Thus, also the magnetic structure needs to be compatible with these elements, where g acts on the positions of the magnetic atoms and on the axial magnetic moment vector [166]. The symmetry operations of G_k permutes the magnetic ion positions, which is described by the representation[‡] Γ_p [§]. The associated character, $\chi_p(g)$, equals the number of magnetic ion positions that remain unchanged under the symmetry operation g . In cases where several magnetic sites in the unit cell exist, each magnetic orbit requires an independent treatment [166]. Here, different scenarios can occur. An identical moment orientation of all sites is expected when the inter-site coupling is dominant. In contrast, distinct structures may arise for strong intra-site exchange interactions.

The transformation of the magnetic moment vector by a symmetry element $g = \{h|\tau\}$ with rotation h yields the axial character [166]:

$$\chi_A(g) = \text{Tr}[\Gamma(h)] \det|\Gamma(h)|. \quad (3.18)$$

The general magnetic representation Γ_M^k is the direct product of the permutation and axial vector representation, $\Gamma_p\Gamma_A$, and leads to the character table $\chi_M^k = \chi_p\chi_A$.

Based on Landau's theory of second-order phase transitions it is advantageous to diagonalize Γ_M^k into orthogonal, irreducible representations $\Gamma_M^k = \sum_{\nu} a_{\nu}^k \Gamma_{\nu}^k$. The theory states that the symmetry-breaking fluctuations govern the symmetry of a single Γ_{ν}^k [166]. The irreducible representations of G_0 with a magnetic wave-vector k are tabulated and reveal the character table χ_{ν}^k [168]. This allows to decompose Γ_M^k into the irreducible representations Γ_{ν}^k with prefactors [166]:

$$a_{\nu}^k = \frac{1}{n(g)} \sum_{g \in G_k} \chi_{\nu}^k(g) [\chi_M^k(g)]^*. \quad (3.19)$$

$n(g)$ is the number of symmetry operations in the little group G_k and the sum runs over the individual elements.

The magnetic moment can be written as $\mu_j^k = \sum_{\nu} C_{\nu}^k \mathbf{S}_{\nu}^k$, where \mathbf{S}_{ν}^k are the basis vectors of the irreducible representations Γ_{ν}^k that are calculated via the projection formula[¶] [166]:

$$P_{\nu}(\mathbf{S}) = \sum_{g \in G_k} [\chi_{\nu}^k(g)]^* g(\mathbf{S}). \quad (3.20)$$

C_{ν}^k is the representation specific amplitude of the magnetic moment that is expected to be nonzero for one ν only, according to Landau's theory. In this thesis, the representational analysis was performed with the program Basireps of the FullProf suite [169].

[‡]A representation denotes the set of matrices that describe the general transformations of a group [167].

[§]If $g(\mathbf{r}_j) = h\mathbf{r}_j + \tau$ is outside the first Brillouin zone, a phase factor $\theta = -2\pi k[g(\mathbf{r}_j) - \mathbf{r}_j]$ is added.

[¶] $\mathbf{S} = (S_x, S_y, S_z)$ is a general axial vector.

3.4 ABSORPTION AND EXTINCTION

Atoms in a crystalline structure experience an unequal neutron intensity, because the beam is attenuated as the particles penetrate the material [14]. This arises from two effects, which refer to absorption and extinction that is related to the diffraction process.

A monochromatic beam guided on a single crystal that is oriented in Bragg condition gradually decreases in intensity as neutrons diffract on successive lattice planes [14]. Extinction is mainly relevant for ultra clean single crystals and negligible for polycrystalline samples. Here, the random distribution of crystallites suppress the probability of consecutive Bragg planes in the same orientation. Most single crystals feature imperfections, such as defects and dislocations that lead to a crystalline mosaicity for which primary extinction is small.

The incident neutron intensity is also reduced when the neutrons are absorbed by the nuclei in the material [14]. The absorption cross section is element specific and shown in Tab. 3.1 for Nd, Ce, Co and In [164]. The reduction of the initial neutron intensity, I_0 , arising from coherent^{||} and incoherent scattering as well as from absorption is described by the linear attenuation factor μ . It yields a reduced transmitted intensity, I_d , when the neutrons travel through a crystal of thickness d [14]:

$$I_d = I_0 e^{-\mu d}. \quad (3.21)$$

Both attenuation effects have to be included in the data analysis of the recorded neutron patterns. While extinction effects are dominating for single crystal diffraction on small samples ($V \approx 1 \text{ mm}^3$), absorption effects may be dominant for certain chemical compositions [14].

This thesis focuses on the microscopic properties of the series $\text{Nd}_{1-x}\text{Ce}_x\text{CoIn}_5$. The material consists mainly of indium (5:7 parts), which reveals a large absorption cross section (see Tab. 3.1). Moreover, the chemical substitution of Nd for Ce in CeCoIn_5 introduces disorder in the crystal lattice, which is observed, for instance, in the reduced residual resistivity ratio of synthesized crystals (see chapter 5.1). Thus, absorption effects are dominant in this case.

The correction depends on the geometrical shape of the sample with respect to \mathbf{k}_i and \mathbf{k}_f . The spacial extent of the experimental realizations (powder or single crystal) was simulated in the considered scattering condition and the average neutron path, $\langle d(\mathbf{Q}) \rangle$, was modeled using a finite element method. The attenuation length,

$$d_\mu = \mu^{-1} = \frac{V_0}{\sigma_{tot}} \frac{|\mathbf{k}_i|}{|\mathbf{k}_f|}, \quad (3.22)$$

was estimated from the unit cell volume V_0 and the total scattering cross section $\sigma_{tot} = \sum_i n_i (\sigma_{coh,i} + \sigma_{inc,i} + \sigma_{abs,i})$. n_i is the number of atoms of the element i in the unit cell and $\sigma_{coh,i}$, $\sigma_{inc,i}$ and $\sigma_{abs,i}$ is the coherent, incoherent and absorption cross section, respectively. The absorption correction, $Ab(\mathbf{Q})$, at a wave-vector transfer \mathbf{Q} reads:

$$Ab(\mathbf{Q}) = e^{-\langle d(\mathbf{Q}) \rangle / d_\mu}. \quad (3.23)$$

^{||}The coherent elastic scattering at a Bragg peak position is treated by the extinction and, thus, excluded here.

3.5 EXPERIMENTAL TECHNIQUES

Neutron scattering probes the dynamic scattering function, $S(\mathbf{Q}, \omega)$, that gives access to the microscopic interactions in a material [14–16]. Six orders of magnitude in \mathbf{Q} and twelve orders of magnitude in ω can be covered by various neutron scattering setups [14]. Thus, it is necessary to choose the instrument that is optimal for the addressed scientific question. The following discussion is focussed on the experimental techniques that are used in this thesis.

3.5.1 Powder Diffraction.

Nuclear and magnetic order in experimental realizations can be probed by means of the elastic differential cross sections that are written in Eq. 3.7 and 3.15. Powder diffraction is an excellent technique to study these properties, in particular when the structure or the magnetic wave-vector is unknown. A random orientation of the crystallites transforms the sharp Bragg condition into Debye-Scherrer cones at constant \mathbf{Q} -moduli [14]. These cones are resolved in an angular-dispersive diffraction mode, because a Bragg angle, θ , triggers an elastic signal at the scattering angle 2θ .

The method requires a monochromatic neutron beam that is scattered at the sample and detected by a position sensitive ^3He -detector covering a large area of scattered angles [14, 170]. The schematic view of the high-resolution powder diffractometer HRPT at SINQ is shown in Fig. 3.1 and covers an angular range of 160° with a resolution of 0.05° [170].

The mosaicity of the monochromator crystal and the angular divergence of the neutron beam stretch the δ -function of the $|\mathbf{Q}|$ -dependent Bragg condition into a Gaussian [14]. Its line-width, $\Gamma_{2\theta}$, is parametrized by the instrument-dependent coefficients U , V and W and is given by [14]:

$$\Gamma_{2\theta} = \sqrt{U \tan^2 \theta + V \tan \theta + W}. \quad (3.24)$$

The scattered intensity at $2\theta_i$ that arises from a powdered material and that features magnetic long-range order is modeled by [14]:

$$I(2\theta_i) = BG(2\theta_i) + L(2\theta_i) Ab(2\theta_i) \left(N_0 \frac{(2\pi)^3}{V_0} m_N(2\theta_N^{hkl}) |F_N(2\theta_N^{hkl})|^2 e^{-4 \ln 2 \left(\frac{2\theta_i - 2\theta_N^{hkl}}{\Gamma_{2\theta_i}} \right)^2} + N_M \left(\frac{\gamma r_0}{2} \right)^2 \frac{(2\pi)^3}{V_M} m_M(2\theta_M^{hkl}) |F_M(2\theta_M^{hkl})|^2 e^{-4 \ln 2 \left(\frac{2\theta_i - 2\theta_M^{hkl}}{\Gamma_{2\theta_i}} \right)^2} \right), \quad (3.25)$$

where $BG(2\theta_i)$ is the background at $2\theta_i$ that results mainly from incoherent scattering. In this thesis the background was fitted with a polynomial function. N_0 (N_M) denotes the number of nuclear (magnetic) unit cells, V_0 (V_M) is the structural (magnetic) unit cell volume, γ substitutes the gyromagnetic ratio, r_0 is the classical electron radius and $F_N(2\theta_N^{hkl})$ ($F_M(2\theta_M^{hkl})$) describes the nuclear (magnetic) structure factor of the Bragg reflection (h , k , l) at $2\theta_N^{hkl}$ ($2\theta_M^{hkl}$) that is closest to $2\theta_i$. The multiplicity of the nuclear or magnetic Bragg peak is represented by $m_N(2\theta_N^{hkl})$ or $m_M(2\theta_M^{hkl})$, respectively**. $L(2\theta_i)$ is the geometrical Lorentz factor, enhancing the signal at small and large $|\mathbf{Q}|$ -values. In a powder diffraction experiment the factor equals $L(2\theta_i) = 1/(\sin(\theta_i)\sin(2\theta_i))$. $Ab(2\theta_i)$ describes the correction that is attributed to absorption.

**The multiplicity of $m_N(2\theta_N^{100})$ in $P4/mmm$, for instance, is 4, whereas $m_N(2\theta_N^{001}) = 2$.

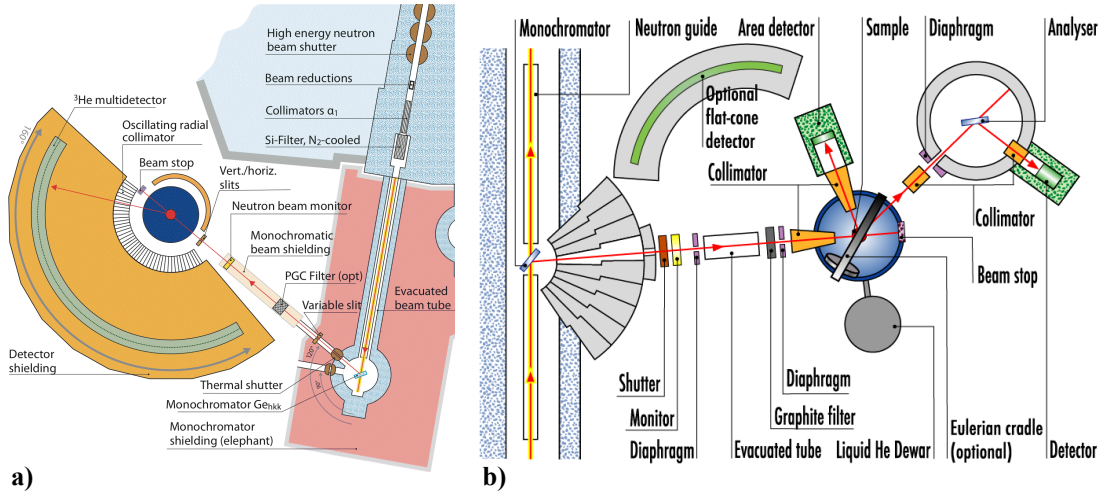


FIGURE 3.1: Powder and Four-Circle Diffractometer. a) Schematic view of the angular-dispersive high-resolution powder diffractometer HRPT at SINQ. b) Illustration of the four-circle diffractometer D10 at the ILL. Taken from [170, 171].

The analysis of the diffraction patterns conducted in this thesis is based on the Rietveld method and performed with the FullProf suite [169, 172]. The program uses an iterative process to minimize the residuals between the observed and calculated structure factors F_{obs} and F_{calc} . The goodness of the fit is evaluated by the crystallographic R_f -factor [173]:

$$R_f = \frac{\sum_h |F_{obs,h} - F_{calc,h}|}{\sum_h |F_{obs,h}|}. \quad (3.26)$$

3.5.2 Single Crystal Diffraction.

The randomly oriented crystallites in powdered samples distribute the Bragg peak intensity over the entire angular range at constant $|Q|$ [14]. This limits the sensitivity to magnetic moments sizes that are typically larger than $\mu \approx 0.5\mu_B$. In cases where magnetic signals with smaller moments are studied, neutron diffraction on single crystals is performed.

Structural and magnetic Bragg reflections in a standard single crystal diffraction experiment are accessed by an Eulerian cradle that enables three independent rotations. Additional to the ω -axis (\perp to the scattering plane), the single crystal can be rotated perpendicular to ω (χ -axis) and 90° to χ (ϕ -axis). This instrumental setup is a four-circle diffractometer, where the rotation of the detector in the ω -plane represents the fourth rotation.

The schematic view of the four-circle diffractometer D10 at the ILL is displayed in Fig. 3.1b. The instrument reveals various detector options, including a two-dimensional area detector, a flat-cone detector and an analyzer option with a single-counter ³He detector [171]. The advantage of an analyzer unit in a diffraction experiment is the highly efficient reduction of the

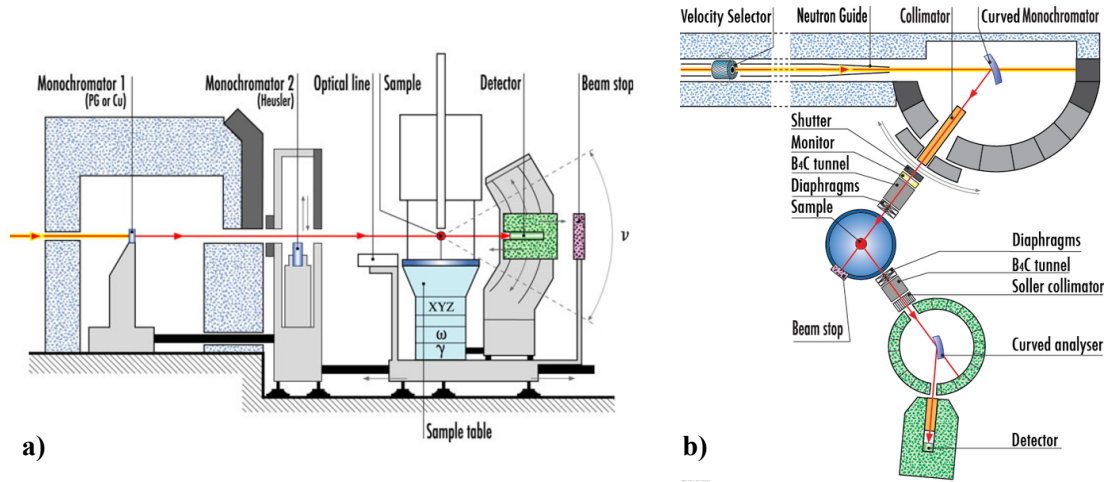


FIGURE 3.2: Lifting-Counter Two-Axis Diffractometer and Triple-Axis Spectrometer. **a)** Schematic view of the thermal neutron lifting-counter two-axis diffractometer D23 at the ILL. **b)** Illustration of the cold-neutron three-axis spectrometer IN12 at the ILL. Taken from [174, 175].

background that arises from inelastic scattering of the sample and the environment. The analyzer (third axis in Fig. 3.1b) is oriented such that only neutrons with $|\mathbf{k}_f| = |\mathbf{k}_i|$ are diffracted into the detector unit.

The neutron intensity is directly related to the coherent elastic differential cross section via:

$$I(\mathbf{Q}) = BG(\mathbf{Q}) + L(\mathbf{Q})Ab(\mathbf{Q}) \left(\frac{d\sigma}{d\Omega} \right)_{coh}^{el}(\mathbf{Q}), \quad (3.27)$$

where the background, $BG(\mathbf{Q})$, at wave-vector $\mathbf{Q} = \mathbf{k}_f - \mathbf{k}_i$ originates from incoherent elastic scattering of the single crystal and the sample environment. $Ab(\mathbf{Q})$ is the absorption correction that is discussed in chapter 3.4. The elastic cross section consists of the coherent nuclear and magnetic contributions that are written in Eq. 3.7 and 3.15. Here, the δ -function of the Bragg condition is replaced by a Gaussian with a finite line-width that results from instrumental resolution effects. The integrated Bragg peak intensity is directly proportional to the square of the structure factor and is usually measured by an ω -rotation. This yields a Lorentz factor $L(\mathbf{Q}) = 1/\sin(2\theta_Q)$, where $2\theta_Q$ is the position of the detector with respect to the incoming neutron beam that corresponds to the wave-vector transfer \mathbf{Q} [14, 16].

Single crystal neutron diffraction experiments can be performed under magnetic fields along specific crystallographic directions. In this case the single crystal is placed in a cryogenic magnet (see chapter 3.6) that prevents the use of an Eulerian cradle. In consequence, the angular range is limited to the horizontal scattering plane (ω -rotation) in a standard two-axis diffractometer or when a triple-axis spectrometer with $|\mathbf{k}_i| = |\mathbf{k}_f|$ is employed (see 3.2b).

Two-axis diffractometers with lifting-arm detectors, such as D23 at the ILL and Zebra at

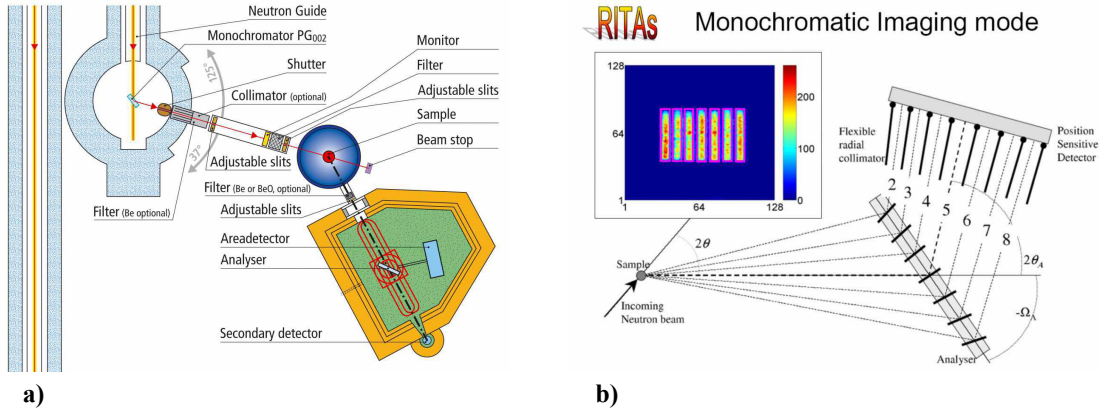


FIGURE 3.3: The Triple-Axis Spectrometer RITA-II. a) Schematic view of the cold-neutron three-axis spectrometer RITA-II at SINQ. b) Illustration of the multi-blade analyzer and the position sensitive ^3He -detector of RITA-II. Taken from [177].

SINQ, enable the investigation of Bragg reflections up to $\nu = 12^\circ$ above the scattering plane, even when cryogenic magnets are used^{††} [174]. The schematic view of D23 is shown in Fig. 3.2a. The detector angle, 2θ , consists of the in-plane rotation, γ , and the out-of-plane angle, ν , which change the geometrical Lorentz correction factor to $L(\mathbf{Q}) = 1/(\sin(\gamma_Q)\cos(\nu_Q))$ [176].

Single crystal diffraction was also conducted on the triple-axis spectrometer RITA-II at SINQ. The schematic view of the instrument is shown in Fig. 3.3a. The analyzer unit consists of nine blades that diffract the scattered neutrons onto individual position-sensitive ^3He -detectors (see Fig. 3.3b) [177]. This allows a simultaneous measurement of different \mathbf{Q} s for a fixed sample position. Furthermore, the position-sensitive detectors access out-of plane angles of $\pm 2^\circ$ when the beam divergence is restricted^{‡‡} by the vertical 15 T cryogenic magnet available at SINQ [177, 178].

3.5.3 Inelastic Neutron Scattering.

Neutron scattering allows to study the elementary structural and magnetic excitations of a material by means of the inelastic dynamical scattering function, $S(\mathbf{Q}, \omega)$ with $\omega \neq 0$. While phonons are the basic collective lattice excitations of all crystalline structures, the nature of the magnetic excitations depend on the corresponding exchange coupling [4, 5, 14].

The dominating magnetic energy scale in crystals containing $4f$ -electrons is governed by the crystal field splitting (see chapter 2.1.1) that is usually of the order of 10-100 meV [97]. A transition from the ground state multiplet into a higher energy level arises from a local excitation that is attributed to a single magnetic site. $S(\mathbf{Q}, \omega)$ can be expressed exactly if the

^{††}The motor of D23 reveals an angular range of $-28 < \nu < 29^\circ$ that is reduced to $-2 < \nu < 12^\circ$ by the opening windows of the vertical 12 T cryogenic magnet used in our experiments [174].

^{‡‡}Without restrictions an opening angle of $\pm 3^\circ$ is obtained [177].

total angular momentum, \mathbf{J} , is a good quantum number. Thus, inelastic neutron scattering enables a direct measurement of the crystal field scheme.

The counterpart of crystal field transitions are collective magnetic excitations that restore the broken symmetry in a magnetically ordered phase [97]. Here, it is necessary to distinguish the two extreme cases, where magnetic order arises either from a small or large Fermi surface (see chapter 2.1). In metallic systems that feature unhybridized f -bands, local moment magnetism is mediated via the RKKY interaction that is equivalent to a superexchange in insulators [5]. The elementary collective excitations are dispersing spin waves that yield a magnetic susceptibility, which can be modeled within the random phase approximation [14, 97]. The dynamic local susceptibility is connected to $S(\mathbf{Q}, \omega)$ via the dissipation fluctuation theorem (see Eq. 3.14). In rare-earth metals typical exchange couplings $|J_{RKKY}| \approx 1\text{-}10$ meV are found [97].

Magnetic excitations are more complex in HF systems, where the hybridized state leads to quenched localized moments [12]. Here, magnetic order arises from a Fermi surface instability that triggers a gap in reciprocal space and a corresponding spin-density modulation in real space (see chapter 2.1.2) [47]. The SDW features two collective excitations that are attributed to the amplitude and the phase of the SDW [4]. At large wave-vectors they merge into the Stoner continuum that is associated to particle-hole excitations across the SDW gap [97]. Neutron scattering allows to probe the excitations via the fluctuation dissipation theorem (see Eq. 3.14 and 2.5). It is noted that the interpretation of the magnetic excitation spectrum is complicated in materials described by the two fluid model consisting of finite small and large Fermi surface fractions.

In this thesis inelastic neutron scattering was used to study the magnetic excitations inside a superconducting phase. The description of the superconducting spin resonance in unconventional spin-singlet condensates is given in chapter 2.3.3. The magnetic excitation reveals a peak in the magnetic susceptibility that can be probed with neutrons.

A triple-axis spectrometer that is used in the inelastic mode ($|\mathbf{k}_i| \neq |\mathbf{k}_f|$) is an excellent instrument to measure $S(\mathbf{Q}, \omega)$ in a highly resolved and controlled manner [14, 16]. Here, the analyzer (third axis in Fig. 3.2b) is oriented such that only neutrons with a specific energy transfer $\hbar\omega = \hbar^2/(2m)(|\mathbf{k}_i|^2 - |\mathbf{k}_f|^2)$ are diffracted into the detector unit. The dynamic susceptibility can be measured for a particular line in reciprocal space by means of an appropriate rotation of the sample at a fixed energy transfer (constant- E scan). In contrast, the energy dependence of an excitation at a specific point in reciprocal space is studied via rotation of the monochromator (constant- \mathbf{Q} scan). The orientation of the analyzer is usually fixed, because in this setup the conversion from neutron intensity to the inelastic cross section requires only minimal corrections [14].

The detailed specifications of the employed instruments are described in the experimental details prior to the corresponding results (see chapter 5.2.1, 5.3.2, 5.4.1 and 5.5.1).

3.6 SAMPLE ENVIRONMENT

Strongly correlated electron systems are quantum materials in which different degrees of freedom are intrinsically coupled [32]. Their ground state properties are often observed at low temperatures only and the application of magnetic fields or pressure may be required to decouple the microscopic exchange interactions.

Neutron scattering is an excellent technique, by which structural and magnetic properties can be studied under such conditions [14–16]. The particles interact only weakly with their surrounding, enabling the use of a complex sample environment. In this work we tuned the ground state properties via chemical substitution and magnetic field. Thus, the following discussion is focused on cryostats, cryogenic magnets as well as on ^3He inserts and dilution refrigerators.

Cryostats and cryogenic magnets are made of aluminium close to the sample position, because the material reveals a tiny incoherent and absorption cross section [164, 179]. In contrast, the cooling devices that are connected directly to the sample are often made of Copper as it features a small heat capacity.

3.6.1 Cryostats and Cryogenic Magnets.

Experiments at zero magnetic field are mainly conducted in cryostats that can access temperatures between $T = 1.5$ and 300 K. So-called orange cryostats from *Scientific Products* may be used on powder and two-axis diffractometers as well as on triple-axis instruments. The schematic design of the device is depicted in Fig. 3.4a [180]. The sample is mounted on a stick with appropriate diameter. It is inserted into the core of the cryostat that is surrounded by a liquid ^4He bath [179, 181]. The thermal shielding between the ^4He bath and the outer world is realized by a nitrogen bath. The cooling of the sample is achieved via a continuous transfer of liquid ^4He into the heat exchanger. The evaporated liquid is pumped along the tube around the sample stick, where radiation baffles enable the thermal contact with the sample holder [180]. The pumped ^4He is collected by a recovery line and the cold valve control, also called needle valve, allows an accurate manipulation of the sample cooling rate.

The various rotational degrees of freedom complicate the cooling concept on a four-circle diffractometer. Here, the ^4He bath is placed next to the instrument and the sample is covered by an aluminium shielding [182]. This head is connected with the bath using helium transfer lines with rotating joints that allow a free movement of the cradle angles [179]. The cooling of the sample is established by pumping evaporated He gas through the space between the sample and the shielding.

The vertical cryogenic magnets that are provided by *Oxford Instruments* keep the cooling concept of the orange cryostats, but add two solenoid coils to their design [183]. The coils, made of superconducting Nb_3Sn wires, are placed above and below the Al window and are cooled by the ^4He bath (see Fig. 3.4b). The magnetic field is produced by circulating superconducting currents in the two coils. It can be changed by an external switch that heats a small part of the wire above the critical temperature. Subsequent to the modification of the current in the solenoid coils, the switch heater is turned off. Finally, the external current source ramps down, after the entire coil has reentered the superconducting phase.

3.6.2 ^3He Inserts and Dilution Refrigerators.

^3He reveals a substantially larger vapor pressure than ^4He [179]. In contrast to ^4He ($T_c \approx 2.2$ K), the isotope is not superfluid for temperatures above several Millikelvins, which prevents heat transfer problems during experiments. The production costs of ^3He are, however, approximately ten times higher than the ones of ^4He , which is the main disadvantage of using ^3He as a cooling medium. In consequence, a closed system with ^3He gas is used in experiments where temperatures between $T = 0.3$ and 1.5 K are required. The insert fits into the core of the

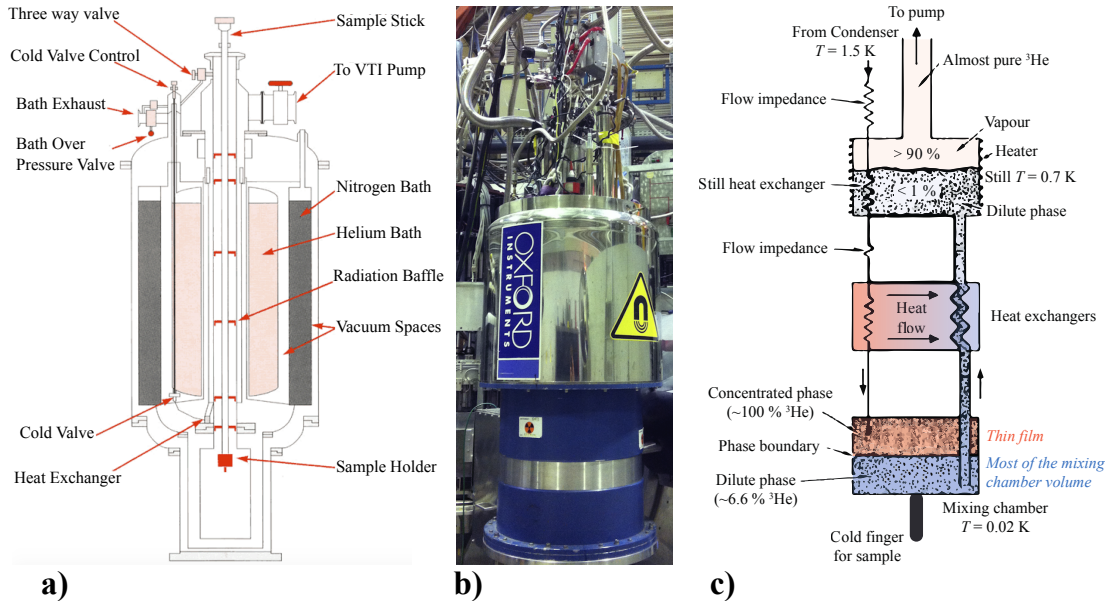


FIGURE 3.4: Cryostats, Cryogenic Magnets and Dilution Refrigerators. a) Schematic design of an orange cryostat, produced by *Scientific Products*. b) Picture of the vertical CRG-CEA 12 T magnet. Schematic view of a dilution refrigerator. Taken from [24, 180].

cryostat or the cryogenic magnet and the gas is turned into a liquid ($T_{3He} = 3.3$ K) using 4He as a cooling medium. Sample temperatures below $T = 1.5$ K are achieved by pumping on the evaporated 3He gas [179].

3He - 4He dilution refrigerators are used to conduct experiments down to $T \approx 20$ mK and are based on the xT -phase diagram of the two He isotopes. The superfluid transition temperature of 4He is suppressed when it is diluted with the Fermi liquid 3He [179]. At a 3He concentration larger than 67.5% and temperatures below $T \approx 0.9$ K the phase boundary between the superfluid condensate and the normal fluid phase meets the phase-separation line. Here, 3He and 4He can mix for certain concentrations only, which leads to two separated phases with a low concentration of 3He (diluted phase) and a concentrated 3He phase. At lowest temperatures, $T \approx 20$ mK, the diluted phase reveals 6.6% of admixed 3He .

The schematic view of the refrigerator is shown in Fig. 3.4c where the diluted phase is depicted in blue and the concentrated phase in orange color. Because of gravity, the concentrated phase is separated from the diluted one that is on the bottom of the mixing chamber. 3He of the diluted phase flows from the mixing chamber into the Still because of an osmotic pressure difference [179]. The Still is operated at $T \approx 0.7$ K, where 3He reveals a higher vapor pressure than 4He . Thus, the evaporation of almost pure 3He yields the pressure difference between the two chambers. The 3He concentration in the mixing chamber is maintained by the transition of the isotope from the concentrated into the diluted phase. This mixing process features a latent

heat that is used to cool the sample. Finally, ^3He that is evaporated in the Still recondenses via heat exchange with the ^4He -bath and is guided back to the concentrated phase.

Dilution inserts are also available for four-circle cryostats, where a special geometry is needed to overcome the gravitation problem of the phase separation [184].

Chapter 4

The Pauli-Limited Heavy-Fermion d -wave Superconductor CeCoIn₅

The HF material CeCoIn₅ reveals one of the highest critical temperatures, $T_c = 2.3$ K, among all Ce-based superconductors [17]. Single crystals can be grown with very little impurities featuring residual resistance ratios (RRR) up to values of 300 and electronic mean free paths larger than one micrometer [185, 186]. The high tuneability of the ground state properties by means of magnetic field, pressure and chemical substitution and its proximity to the cuprates lead to a plethora of experimental and theoretical studies on this system over the last years.

4.1 HEAVY-FERMION PROPERTIES

CeCoIn₅ is a member of the series Ce_{*n*}M_{*m*}In_{3*n*+2*m*} ($M = \text{Co, Ir, Rh}$) that is shown in Fig. 4.1a [131]. The parent structure is defined by CeIn₃ ($n = \infty$ and $m = 0$) that crystalizes in the face-centered cubic space group $Pm\bar{3}m$. Other members are constructed by n -fold CeIn₃ layers that are separated by m -fold MIn₂ sheets. This gives rise to a tetragonal structure that becomes more two dimensional for increasing n and m . CeMIn₅ crystalizes in the space group $P4/mmm$ ($a = 4.6$ Å and $c = 7.54$ Å for $M = \text{Co}$) and reveals two inequivalent In sites. One site appears in the MIn₂ building block and is detached from the other one that is found in the tetragonal basal Ce-In plane.

The Fermi surface of CeCoIn₅ is displayed in Fig. 4.1b and characteristic of all CeMIn₅ compounds [54, 188–193]. It features a quasi-two dimensional structure with tubes along the tetragonal c -axis that are centered around the middle of the Brouillon zone, Γ , and around the corners M . Thus, two dimensional-fluctuations that arise in the basal Ce-In plane are important in these so-called 115 compounds, but their ground state properties cannot solely be attributed to such correlations.

The parent compound, CeIn₃, is constructed only from one Ce-In building block and reveals antiferromagnetic order within a small Fermi surface at ambient pressure [133, 194]. Under pressure, T_N linearly decreases and extrapolates to zero at a critical value $p_c = 2.6$ GPa, where the center of an unconventional superconducting phase is found [11]. CeMIn₅ is very sensitive to the isovalent transition-metal ion $M = \text{Co, Ir and Rh}$, despite no apparent trend in the Ce-In bond lengths/angles is observed in the family [195]. While CeCoIn₅ and CeIrIn₅ are superconductors below $T_c = 2.3$ and 0.4 K, respectively, CeRhIn₅ features antiferromagnetic

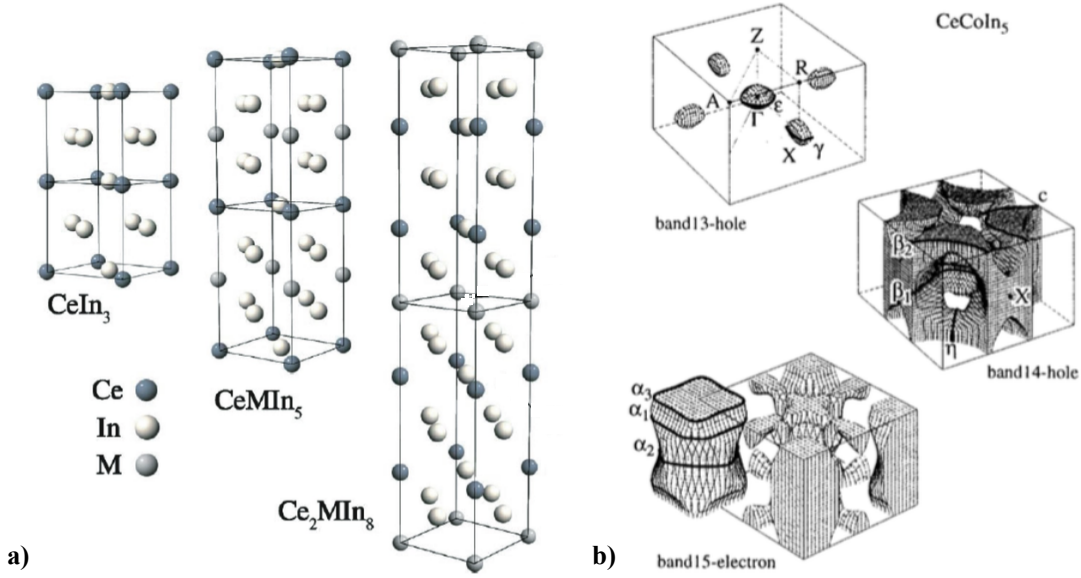


FIGURE 4.1: Crystal Structure and Fermi Surface. a) Crystal structure of the series $\text{Ce}_n\text{M}_m\text{In}_{3n+2m}$ ($M = \text{Co}, \text{Ir}, \text{Rh}$) for $n = \infty, 1, 2$ and $m = 0, 1$. b) Fermi surface of CeCoIn_5 measured by de Haas-van Alphen oscillations. Taken from [187, 188].

order below $T_N = 3.5$ K at ambient pressure [131]. A pressure-induced QPT is established in the latter compound, at which the Fermi surface is substantially enlarged [39]. Moreover, it is believed that the f -electrons are more itinerant in CeIrIn_5 than in CeCoIn_5 that is located close to a SDW quantum critical point [20, 195].

The comparison underlines that the choice of the transition-metal ion in CeMIn_5 is crucial for the degree of hybridization between the $4f$ -electrons and the conduction band. Recent systematic x-ray absorption spectroscopy results show that the degree of itinerancy among CeRhIn_5 , CeCoIn_5 and CeIrIn_5 scales with the out-of-plane anisotropy of the crystal-electric field ground state wave function that tunes the $4f$ -orbital overlap with the out-of-plane In $5p$ -orbitals [196]. The scenario is supported by dynamical mean-field calculations that predict a strong hybridization among these bands in CeIrIn_5 and CeCoIn_5 [195]. This is in line with angle-resolved photoemission spectroscopy (ARPES) measurements on CeCoIn_5 that show only a moderate $4f$ -hybridization for the most pronounced two-dimensional band in the tetragonal plane [192].

Heavy effective masses in this material are also reflected in the strongly enhanced Sommerfeld constant, $\gamma = 290$ mJmol $^{-1}$, just above T_c [17]. The same authors provide evidence for a coherent Kondo lattice below $T_K \approx 45$ K. Recent ARPES results on samples that were cleaved perpendicular to the c -axis demonstrated that hybridization occurs mainly around the Γ -point (see Fig. 4.2a and b) [54]. Figure 4.2c displays high statistic momentum distribution cuts in

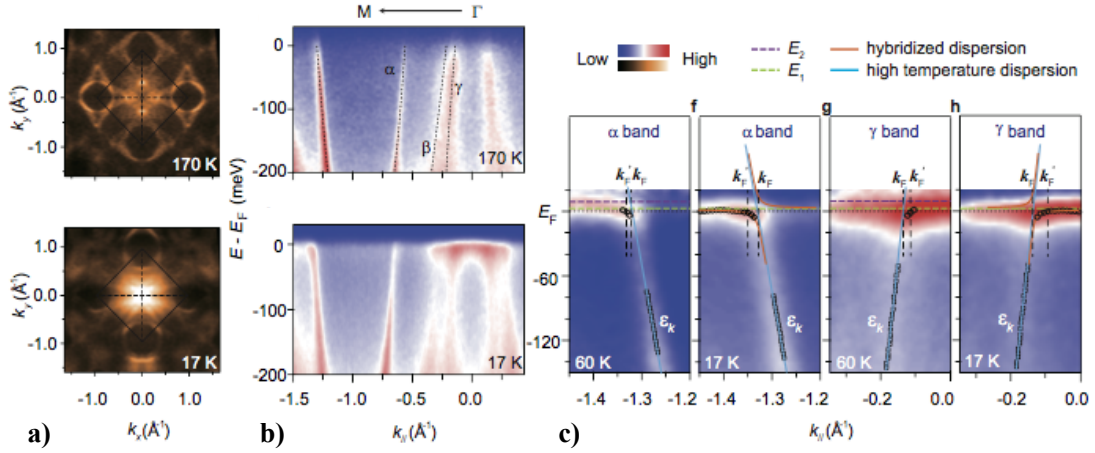


FIGURE 4.2: Angle-Resolved Photoemission Spectroscopy on CeCoIn₅. a) Fermi surface of CeCoIn₅ measured on the $4d \rightarrow 4f$ resonance of Ce above and below the Kondo coherence temperature. b) Momentum distribution cuts in the Γ - M -direction at $T = 170$ and 17 K. c) High statistic cuts near the Fermi crossing of the α - and γ -band. Taken from [54].

the diagonal direction of the Brillouin zone ($\Gamma - M$) that provide evidence for the emergence of a direct Kondo gap with $v \approx 30$ meV.

4.2 PAULI-LIMITED SUPERCONDUCTIVITY NEAR A SDW QUANTUM CRITICAL POINT

It is believed that the hybridized electrons trigger the superconducting ground state in HF materials [73]. The ARPES results depicted in Fig. 4.2, thus, indicate a $d_{x^2-y^2}$ -wave symmetry in superconducting CeCoIn₅ with a gap along the tetragonal a -axis and nodal planes along the $(1, 1, 0)$ direction in reciprocal lattice units (r. l. u.). This gap symmetry has been suggested first by macroscopic measurement, such as the temperature and angular dependent thermal conductivity and the angular dependence of the specific heat [198–200]. Subsequent point-contact spectroscopy and quasiparticle interference studies provided evidence for a d -wave amplitude $\Delta E \approx 0.6$ meV [18, 19, 197]. The symmetry of the superconducting order parameter is consistent with the emergence of a spin resonance below T_c [92]. High-resolution inelastic neutron scattering results have shown that the resonance arises at a wave-vector transfer $\mathbf{Q} = (q, q, 0.5)$ with $q \approx 0.45$ and for an energy transfer $\Delta E = 0.6$ meV [201].

A close connection between superconductivity and magnetism in CeCoIn₅ is revealed by its vicinity to a SDW quantum critical point [17, 20, 22, 202–204]. The normal state specific heat and electrical resistivity feature non-Fermi liquid behavior in their temperature dependence [17, 22, 202, 203]. This suggests the presence of quantum critical fluctuations, which have been determined to be of antiferromagnetic nature using nuclear magnetic resonance spectroscopy

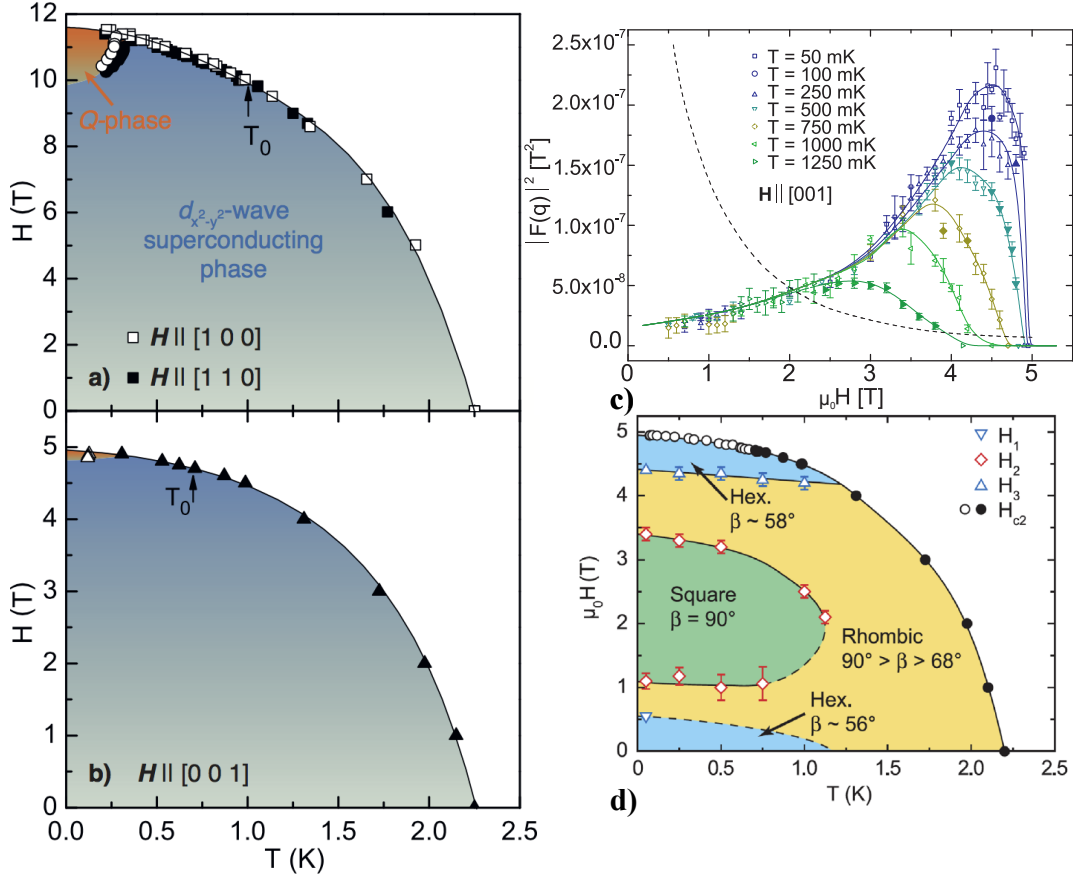


FIGURE 4.3: HT -phase Diagram of CeCoIn₅. **a)** Superconducting phase of CeCoIn₅ for $H \parallel [1 0 0]$ and $H \parallel [1 1 0]$ with the Q -phase below $T = 300$ mK and above $\mu_0 H^p = 9.8$ T. **b)** Superconducting phase of CeCoIn₅ for $H \parallel [0 0 1]$. **c)** Square of the magnetic vortex form factor as a function of magnetic field strength for $H \parallel [0 0 1]$. The dashed line represents the field dependence expected from the Abrikosov-Ginzburg-Landau approach. **d)** Vortex lattice phase diagram for $H \parallel [0 0 1]$. Taken from [22, 205, 206].

[204]. Finally, the quantum critical point has been located at zero field by means of the temperature dependent Grüneisen parameter [20]. The origin of the magnetic instability and its relation to superconductivity is still unclear. Its presence, however, provides an environment of strong fluctuations, where novel physical phenomena may be expected.

CeCoIn₅ displays an anisotropic superconducting phase as a function of the magnetic field orientation (see Fig. 4.3a and b) [21, 22]. At lowest temperatures superconductivity is suppressed at $\mu_0 H_{c2} = 5$ T for a field perpendicular to the tetragonal plane, but the condensate remains stable up to $\mu_0 H_{c2} = 11.5$ T for fields applied in the basal plane. Here, a 4% increase of the upper critical field is observed when the field is rotated from the d -wave node towards

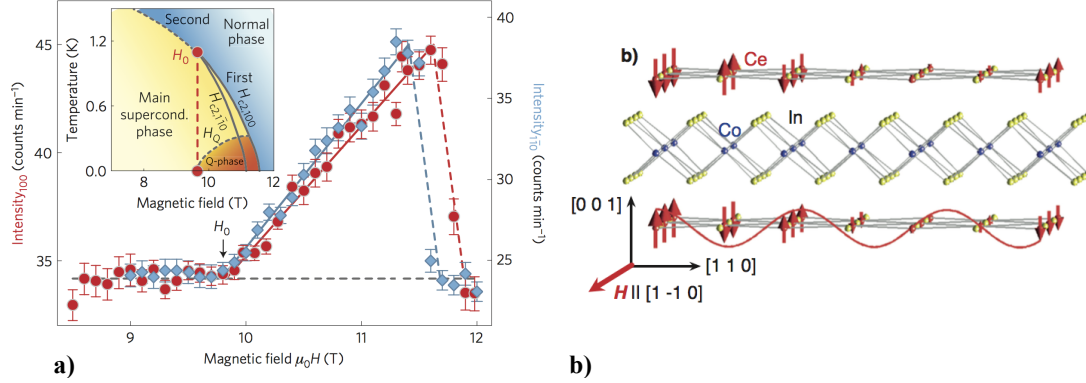


FIGURE 4.4: The Q-phase of CeCoIn₅. **a)** Field dependent neutron diffraction results below $T = 100$ mK at $\mathbf{Q} = (0.45, 0.45, 0.5)$ for $H \parallel [1 0 0]$ in red and $H \parallel [1 -1 0]$ in blue. Inset: HT -phase diagram. **b)** Magnetic structure of the SDW in the Q-phase. Taken from [23, 24, 88].

the maximal gap (see Fig. 4.5a inset).

The temperature dependence of $H_{c_2}(T)$ reveals an orbital limiting field $\mu_0 H^{orb} = 35$ and 13 T for $H \parallel [1 0 0]$ and $H \parallel [0 0 1]$, respectively, which is considerably higher than $H_{c_2}(0)$ [21, 22]. This provides strong evidence that close to the upper critical field Pauli paramagnetic effects gain in importance, which is also revealed by the suppression of superconductivity in a first-order transition for critical fields larger than $\mu_0 H^p = 9.8$ and 4.7 T, respectively [21, 22, 207]. Microscopic evidence for strong spin paramagnetic effects at high fields has been provided first by de Haas-van Alphen oscillations [208], and has been further investigated via small-angle neutron scattering [209, 210].

These experiments reveal an increasing magnetic form factor of the superconducting vortices with magnetic fields that are oriented along the basal plane and perpendicular to it (see Fig. 4.3c) [209, 210]. The behavior is in contrast to all previously studied type-II superconductors that show a decreasing form factor and that is commonly modeled within an Abrikosov-Ginzburg-Landau approach [211]. This provides evidence for the emergence of an additional scattering cross section in CeCoIn₅ that has been attributed to paramagnetic moments around the vortex core or to antiferromagnetic fluctuations [212–216].

The vortex lattice phase diagram as a function of temperature and magnetic field is displayed in Fig. 4.3d for $H \parallel [0 0 1]$. It shows a cascade of geometric transitions as the field is increased with a reentrant triangular structure below the upper critical field [206]. While the transitions at low fields are expected [25, 217], the triangular phase below H_{c_2} is thought to arise from paramagnetic or antiferromagnetic effects [206].

4.3 THE Q-PHASE OF CeCoIn_5

Thermal heat capacity results provide evidence for a supplementary phase (Q-phase) inside the superconducting condensate of CeCoIn_5 that exists above $\mu_0 H^p = 9.8$ T and below $T = 300$ mK for $H \perp c$ [22, 23]. The phase consists of SDW order that arises at a wave-vector transfer $\mathbf{Q} = (q, \pm q, 0.5)$ with $q \approx 0.44$, identical to the reciprocal space position of the spin resonance [23, 88, 144–146, 201]. The magnetic structure is amplitude modulated along the c -axis with an ordered moment $\mu \approx 0.15\mu_B$ (see Fig. 4.4b) [23, 88, 145]. Magnetic order appears from a second-order mean-field-like transition at the phase boundary of the Q-phase and collapses in a first-order transition at the superconducting upper critical field. This demonstrates that the Q-phase features a multicomponent magneto-superconducting ground state that emerges from a field-induced QPT at $\mu_0 H^p = 9.8$ T (c.f. Fig. 4.4b). SDW order is suppressed upon rotating the magnetic field 17° towards the tetragonal c -axis, which coincides with the angle where H_{c2} decreases below H^p [188, 218]. This demonstrates that Pauli paramagnetic effects are crucial for the development of the Q-phase. It is noted that heat capacity results have also suggested a supplementary phase for $H \parallel [0\ 0\ 1]$ [21]. However, no microscopic evidence for magnetic order has been found in this phase yet [24].

The multicomponent ground state of the Q-phase is hypersensitive to the magnetic field direction in the tetragonal basal plane [88, 219]. Neutron diffraction studies along the two wave-vectors $\mathbf{Q}_{h,v} = (q, \pm q, 0.5)$ with $q \approx 0.44$ showed that only one of both domains is populated for all in-plane field directions (see Fig. 4.5a and b) [88]. As the magnetic field is rotated around the crystalline a -axis the modulation direction of the SDW is switched by 90° . At $\mathbf{H} \parallel [1\ 0\ 0]$, where both domains are equivalent by symmetry, a first-order transition with a hysteresis of $\Delta\Psi \approx 0.2^\circ$ is found (see Fig. 4.5c). Since the magnetic moment is oriented perpendicular to the field, the selection of one modulation direction cannot originate from a Zeeman term that couples the field to the magnetic structure.

A similar behavior is observed in the superconducting quasiparticle excitation spectrum that was examined by thermal conductivity [219]. Here, the temperature normalized thermal conductivity response, κ/T , is measured for heat currents applied along the d -wave node, $\mathbf{J} \parallel [1\ 1\ 0]$, as the magnetic field turned through the a -axis (Fig. 4.5d and e). The angle between \mathbf{J} and the magnetic field, \mathbf{H} , is denoted as θ that probes quasiparticle excitations perpendicular to the populated SDW for $\theta < 45^\circ$ (case $\Psi > 0$ in Fig. 4.5a and b). At $\theta = 45^\circ$ the modulation direction of the SDW is switched and triggers a jump in κ/T (see Fig. 4.5e). We point out that quasiparticle excitations across the SDW gap are probed for $\theta > 45^\circ$, but a larger κ/T is observed for this configuration when compared to the case $\theta < 45^\circ$ where the SDW modulation along \mathbf{J} is suppressed.

Several theoretical models have been proposed to explain the microscopic mechanism of the Q-phase [147–158, 220–222], but only a few of them can account for the high sensibility to the in-plane magnetic field direction [147, 153, 158, 220–222]. The condensation of the spin resonance into the ground state is possibly the most promising microscopic theory that directly intertwines magnetic order with superconductivity (see also chapter 2.4.3) [147]. This scenario is supported by inelastic neutron scattering results that show a splitting of the superconducting resonance for increasing magnetic fields. The field dependence of the lower mode extrapolates to zero close to the Q-phase boundary [223, 224]. In the exciton scenario, the magnetic mono-domain state in the Q-phase is attributed to spin-orbit effects that also trigger the change of

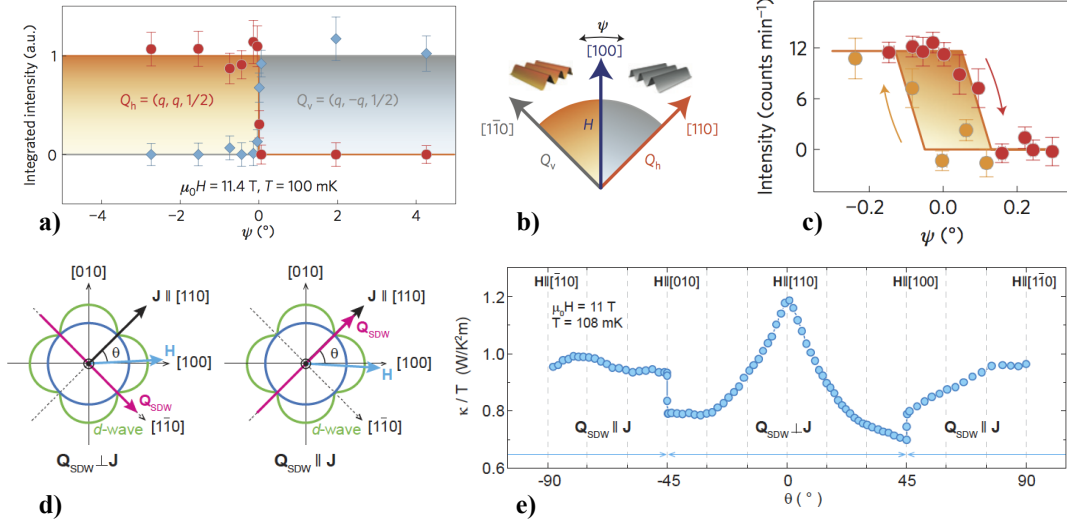


FIGURE 4.5: Switching of the Multicomponent Ground State in CeCoIn₅. **a)** Magnetic Bragg peak intensity of the two domains $Q_h = (q, q, 1/2)$ and $Q_v = (q, -q, 1/2)$ with $q = 0.44$ as a function of ψ . **b)** ψ defines the angle between the tetragonal a -axis and the magnetic field direction in the basal plane. **c)** Hysteresis of magnetic Bragg peak intensity as a function of ψ . **d)** Schematic illustration of the thermal conductivity experiment that probed the heat current response $J \parallel [110]$ as a function of the magnetic field direction in the basal plane. **e)** Thermal conductivity divided by temperature as a function of field orientation measured in the Q-phase. Taken from [88, 219].

modulation direction as the magnetic field is rotated around the a -axis [220]. The model, however, cannot directly predict the thermal conductivity results that suggest the emergence of an additional gap perpendicular to the SDW modulation direction [219].

This aspect is resolved in other theories where a supplementary superconducting order parameter arises in the Q-phase that couples the superconducting d -wave order parameter to the SDW [153, 221, 222]. The emergent p -wave features a gap in the direction of the unpopulated SDW-domain, which is compatible with the $d_{x^2-y^2}$ -gap symmetry (see Fig. 2.5b and c) and enables the population of the SDW-domain perpendicular to its maximal extent.

A lowest linear-order coupling term between magnetism and superconductivity predicts a spatially modulated triplet component, such that momentum is conserved [221, 222]. It is currently debated whether the Q-phase features a spin-triplet PDW with coexistent d -wave or FFLO-superconductivity. The former theory assumes a spatially-modulated p -wave as the primary order parameter of the Q-phase that induces SDW order [221]. Here, the switching of the domain population may be driven by the anisotropic spin susceptibility of the spin-triplet component [88]. In an alternative scenario a field-induced FFLO-phase emerges as a primary order parameter [222]. Here, SDW order arises from pair breaking effects and triggers the emergence of the p -wave component. The change of the SDW modulation direction is driven

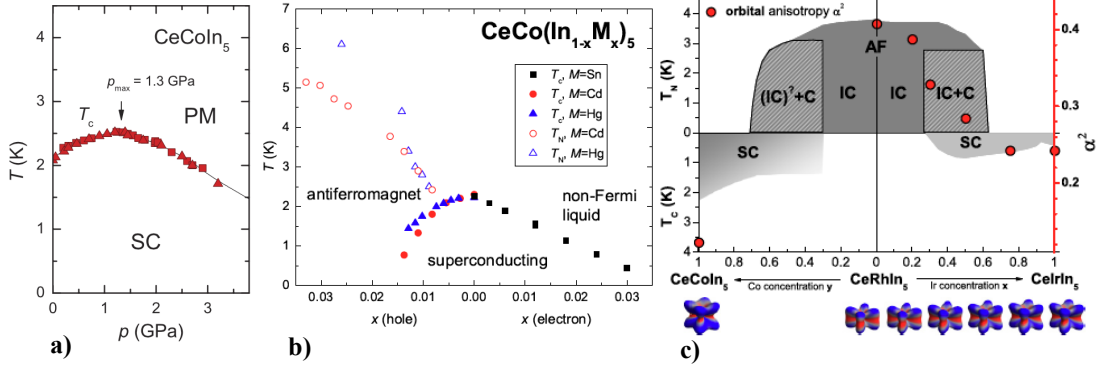


FIGURE 4.6: Pressure and Doping Dependence of CeCoIn₅. a) pT -phase diagram of CeCoIn₅. b) xT -phase diagram of CeCo(In_{1-x}M_x)₅ with $M = \text{Sn}, \text{Cd}$ and Hg . c) yT -phase diagram of CeM_{1-y}N_yIn₅ with $M, N = \text{Co}, \text{Rh}$ and Ir with orbital anisotropy of crystal field $4f$ -wave function. Taken from [196, 225, 229].

by the spatially-modulated d -wave that is sensitive to the magnetic field direction [158].

Irrespective of the different phenomenological theories, the maximal p -wave gap estimated by thermal conductivity is about 20% of the one of the d -wave amplitude [219]. One possible avenue to gain further insight in the microscopic nature of the Q-phase is the application of external parameters auxiliary to magnetic field.

4.4 PRESSURIZED AND SUBSTITUTED CECOIN₅

The ground state properties of CeCoIn₅ have been tuned previously by hydrostatic pressure and chemical substitution [26, 27, 196, 225–243]. The former parameter triggers an increase of the superconducting transition temperature up to $T_c \approx 2.5$ K at $p_{\max} = 1.3$ GPa [225, 226]. Larger pressures yield a decreasing T_c that is suppressed at $p_c \approx 4$ GPa (see Fig. 4.6a). Isotropic pressure reduces the unit cell volume of the material in a monotonic way but has an anomalous impact on the tetragonal a - and c -axis [226]. An increasing c/a ratio is observed for increasing pressures that may saturate for $p_{\max} < p < p_c$ and decreases for further increments. Thus, the discrepancy of the in- and out-of-plane wave-function overlap between the Ce $4f$ -orbital and the two inequivalent In $5p$ -orbitals possibly explains the behavior of $T_c(p)$ in CeCoIn₅ [196, 226]. Thermal heat capacity and magnetization studies under pressure and at high magnetic fields show that the Q-phase is stable up to at least $p = 1.4$ GPa [227, 228]. Hitherto, no neutron diffraction results of the Q-phase were reported under pressure, preeminently because of the technical challenges of such an experiment.

Chemical substitution is a complex way of tuning the ground state properties of CeCoIn₅, because it acts on a multitude of physical properties. This includes the tuning of the crystal-field wave function, changes in the in- and/or out-of-plane hybridization or the incorporation

of impurities, Kondo holes, mixed valence elements or localized moments.

Several experiments were carried out on the series CeCo(In_{1-x}M_x)₅ with $M = \text{Sn, Cd, Hg}$ and Zn [26, 229–235]. Sn features one extra electron when compared to In and in contrast, Cd, Hg and Zn act as hole dopants. Extended x-ray absorption fine structure measurements have shown that Sn, Cd, and Hg mainly substitute the In atom in the tetragonal basal plane and have, thus, a direct effect on the in-plane hybridization [229, 230]. It is expected that the unequal distribution of impurity atoms in the crystalline structure also affects the crystal-field ground state wave function. The interpenetrating xT -phase diagram is shown in Fig. 4.6b and reveals an interplay between superconductivity and magnetism. While the superconducting transition temperature and the upper critical field decrease for Sn substitution, T_c and H_{c2} display an anti-theoretical trend for small Cd and Hg concentrations [26]. No sign of the Q-phase has been found above 0.05% Hg concentration on the In site. In contrast, hole-doping concentrations of about 1% feature a microscopic coexistence of superconductivity and magnetism with a suppressed superconducting phase at larger concentrations [229, 231, 233]. Magnetic order appears at the commensurate wave-vector $\mathbf{Q}_{AF} = (1/2, 1/2, 1/2)$ and may origin from impurity-induced magnetic islands [232]. The antiferromagnetic transition temperature rises for increasing x and the differences between Cd and Hg substitution may be attributed to the auxiliary c -axis distortion that is found in Hg doped CeCoIn₅ [229, 230].

The substitution of Rh for Co drives the system from a d -wave superconductor into the antiferromagnetic ground state of CeRhIn₅ that features a small Fermi surface [196]. The magnetic order in CeRhIn₅ is incommensurate, $\mathbf{Q}_S = (1/2, 1/2, 0.297)$, and reveals a spiral structure along the tetragonal c -axis with an ordered moment $\mu = 0.54\mu_B$ [244, 245]. The yT -phase diagram of CeCo_yRh_{1-y}In₅ is depicted in Fig. 4.6c. Small Rh concentrations continuously decrease the superconducting transition temperature until magnetic order emerges at $y = 0.75$ that coexists with superconductivity for $0.3 > y > 0.75$ [196]. Superconductivity collapses in a first-order transition at a Rh concentration of 70% and the magnetic structure is incommensurate on the Rh dominated side of the phase diagram. In the phase space where superconductivity coexists with magnetism a combination of commensurate and incommensurate magnetic order has been observed [246, 247]. A spiral antiferromagnetic state is, however, incompatible with d -wave superconductivity and it is currently debated whether the phase originates from sample stoichiometry uncertainties [248–250].

Recent x-ray absorption spectroscopy results have shown that the substitution on the Co site tunes the crystal-field environment and affects the spatial distribution of the $4f$ Ce ground state wave-function [196]. While the out-of-plane anisotropy is prolate in CeCoIn₅, the wave-function features an oblate shape in CeRhIn₅ (see Fig. 4.6c). Upon Rh doping in CeCoIn₅ the $4f$ -cerium orbital is squeezed into the tetragonal CeIn₃ plane, decreasing the hybridization with the out-of-plane In $5p$ -orbitals. The suppression of itinerant f -electrons reduces the size of the Fermi surface and drives the system away from the superconducting ground state and into a magnetically ordered phase. It is noted that the hole doping effect on the Co-site has been investigated in CeCo_{1-x}Ru_xIn₅ for substitutions $x < 0.5$ [236]. It leads to a suppression of superconductivity without an emergent magnetic phase.

Chemical substitution on the Ce-site of CeCoIn₅ has the advantage that it affects directly the Kondo coupling strength between the $4f$ -electrons and the conduction band. This should allow a much more controlled tuning of the correlated ground state when compared to substitutions on the Co- or In-site or the application of hydrostatic pressure. The most prominent

studies were carried out on Yb, La and Nd doped CeCoIn₅ that represent the substitution with a mixed-valence element, a Kondo hole and a localized magnetic moment, respectively [27, 237–243].

Yb is generally considered as the hole analog of Ce, because Ce³⁺ features one electron in the 4*f* shell, while Yb³⁺ has a single hole. However, the hole occupancy of Yb in Ce_{1-x}Yb_xCoIn₅ is strongly intermediate (Yb^{2.3+}) and leads to a broad crossover towards a metallic ground state of mixed-valence that is accompanied with a linearly decreasing T_c as x is increased [239–241]. Temperature dependent studies on the London penetration depth have suggested that the $d_{x^2-y^2}$ order parameter becomes fully gapped for $x > 0.2$ [237]. This conclusion has been questioned by recent thermal conductivity measurements that provide evidence for a robust superconducting d -wave gap [238].

The substitution of La for Ce in CeCoIn₅ is less complex in this respect, because La has an empty 4*f*-shell when compared to the single occupied state of Ce. Ce_{1-x}La_xCoIn₅ reveals a decreasing superconducting transition temperature with increasing x that clearly maintains the d -wave order parameter [237, 243]. The incorporated Kondo hole yields pair breaking effects that give rise to conduction electrons which are excluded from the superconducting condensate [242]. No interplay with magnetic order is found in Ce_{1-x}La_xCoIn₅ and no Q-phase has been reported in this series yet.

The substitution of the itinerant Ce³⁺ with a localized magnetic moment of the same valence should shift the hybridized 4*f*-band below the Fermi level without adding the complexity of a mixed-valence element. Such a doping would reduce the Kondo coupling with the conduction electrons, while leaving, in a first approximation, invariant the relative overlap with the in- and out-of-plane In 5*p*-orbitals. This increases the chance of observing a stable Q-phase for moderate doping concentrations and the localized moment eventually induces magnetic order that coexists with superconductivity. The substitution of Nd³⁺ for Ce in CeCoIn₅ unifies these requirements.

Chapter 5

Intertwined Degrees of Freedom in the Series $\text{Nd}_{1-x}\text{Ce}_x\text{CoIn}_5$

Systematic studies on $\text{Nd}_{1-x}\text{Ce}_x\text{CoIn}_5$ were carried out first in 2008 [27]. The series features a rich xT -phase diagram with different electronic ground states, including magnetic order for $x \leq 0.95$, superconductivity for $x \geq 0.83$ and HF properties for $x \geq 0.5$ (c.f. Fig. 5.1a). Magnetism coexists with superconductivity for $0.83 \leq x \leq 0.95$ that preserves, most likely, the $d_{x^2-y^2}$ gap symmetry [27, 237]. A gradual suppression of the heat capacity jump at T_c , $\Delta C/C(T_c)$, has been observed with increasing Nd concentration and provides evidence that the dopant weakens the superconducting pairing strength. The incorporation of Nd impurities, thus, acts as random disorder in the material and reduces the hybridization with the conduction band that yields a coherent Kondo lattice around $x \approx 0.5$ [27, 28]. Localized moment magnetism arises within a small Fermi surface ($x < 0.5$) and is expected to be itinerant for large Ce concentrations. It is noted that a detailed analysis of $\Delta C/C(T_c)$ showed that the effect of chemical pressure is less important in the series when compared to the tuning of the Kondo coupling [27].

The nature of magnetic order in $\text{Nd}_{1-x}\text{Ce}_x\text{CoIn}_5$ is currently unknown, but crucial to understand how magnetic order, superconductivity and HF properties are intertwined. Hitherto, only $\text{Nd}_{0.05}\text{Ce}_{0.95}\text{CoIn}_5$ has been investigated microscopically using neutron diffraction [251]. It features a superconducting phase with $T_c = 1.8$ K that coexists with magnetism below $T_N = 0.8$ K [27, 251]. Magnetic order develops at a wave-vector $\mathbf{Q}_{ICM} = (q, \pm q, 0.5)$ with $q \approx 0.45$ at zero field, which is similar to the one of the Q-phase in CeCoIn_5 (see Fig. 5.1b) [23, 251]. An ordered moment between $0.1 - 0.15\mu_B$ is expected, but insight in its orientation is lacking [251]. Moreover, the nature of this SDW and its relation to the Q-phase of CeCoIn_5 is an open question that is addressed in this thesis.

5.1 CHEMICAL SYNTHESIS AND SAMPLE QUALITY

Single crystalline CeCoIn_5 samples were synthesized using an In self-flux with atomic parts of 3% Ce, 3% Co and 94% In [17]. The high purity starting elements were placed in an alumina crucible and heated to 1150 °C using an evacuated and sealed quartz tube. A uniform distribution of the liquid elements was ensured by a 30 min motorized rotation of the quartz tube at the maximal temperature. After rapidly (100 °C/h) decreasing the temperature to $T_i^1 = 750$ °C,

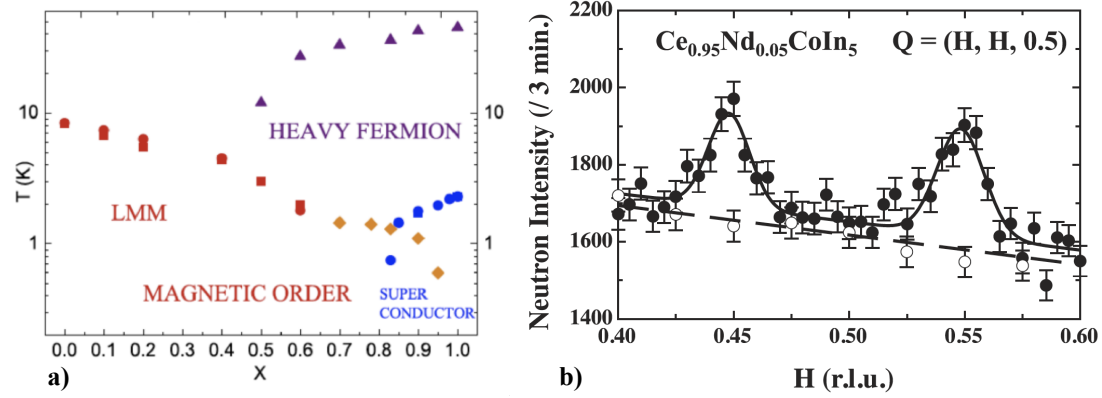


FIGURE 5.1: xT -Phase Diagram of $\text{Nd}_{1-x}\text{Ce}_x\text{CoIn}_5$. **a)** Phase diagram of $\text{Nd}_{1-x}\text{Ce}_x\text{CoIn}_5$ with HF properties for $x \geq 0.5$, itinerant magnetism and localized moment magnetism (LMM) for $x \leq 0.95$ and superconductivity for $0.83 \leq x \leq 1$. **b)** Magnetic intensity along $Q = (H, H, 0.5)$ in $\text{Nd}_{0.05}\text{Ce}_{0.95}\text{CoIn}_5$ measured for temperatures above and below $T_N = 0.8$ K. Taken from [27, 251].

the liquid was cooled to $T_f^1 = 450$ °C at a rate of 3 °C/h. The major fraction of excess flux was separated from the crystals by means of centrifugation, where quartz wool was used as a filter. The remaining flux on the crystal surface was removed via hydrochloric acid (HCl). The resulting single crystals had typical dimensions of $2 \times 2 \times 0.1$ mm³ and revealed a RRR ≈ 5 (see Fig. 5.3a), comparable to the first experimental realizations of the compound [17]. The growth of NdCoIn_5 was found to be optimized by tuning $T_i^0 = 800$ °C and $T_f^0 = 550$ °C, which led to $T_{i,f}^x = T_{i,f}^0 - (T_{i,f}^0 - T_{i,f}^1)x$ for $\text{Nd}_{1-x}\text{Ce}_x\text{CoIn}_5$.

The experimental realizations presented in this thesis were synthesized in a collaboration between the Paul Scherrer Institut, Villigen Switzerland ($x = 0, 0.2, 0.4, 0.6, 0.75$ and 1) and the Commissariat à l’Energie Atomique et aux Energies Alternatives, Grenoble France ($x = 0.83, 0.95$). The sample quality of $x = 0, 0.2, 0.4, 0.6$, and 1 has been investigated by high-resolution X-ray powder diffraction at the Material Science (MS-X04SA) beamline of the Swiss Light Source at the Paul Scherrer Institut. Ground single crystals were filled in quartz capillaries of diameter $d = 0.1$ mm, which were exposed to a photon wavelength $\lambda = 0.56491$ Å. The diffracted photons were collected by a Mythen-II detector. All samples were measured at room temperature and the results are displayed in Fig. 5.2a.

The comparison of the diffraction patterns provides evidence that all samples crystallized in an identical space group symmetry and were refined in $P4/mmm$ using the FullProf suite [169]. The structural analysis shows that all compositions were synthesized in a very pure form with residual impurity contributions of $f < 1$ -2%, which were attributed to contents in the remaining flux. We find structural diffraction peaks that shift monotonically to larger diffraction angles, 2θ , as the Ce content is increased, while a uniform peak width is observed that is independent on x . The doping dependent evolution of the crystallographic a - and c -axis is shown in Fig.

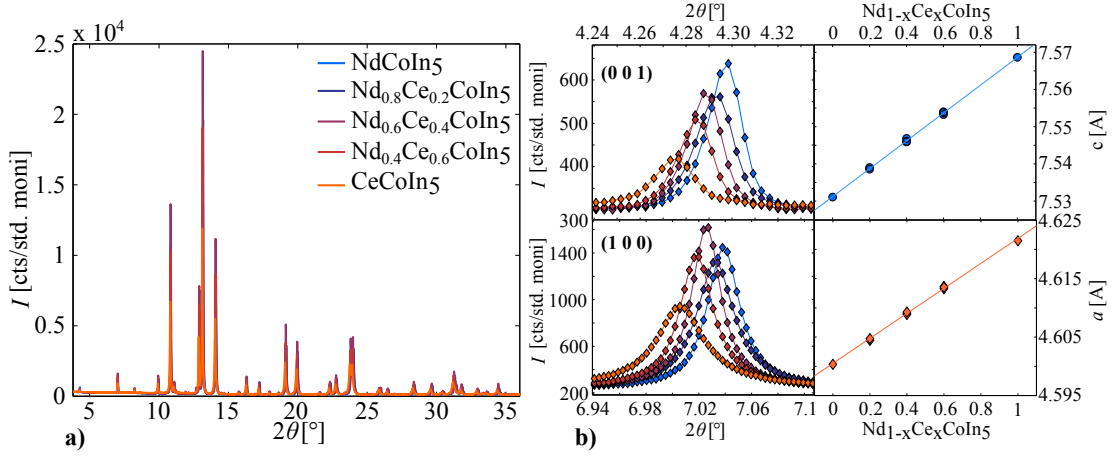


FIGURE 5.2: X-ray Powder Diffraction of $\text{Nd}_{1-x}\text{Ce}_x\text{CoIn}_5$. a) Diffracted photon intensity of $\text{Nd}_{1-x}\text{Ce}_x\text{CoIn}_5$ for $x = 0, 0.2, 0.4, 0.6$ and 1 as a function of the scattering angle, 2θ , at room temperature. b) The linear shift of the lattice parameters a and c reveals a homogeneous substitution of Ce for Nd.

5.2b and reveals a linear dependence in agreement with earlier reports [27]. These results provide evidence that Ce substitutes Nd uniformly in $\text{Nd}_{1-x}\text{Ce}_x\text{CoIn}_5$ without supplementary inter-grown structural phases. It is noted that no differences among batches with the same nominal Ce concentration, x_{nom} , were observed.

The actual Ce content in the samples was determined via high-resolution neutron powder diffraction on the instrument HRPT at SINQ. About $m = 3$ g of ground single crystals per composition were loaded in vanadium double-walled cans with inner diameter $d_{inner} = 8$ mm and outer diameter $d_{outer} = 9.2$ mm. The four sample holders were installed on the automatic sample changer of HRPT and inserted in an orange cryostat with a base temperature of $T = 1.8$ K. A neutron wavelength of $\lambda = 1.886$ Å was employed.

Neutron powder diffraction results on NdCoIn_5 were measured at $T = 15$ and 1.8 K and are shown in Fig. 5.4a. The diffraction pattern at $T = 15$ K was refined within two contributing phases accounting for the supplementary vanadium Bragg peaks that provide a fraction of about $f \approx 5\%$ to the total integrated intensity (agreement factor $R_f = 10\%$). The additional magnetic phase at $T = 1.8$ K is discussed in chapter 5.5. The refined Ce content ($R_f = 5\%$) of the substituted samples with nominal concentrations $x_{nom} = 0.2, 0.4, 0.6$ is depicted in Fig. 5.4b (see Tab. 3.2.1 for the difference in σ_{coh}^{Nd} and σ_{coh}^{Ce}). While we observe a maximal discrepancy $\Delta x = x_{obs} - x_{nom} = -4(2)\%$ for $x_{nom} = 0.2$, $x_{obs} = 0.40(2)$ and $0.61(2)$ is found for $x_{nom} = 0.4$ and 0.6 , respectively.

$\text{Nd}_{0.05}\text{Ce}_{0.95}\text{CoIn}_5$ single crystals feature $\text{RRR} \approx 3.6$ (see Fig. 5.7a) with a Nd uncertainty concentration of about 1% that was determined by in-beam neutron activation analysis at the Heinz Maier-Leibnitz neutron source FRM-II, Munich Germany. The technique enables

a non-destructive chemical analysis, in which samples are activated by a white neutron beam and analyzed by their time dependent gamma radiation spectrum. The averaged stoichiometric composition is determined via the different radioactive half-life times of the chemical elements in the crystal [252]. The homogeneity of the chemical composition was verified by energy dispersive X-ray spectrometry and photo-emission electron microscopy on the SIM beamline of the Swiss Light Source, Paul Scherrer Institut [251]. High spatial resolution X-ray absorption maps were measured on and off the Nd M_5 , Ce M_5 , Co L_3 and In M_5 absorption edges. The elemental contrast of these images provides evidence for a uniform Nd distribution in the sample. The single crystal neutron scattering results presented here were carried on the same single crystal that is reported in Ref. [251] with mass $m = 64$ and dimensions $7 \times 4 \times 0.3 \text{ mm}^3$.

Single crystal diffraction on $\text{Nd}_{1-x}\text{Ce}_x\text{CoIn}_5$ with $x_{nom} = 0.83$ and 0.75 was obtained from experimental realizations with masses $m = 20$ and 14 mg and $3 \times 2.7 \times 0.15$ and $3.5 \times 2.1 \times 0.3 \text{ mm}^3$, respectively. The quality of these samples was checked with X-ray Laue diffraction.

5.2 THE MAGNETIC PHASE DIAGRAM OF $\text{Nd}_{1-x}\text{Ce}_x\text{CoIn}_5$ AT ZERO FIELD

Localized moment magnetism is expected to compete with the HF ground state in $\text{Nd}_{1-x}\text{Ce}_x\text{CoIn}_5$ [27]. Although magnetic order is found for $x \leq 0.95$ only the magnetic wave-vector of 5% Nd doped CeCoIn_5 is known at zero field [27, 251]. We performed a systematic study of the magnetic ground state in the series, which provides detailed insight in the interplay between the rivalry energy scales.

5.2.1 Experimental Details.

The xT -phase diagram of $\text{Nd}_{1-x}\text{Ce}_x\text{CoIn}_5$ was investigated by means of electrical resistivity, magnetization and neutron diffraction. Macroscopic transport measurements that were performed by our group at PSI were recorded in a Quantum Design PPMS or in cryogenic magnets, where a four-probe setup was used. We found the Kondo coherence temperatures $T_{coh} = 46, 48, 30$ and 26 K for $x = 1, 0.95, 0.83$ and 0.75 and $T_c = 2.3, 1.8$ and 1.17 for $x = 1, 0.95$ and 0.83 , respectively (see Fig. 5.3a and 5.7a). Magnetization data on $x = 0, 0.16, 0.4$ and 0.61 revealed the Néel temperatures $T_N = 8.2, 6.3, 4.4$ and 2.3 (see Fig. 5.3b). The values fit in the initial phase diagram reported by Hu *et. al.* [27].

Neutron diffraction experiments were carried out on HRPT for $x = 0, 0.16, 0.4$ and 0.61 as well as on the single crystal diffractometers Zebra at SINQ for $x = 0.75$ and on D10 at the Institut Laue-Langevin (ILL), Grenoble France for $x = 0.95$, respectively. $\text{Nd}_{0.17}\text{Ce}_{0.83}\text{CoIn}_5$ was investigated on the triple-axis spectrometer IN12 at the ILL. The experiment on D10 was conducted with a neutron wavelength $\lambda = 2.36 \text{ \AA}$ using a four-circle setup with a dilution insert. An orange cryostat with ^3He insert was employed on IN12 and a Variox cryostat with dilution insert was used on Zebra ($\lambda = 1.177 \text{ \AA}$). On IN12 the sample was aligned in the plane perpendicular to $[1 -1 0]$ and perpendicular to $[0 1 0]$ for the experiment on Zebra. The latter orientation enabled a search for magnetic reflections along $(h, 0, l)$ and (h, h, l) by means of the lifting-arm detector of the instrument. On IN12 clean wavelengths of $\lambda = 3.307$ and 4.83 \AA were derived from a velocity selector and a double-focussing pyrolytic graphite monochromator. The instrument was used in a W -configuration (as depicted in Fig. 3.2b) with collimated neutrons ($\alpha = 80^\circ$) in front of the sample.

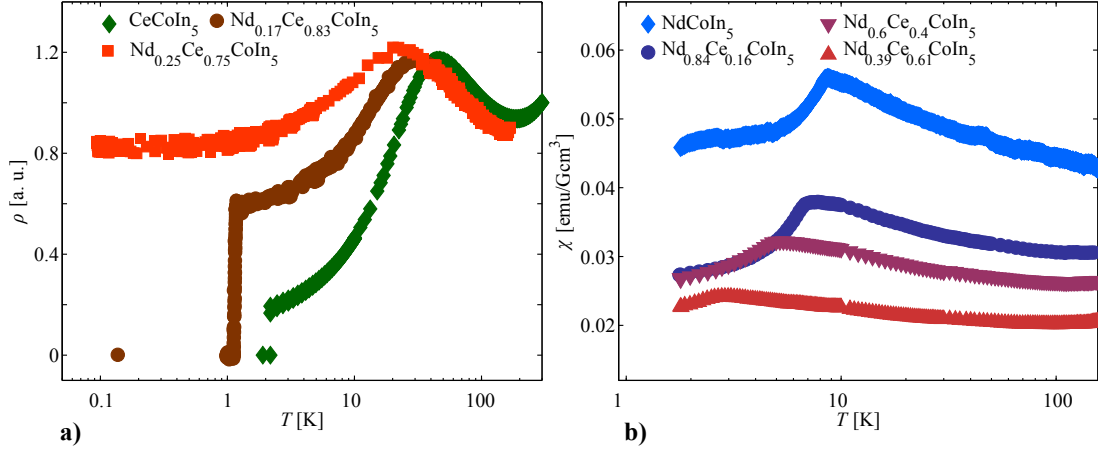


FIGURE 5.3: Macroscopic Results of $\text{Nd}_{1-x}\text{Ce}_x\text{CoIn}_5$. a) Renormalized electrical resistivity data on CeCoIn_5 , $\text{Nd}_{0.17}\text{Ce}_{0.83}\text{CoIn}_5$ and $\text{Nd}_{0.25}\text{Ce}_{0.75}\text{CoIn}_5$. b) Magnetic susceptibility of NdCoIn_5 , $\text{Nd}_{0.84}\text{Ce}_{0.16}\text{CoIn}_5$, $\text{Nd}_{0.6}\text{Ce}_{0.4}\text{CoIn}_5$ and $\text{Nd}_{0.39}\text{Ce}_{0.61}\text{CoIn}_5$ using an applied field of $\mu_0 H = 100$ mT.

5.2.2 Ising-like Structure in Nd dominated $\text{Nd}_{1-x}\text{Ce}_x\text{CoIn}_5$.

Powder neutron diffraction results on NdCoIn_5 are shown in Fig. 5.4a and are representative for $\text{Nd}_{1-x}\text{Ce}_x\text{CoIn}_5$ with $x = 0, 0.16, 0.4$ and 0.61 . We observe resolution limited magnetic Bragg peaks at $T = 1.8$ K $< T_N$. They are consistent with the commensurate (CM) propagation vectors $\mathbf{Q}_{CM} = (1/2, 0, 1/2)$ and $(0, 1/2, 1/2)$, doubling the unit cell along the tetragonal a - and c -axis. The representational analysis was performed with the program Basireps of the FullProf suite (see chapter 3.3 for the definition of parameters) [169]. The wave-vectors remain invariant under symmetry operations of the little group $G_{Q_{CM}}$ in $P4/mmm$ that consists of the elements $g_{1-8} = \{1|000\}$ (identity), $\{2_{001}|000\}$ (twofold rotation around $[0\ 0\ 1]$), $\{2_{010}|000\}$, $\{2_{100}|000\}$, $\{\bar{1}|000\}$ (inversion), $\{m_{001}|000\}$ (mirror operation on the plane perpendicular to $[0\ 0\ 1]$), $\{m_{010}|000\}$ and $\{m_{100}|000\}$.

The general moment vector, $\mathbf{M} = (M_x, M_y, M_z)$, at the crystallographic Nd/Ce site, $(0, 0, 0)$, transforms under $G_{Q_{CM}}$ according to Tab. 5.1. The magnetic ion position is robust under g_{1-8} ($\chi_P = 1$) and the natural representation $\Gamma_M^{Q_{CM}}$ with character $\chi_M^{Q_{CM}} = \chi_P \chi_A$ is obtained with Eq. 3.18. It can be decomposed in a linear combination of the irreducible representations $\Gamma_3^{Q_{CM}}$, $\Gamma_5^{Q_{CM}}$ and $\Gamma_7^{Q_{CM}}$ via Eq. 3.19 (c.f. Tab. 5.1). The projection formula in Eq. 3.20 yields the three basis vectors $\mathbf{S}_3^{Q_{CM}} = (0, 0, 1)$, $\mathbf{S}_5^{Q_{CM}} = (0, 1, 0)$ and $\mathbf{S}_7^{Q_{CM}} = (1, 0, 0)$ for $\Gamma_3^{Q_{CM}}$, $\Gamma_5^{Q_{CM}}$ and $\Gamma_7^{Q_{CM}}$, respectively.

The best refinement of the absorption and Lorentz corrected integrated intensity is found with a magnetic moment orientation along the c -axis ($\mu(\mathbf{R}) = \mu_p \mathbf{S}_3^{Q_{CM}} \exp[i\mathbf{Q}_{CM}\mathbf{R}] + c.c$) and two additional phases that account for the nuclear Bragg peaks originating from $\text{Nd}_{1-x}\text{Ce}_x\text{CoIn}_5$

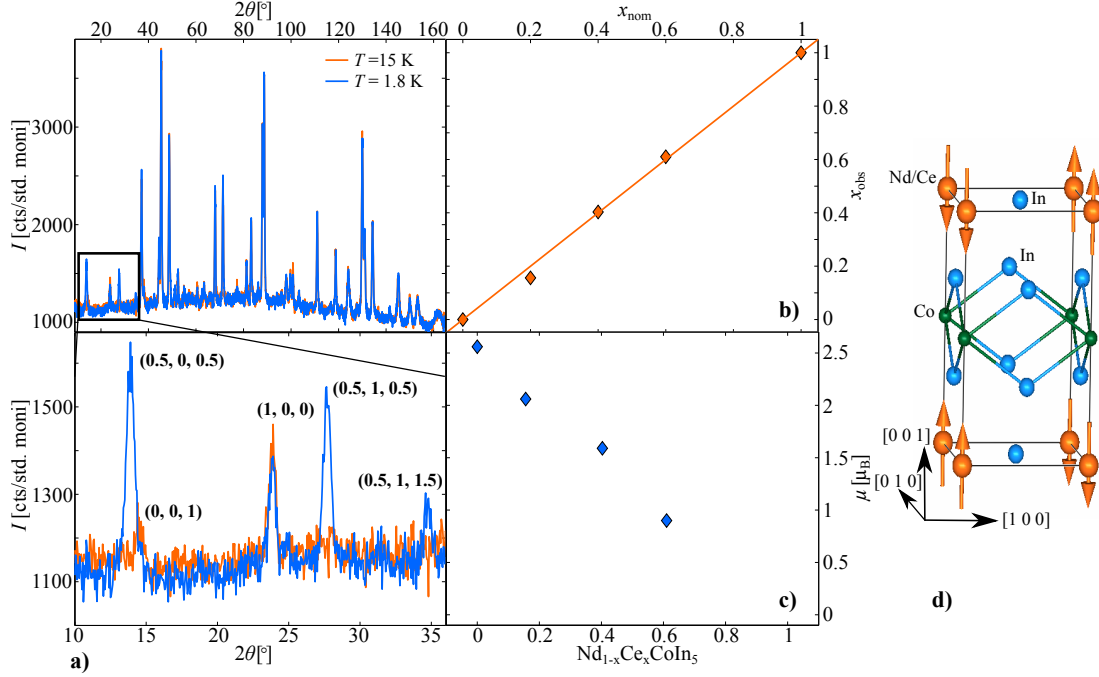


FIGURE 5.4: Neutron Powder Diffraction on $\text{Nd}_{1-x}\text{Ce}_x\text{CoIn}_5$. **a)** Diffracted neutron intensity of NdCoIn_5 as a function of the scattering angle, 2θ , at $T = 15$ and 1.8 K. **b)** Refined Ce content, x_{obs} , against the nominal concentration, x_{nom} . **c)** Doping dependence of the magnetic moment for $x_{obs} = 0, 0.16, 0.4, 0.61$ measured at $T = 1.8$ K. **d)** The magnetic structure reveals an antiferromagnetic alignment with moment orientation along the tetragonal axis and wave-vector $\mathbf{Q}_{CM} = (1/2, 0, 1/2)$.

and the vanadium sample holder*. It reveals an ordered magnetic moment $\mu = 2.56(3)\mu_B$ in NdCoIn_5 with a respective agreement factor $R_f = 15\%$. The irreducible basis vectors, \mathbf{S}_5 and \mathbf{S}_7 , yield $R_f > 35\%$. Similar results are obtained for $\text{Nd}_{0.84}\text{Ce}_{0.16}\text{CoIn}_5$, $\text{Nd}_{0.6}\text{Ce}_{0.4}\text{CoIn}_5$ and $\text{Nd}_{0.39}\text{Ce}_{0.61}\text{CoIn}_5$ with a moment size that is decreasing with increasing Ce content (see Fig. 5.4c). The magnetic structure is shown in Fig. 5.4d for the $(1/2, 0, 1/2)$ -domain and shows an antiferromagnetic modulation along $(1, 0, 0)$ and $(0, 0, 1)$. The magnetic structure is identical to the isostructural compounds RRhIn_5 with $R = \text{Nd, Tb, Dy}$ and Ho as well as RCoGa_5 with $R = \text{Tb}$ and Ho [253].

5.2.3 Spin-Density Wave in Ce dominated $\text{Nd}_{1-x}\text{Ce}_x\text{CoIn}_5$.

Single crystal neutron diffraction on samples with large Ce concentration, $\text{Nd}_{1-x}\text{Ce}_x\text{CoIn}_5$ with $x \geq 0.75$, reveals an incommensurate wave-vector $\mathbf{Q}_{ICM} = (q, \pm q, 0.5)$ with $q \approx 0.44$. Neutron intensity along the reciprocal $(q, q, 1/2)$ and $(0.44, 0.44, l)$ directions is depicted in

*In substituted samples the occupation of the magnetic sites was adjusted such that the magnetic form factor reflects the distribution of Nd/Ce atoms in the sample.

	$\{1 000\}$	$\{2_{001} 000\}$	$\{2_{010} 000\}$	$\{2_{100} 000\}$	$\{\bar{1} 000\}$	$\{m_{001} 000\}$	$\{m_{010} 000\}$	$\{m_{100} 000\}$
M_x	M_x	$-M_x$	$-M_x$	M_x	M_x	$-M_x$	$-M_x$	M_x
M_y	M_y	M_y	M_y	$-M_y$	M_y	$-M_y$	M_y	$-M_y$
M_z	M_z	M_z	$-M_z$	$-M_z$	M_z	M_z	$-M_z$	$-M_z$
χ_P	1	1	1	1	1	1	1	1
χ_A	3	-1	-1	-1	3	-1	-1	-1
$\chi_M^{Q_{CM}}$	3	-1	-1	-1	3	-1	-1	-1
$\chi_1^{Q_{CM}}$	1	1	1	1	1	1	1	1
$\chi_2^{Q_{CM}}$	1	1	1	1	-1	-1	-1	-1
$\chi_3^{Q_{CM}}$	1	1	-1	-1	1	1	-1	-1
$\chi_4^{Q_{CM}}$	1	1	-1	-1	-1	-1	1	1
$\chi_5^{Q_{CM}}$	1	-1	1	-1	1	-1	1	-1
$\chi_6^{Q_{CM}}$	1	-1	1	-1	-1	1	-1	1
$\chi_7^{Q_{CM}}$	1	-1	-1	1	1	-1	-1	1
$\chi_8^{Q_{CM}}$	1	-1	-1	1	1	1	1	-1

TABLE 5.1: Representational Analysis of $\text{Nd}_{1-x}\text{Ce}_x\text{CoIn}_5$ with $Q_{CM} = (1/2, 0, 1/2)$. Transformation of the general moment vector, $\mathbf{M} = (M_x, M_y, M_z)$ at the magnetic site $(0, 0, 0)$ under the little group $G_{Q_{CM}}$ and character table of the general and irreducible representations of $P4/mmm$ with $Q_{CM} = (1/2, 0, 1/2)$.

Fig. 5.5a and b for $\text{Nd}_{0.17}\text{Ce}_{0.83}\text{CoIn}_5$ at $T = 0.4, 1.2$ and 1.8 K and along $(q, q-1, 1/2)$ at $T = 0.05$ K for $\text{Nd}_{0.25}\text{Ce}_{0.75}\text{CoIn}_5$ in Fig. 5.5c. Representative data for $\text{Nd}_{0.05}\text{Ce}_{0.95}\text{CoIn}_5$ are shown in Fig. 5.1b. A lower bound of the magnetic correlation lengths, ξ_a and ξ_c , is obtained from the resolution-limited magnetic Bragg peak width. The best fits to the data show $\xi_a > 150, 138, 45$ Å for $x = 0.95, 0.83$ and 0.75 and $\xi_c > 200$ and 181 Å for $x = 0.95$ and 0.83 , respectively. The low value of ξ_a in $\text{Nd}_{0.25}\text{Ce}_{0.75}\text{CoIn}_5$ results from the instrumental setup that was used on Zebra. Here, a scan along $(q, q-1, 1/2)$ mainly involved an out-of-plane movement of the detector that is known to have a poor resolution.

The wave-vector differs from the commensurate ordering vector observed on the Nd dominated side of the phase diagram, $x \leq 0.61$, and also from the one found in $\text{CeCoIn}(\text{In}_{1-x}\text{M}_x)_5$ with $M = \text{Cd}, \text{Hg}$ and Zn and $\text{CeCo}_y\text{Rh}_{1-y}\text{In}_5$ [232, 246, 247]. In contrast, Q_{ICM} is similar to the wave-vector that occurs in the Q-phase of CeCoIn_5 [23, 88, 145].

The magnetic wave-vector remains invariant under the symmetry operations of the little group $G_{Q_{ICM}}$ within $P4/mmm$ that consists of the four symmetry operations $g_{1-4} = \{1|000\}, \{2_{110}|000\}, \{m_{001}|000\}$ and $\{m_{1\bar{1}0}|000\}^\dagger$. The general moment vector, $\mathbf{M} = (M_x, M_y, M_z)$, at $(0, 0, 0)$ transforms under $G_{Q_{ICM}}$ as shown in Tab. 5.2. The natural representation can be reduced to $\Gamma_M^{Q_{ICM}} = \Gamma_2^{Q_{ICM}} + \Gamma_3^{Q_{ICM}} + \Gamma_4^{Q_{ICM}}$ that feature the three Eigenvectors $\mathbf{S}_2^{Q_{ICM}} = \sqrt{2}/2(1, 1, 0)$, $\mathbf{S}_3^{Q_{ICM}} = (0, 0, 1)$ and $\mathbf{S}_4^{Q_{ICM}} = \sqrt{2}/2(1, -1, 0)$.

The magnetic refinements were performed on seven independent magnetic Bragg reflections of $\text{Nd}_{0.17}\text{Ce}_{0.83}\text{CoIn}_5$ and provide evidence for a magnetic orientation along the tetragonal

[†] $\{m_{110}|000\}$ for the $(q, -q, 0.5)$ -domain.

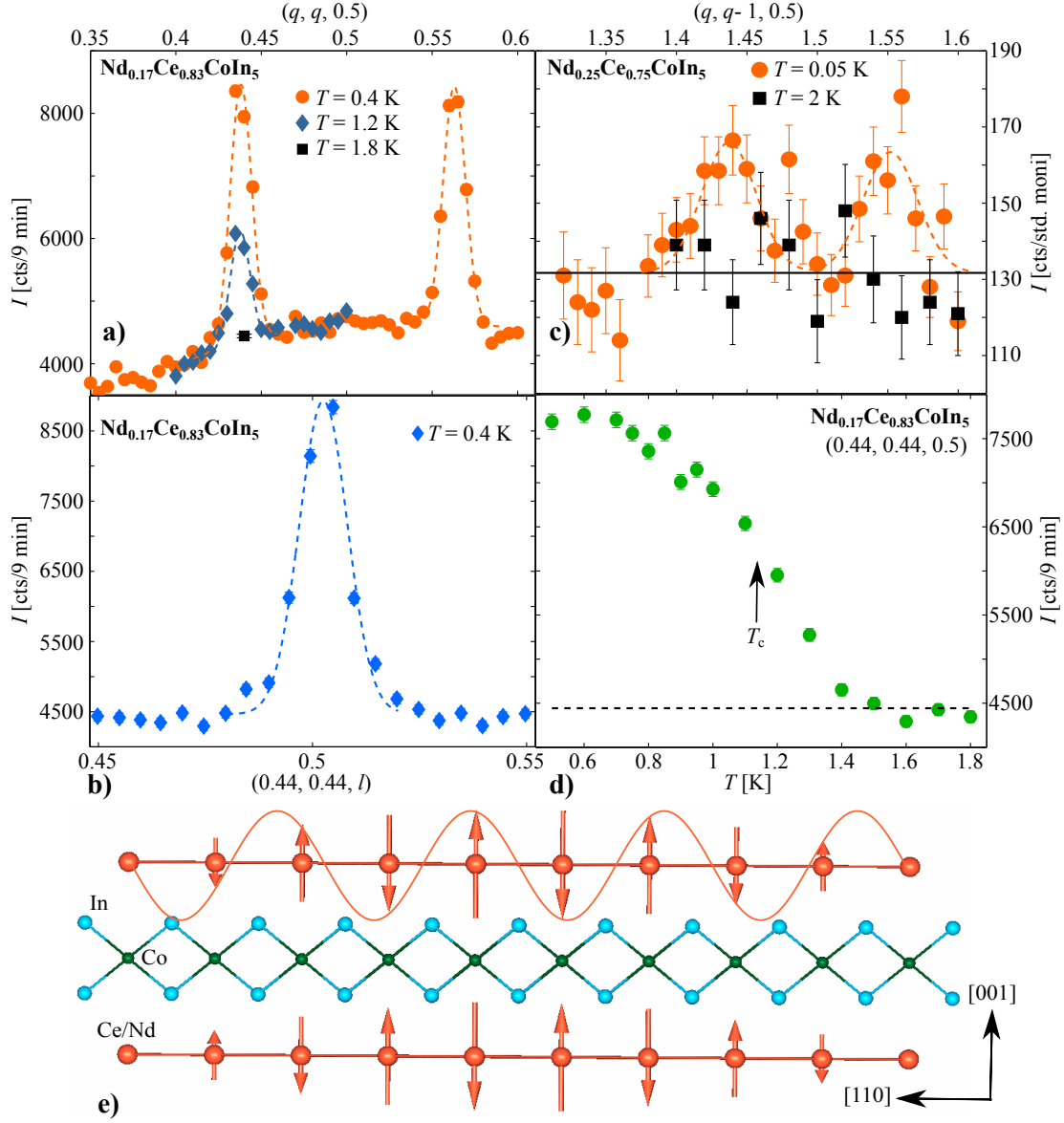


FIGURE 5.5: Single Crystal Neutron Diffraction on $\text{Nd}_{1-x}\text{Ce}_x\text{CoIn}_5$. Diffracted neutron intensity of $\text{Nd}_{0.17}\text{Ce}_{0.83}\text{CoIn}_5$ along $(q, q, 0.5)$ in **a)** and $(0.44, 0.44, l)$ in **b)**. **c)** Diffracted neutron intensity of $\text{Nd}_{0.25}\text{Ce}_{0.75}\text{CoIn}_5$ along $(q, q-1, 0.5)$ **d)** Temperature dependent neutron intensity of $\text{Nd}_{0.17}\text{Ce}_{0.83}\text{CoIn}_5$ at $(0.44, 0.44, 1/2)$. **e)** The magnetic structure of $\text{Nd}_{0.95}\text{Ce}_{0.05}\text{CoIn}_5$, $\text{Nd}_{0.17}\text{Ce}_{0.83}\text{CoIn}_5$ and $\text{Nd}_{0.25}\text{Ce}_{0.75}\text{CoIn}_5$ is amplitude modulated with a moment orientation along the c -axis and $Q_{ICM} = (q, \pm q, 0.5)$ with $q \approx 0.44$. Here the $(q, q, 0.5)$ domain is shown (taken from [28]).

	$\{1 000\}$	$\{2_{110} 000\}$	$\{m_{001} 000\}$	$\{m_{1\bar{1}0} 000\}$
M_x	M_x	M_y	$-M_x$	$-M_y$
M_y	M_y	M_x	$-M_y$	$-M_x$
M_z	M_z	$-M_z$	M_z	$-M_z$
χ_P	1	1	1	1
χ_A	3	-1	-1	-1
$\chi_M^{Q_{ICM}}$	3	-1	-1	-1
$\chi_1^{Q_{ICM}}$	1	1	1	1
$\chi_2^{Q_{ICM}}$	1	1	-1	-1
$\chi_3^{Q_{ICM}}$	1	-1	1	-1
$\chi_4^{Q_{ICM}}$	1	-1	-1	1

TABLE 5.2: Representational Analysis of $\text{Nd}_{1-x}\text{Ce}_x\text{CoIn}_5$ with $Q_{ICM} = (0.45, 0.45, 1/2)$. Transformation of the general moment vector, $M = (M_x, M_y, M_z)$ at the magnetic moment site $(0, 0, 0)$ under the little group $G_{Q_{ICM}}$ and character table of the general and irreducible representations of $P4/mmm$ with $Q_{CM} = (q, q, 1/2)$.

c -axis ($R_f = 4\%$). A similar result was obtained for $\text{Nd}_{0.05}\text{Ce}_{0.95}\text{CoIn}_5$ using six independent reflections contributing to both magnetic domains ($R_f = 14\%$). The magnetic structure is an amplitude modulated SDW and depicted in Fig. 5.5e for the $(q, q, 0.5)$ -domain. The refinements reveal an ordered moment $\mu = 0.55(5)\mu_B$ and $0.13(5)\mu_B$ for $\text{Nd}_{1-x}\text{Ce}_x\text{CoIn}_5$ with $x = 0.83$ and 0.95 , respectively, when two equally populated domains are assumed.

The magnetic intensity of all compositions decreases with increasing temperatures, leaving invariant the incommensuration, $q \approx 0.44$, and the width of the magnetic reflections (see Fig. 5.5a and Ref. [28, 251]). The temperature dependent peak intensity of $\text{Nd}_{0.17}\text{Ce}_{0.83}\text{CoIn}_5$ is shown in Fig. 5.5d. We find $T_N = 1.45(3)$ K and observe no change in slope as the temperature is tuned over $T_c < T_N$. This is compatible with a superconducting order parameter that features a node along the magnetic wave-vector and suggests that the $d_{x^2-y^2}$ -symmetry that is found in CeCoIn_5 remains robust for a Nd concentration $1 - x \leq 0.17$ [18, 19].

5.2.4 Competing Energy Scales.

Figure 5.6a displays the maximal amplitude of the magnetic moment, μ_p ($= \sqrt{2}\mu$ for a modulated structure), as a function of the Ce content. The amplitude monotonically decreases from $\mu_p = 2.56(3)\mu_B$ for NdCoIn_5 to $0.90(5)\mu_B$ for $\text{Nd}_{0.39}\text{Ce}_{0.61}\text{CoIn}_5$ maintaining the Ising-like structure with $Q_{CM} = (1/2, 0, 1/2)$ and $(0, 1/2, 1/2)$. The magnetic propagation vector is rotated around the tetragonal c -axis and stabilized at Q_{ICM} for Ce contents larger than $x \geq 0.75$. Between $x = 0.61$ and 0.83 , μ_p is modified only little before it is strongly suppressed for Nd concentrations smaller than 17%.

The evolution of the magnetic moment size in the series is in agreement with $T_N(x)$ as revealed by the xT -phase diagram of $\text{Nd}_{1-x}\text{Ce}_x\text{CoIn}_5$ (see Fig. 5.5b). Here, our results (open symbols) have been added to the macroscopic phase diagram reported in Ref. [27] (closed symbols). The phase diagram provides evidence for a competition between different energy scales.

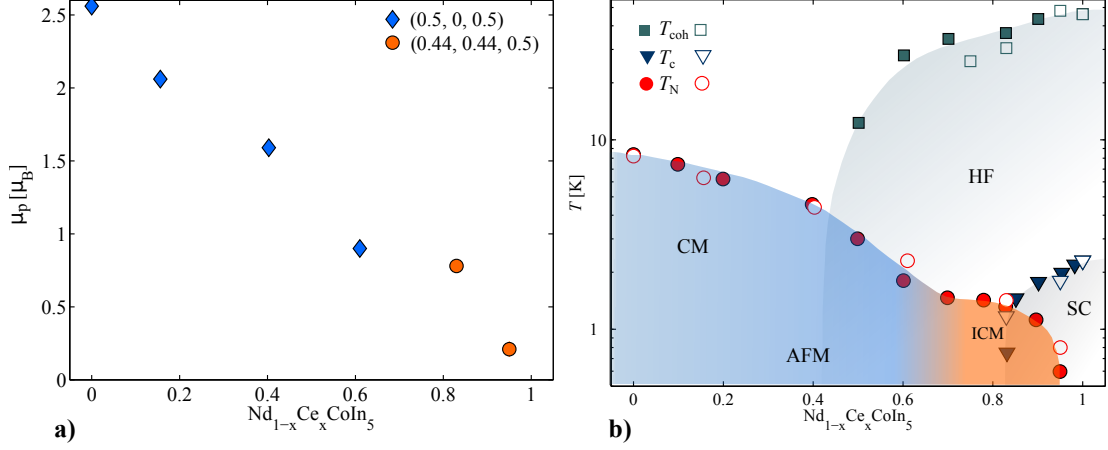


FIGURE 5.6: Updated xT -Phase Diagram of $\text{Nd}_{1-x}\text{Ce}_x\text{CoIn}_5$. a) Substitution dependent magnetic moment amplitude in $\text{Nd}_{1-x}\text{Ce}_x\text{CoIn}_5$. b) Modified xT -diagram of $\text{Nd}_{1-x}\text{Ce}_x\text{CoIn}_5$. Filled symbols represent data taken from Ref. [27].

CeCoIn_5 features $d_{x^2-y^2}$, HF superconductivity in the vicinity of a SDW quantum critical point with suppressed magnetic order [17–20, 197]. The system features a large Fermi surface below the Kondo coherence temperature $T_{coh} \approx 46$ K. Increasing Nd concentrations smaller than 17% steadily reduce the superconducting pairing strength that is thought to emerge from the condensation of hybridized electrons [27, 74]. Superconductivity vanishes around $x \approx 0.83$ and Nd concentrations larger than 50% suppress the heavy-fermion ground state. Larger Nd concentrations trigger magnetic order that is attributed to a dominating small Fermi surface. Thus, the xT -phase diagram of $\text{Nd}_{1-x}\text{Ce}_x\text{CoIn}_5$ shows some similarities to $\text{Yb}(\text{Rh}_{1-x}\text{Co}_x)_2\text{Si}_2$ under field (see Fig. 2.4II) and represents a case, where the Kondo coupling strength is tuned via chemical substitution.

T_N and μ continuously increase with increasing Nd concentration [13, 27]. This provides evidence that the amplitude modulated magnetic structure within the large Fermi surface originates from a magnetic instability of uncompensated localized moments. If a SDW instability arose from nesting a decreasing ordered moment is expected with decreasing x , since the Kondo coupling is gradually reduced.

This may be consistent with a microscopic study of $\text{Nd}_{0.05}\text{Ce}_{0.95}\text{CoIn}_5$ that treats the case where a 5% concentration of magnetic impurities is randomly distributed within the crystal lattice [255, 256]. The model predicts that RKKY-mediated long-range order is established by the strong magnetic fluctuations that arise from the SDW quantum critical point in the proximity of CeCoIn_5 . It is noted that another scenario has been proposed, where magnetic order in 5% Nd doped CeCoIn_5 is caused by the condensation of the superconducting resonance [257]. However, the resonance in $\text{Nd}_{0.05}\text{Ce}_{0.95}\text{CoIn}_5$ features a finite energy transfer as it is

shown in chapter 5.5.

A superconducting $d_{x^2-y^2}$ order parameter is compatible with \mathbf{Q}_{ICM} but does not favor magnetic order along \mathbf{Q}_{CM} . A similar argument applies for a Kondo gap that appears around the Γ -point as it is the case in CeCoIn_5 [54]. In consequence, a magnetic structure that is propagating along the diagonal direction of the tetragonal unit cell is expected for small Nd concentrations. In contrast, many isostructural compounds with localized rare-earth ions feature a commensurate magnetic wave-vector. Moreover, in NdCoIn_5 , NdRhIn_5 and Nd_2RhIn_8 the ordered moments are identical, which suggests a robust crystal electric field ground state that stabilizes a magnetic orientation along the tetragonal c -axis [253].

Naively, this predicts a change from \mathbf{Q}_{CM} to \mathbf{Q}_{ICM} at $\text{Nd}_{0.5}\text{Ce}_{0.5}\text{CoIn}_5$, as a coherent Kondo lattice is stabilized for Ce concentrations larger than 50%. However, the observed anomaly appears between $x = 0.61$ and 0.75 . This may result from the difference in the energy scale triggered by the Nd and Ce atoms in the 115-compounds. The ground state wave-function of NdRhIn_5 is reported and described by a mixture of three multiplets, *i.e.*, $|0\rangle = -0.028|\pm 9/2\rangle - 0.109|\pm 1/2\rangle + 0.994|\mp 7/2\rangle$ [258]. In contrast, CeCoIn_5 features an admixed doublet with $|0\rangle = 0.36|\pm 5/2\rangle + 0.93|\mp 3/2\rangle$ [259]. The fraction of the two expected localized moments, $\mu_{ex}^{Ce}/\mu_{ex}^{Nd}$, yields 33% which is in line with the shift of the magnetic transition towards the Ce-dominated part of the phase diagram. The scenario is supported by the magnetic entropy released at $T_N(x)$ that scales with the Nd concentration up to $x = 0.4$ [27]. This implies that the Ce ions do not play a direct role in the formation of the Ising-like structure.

It is noted that two different magnetic phases have also been observed in the phase diagram of $\text{Nd}_{1-x}\text{Ce}_x\text{RhIn}_5$ [260]. In contrast to the Co family, the antiferromagnetic Kondo phase features a decreasing T_N with increasing Nd content that extrapolates to zero for $x = 0.7$. At larger Nd concentrations an antiferromagnetic phase is emerging with increasing T_N as x is reduced. The magnetic structure in Nd doped CeRhIn_5 is, however, thought to be different from the one in $\text{Nd}_{1-x}\text{Ce}_x\text{CoIn}_5$. The magnetic ground state in CeRhIn_5 is a spiral structure along the tetragonal c -axis with a moment orientation in the basal plane and $\mathbf{Q}_S = (1/2, 1/2, 0.297)$ [244]. In consequence, the localized Nd^{3+} Ising spins may disturb the in-plane order and suppress the spiral structure before magnetic order with a moment orientation perpendicular to the plane is stabilized [260].

In $\text{Nd}_{1-x}\text{Ce}_x\text{CoIn}_5$ both structures feature the same moment orientation, which may allow a continuous change between \mathbf{Q}_{CM} and \mathbf{Q}_{ICM} for $0.61 < x < 0.75$. In fact, a notable change in the incommensuration, q , is observed from $q = 0.448(1)$ in $\text{Nd}_{0.05}\text{Ce}_{0.95}\text{CoIn}_5$ (see Fig. 5.1 and 5.9b) to $q = 0.438(1)$ in $\text{Nd}_{0.17}\text{Ce}_{0.83}\text{CoIn}_5$ (see Fig. 5.5a). The statistics measured on $\text{Nd}_{0.25}\text{Ce}_{0.75}\text{CoIn}_5$ did not allow to conclude whether this trend continues for larger Nd concentrations.

5.2.5 Summary.

The substitution of Nd for Ce in CeCoIn_5 yields a competition between localized moment magnetism and Kondo physics, where magnetic order is observed for Nd concentrations larger than 5% [27]. Our neutron diffraction study reveals two different magnetic structures in the xT -phase diagram of $\text{Nd}_{1-x}\text{Ce}_x\text{CoIn}_5$ that reflect the dominating energy scale of the underlying physics. Magnetism features an Ising-like structure along the tetragonal c -direction for $x \leq 0.61$ with magnetic wave-vectors $\mathbf{Q}_{CM} = (1/2, 0, 1/2)$ and $(0, 1/2, 1/2)$. With increasing Ce concentration the propagation vector is rotated around the tetragonal axis towards

$Q_{ICM} = (q, \pm q, 1/2)$, with $q \approx 0.44$ for $x \geq 0.75$. Here, an amplitude modulated SDW is found that shows a competing coexistence with $d_{x^2-y^2}$ superconductivity for $x \geq 0.83$.

The ordered magnetic moment, $\mu(x)$, scales with the Néel temperature, $T_N(x)$, suggesting that magnetism arises from partially unscreened localized Nd moments for $0.5 < x < 1$. We observe that the modification of the magnetic structure does not appear at a Nd concentration of 50%, where the Kondo lattice is established. We argue that the shift towards the Ce-dominated part of the phase diagram arises from the difference in the energy scales represented by the crystal-field ground state of NdCoIn₅ and CeCoIn₅.

5.3 THE Q-PHASE IN 5% ND DOPED CE_{CO}IN₅

The Q-phase is highly sensitive upon stoichiometric substitution and suppressed at extremely small impurity concentrations (see chapter 4.4). The localized Nd³⁺ electrons in the series Nd_{1-x}Ce_xCoIn₅ act directly on the hybridized 4*f*-bands [27], which may allow a controlled tuning of the correlated superconducting ground state. Experimental realizations with $0.75 \leq x \leq 0.95$ feature a magnetic structure that is alike the one of the Q-phase in CeCoIn₅ (see chapter 5.2.1 and Ref. [23]). It is unclear how this SDW order is related to the Q-phase and whether it may even exist at zero field. Here, we investigate the *HT*-phase diagram of Nd_{0.05}Ce_{0.95}CoIn₅ that reflects a small perturbation to the undoped CeCoIn₅ ground state [28].

5.3.1 Macroscopic Measurements.

The field dependent upper critical field, $\mu_0 H_{c_2}(T)$ was determined via electrical resistivity and heat capacity measurements down to $T = 0.6$ K at the Commissariat à l’Energie Atomique et aux Energies Alternatives, Grenoble France (see Fig. 5.7). Electrical resistivity measurements along the tetragonal *a*-axis reveal a RRR ≈ 3.6 with a sharp superconducting transition at $T_c = 1.8$ K in zero field. The heat capacity results display a supplementary broad transition inside the superconducting condensate, $T_N(0 \text{ T}) = 0.8$ K, that is attributed to the antiferromagnetic state and that is observed only at zero field. The superconducting transition shifts to lower temperatures for increasing magnetic field strengths applied in the tetragonal plane and yields $\mu_0 H_{c_2}(T)$ that is shown in the inset of Fig. 5.7b. The behavior of the upper critical field is similar to the one of CeCoIn₅ and saturates at $\mu_0 H_{c_2} = 11.5$ T for $\mathbf{H} \parallel [1 0 0]$.

5.3.2 Experimental Details.

The field dependent magnetic properties of 5% Nd doped CeCoIn₅ were studied by means of single crystal neutron diffraction on the lifting-counter two-axis spectrometer D23 and on the triple-axis spectrometers IN12 at the ILL and RITA-II at SINQ. The single crystal ($m = 64$ mg) that was used is described in chapter 5.1. The instruments were equipped with vertical-field magnets and dilution inserts, such that fields up to $\mu_0 H = 12$ T and temperatures down to $T = 40$ mK were achieved. The sample was aligned in the scattering plane perpendicular to $[1 -1 0]$ and was exposed to a neutron wavelength $\lambda = 1.28, 4.83$ or 4.217 Å for D23, IN12 and RITA-II, respectively. IN12 and RITA-II were used in configurations as depicted in Fig. 3.2b and 3.3a with an additional $\alpha = 80^\circ$ collimator in front of the sample. On RITA-II we additionally employed a pyrolytic graphite filter before and a beryllium filter after the sample. The nine-bladed multianalyzer allowed a simultaneous measurement of the scattered signal

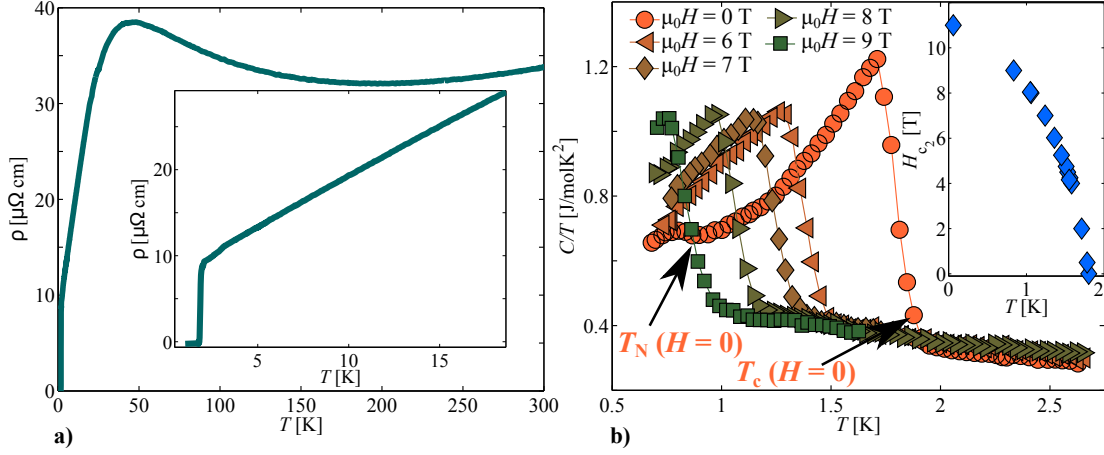


FIGURE 5.7: Field dependent Upper Critical Field of $\text{Nd}_{0.05}\text{Ce}_{0.95}\text{CoIn}_5$. a) Temperature dependent electrical resistivity measured along the a -axis. b) Heat capacity results for different magnetic fields applied in the tetragonal basal plane. Inset: Field dependent upper critical field, $\mu_0 H_{c_2}(T)$, of $\text{Nd}_{0.05}\text{Ce}_{0.95}\text{CoIn}_5$. Modified from [28].

(intensity in the central analyzing blade) and the background (averaged intensity in the two neighboring side blades).

5.3.3 Two Distinct Magnetic Phases with Identical Symmetry inside the Superconducting Condensate.

The field dependence of the magnetic Bragg peak at $\mathbf{Q}_{ICM} = (q, q, 1/2)$, with $q \approx 0.445$ is shown in Fig. 5.8 for $\mathbf{H} \parallel [1 -1 0]$. Diffracted neutron intensity was measured along the wave-vector $(q, q, 0.5)$ in the tetragonal plane for various magnetic fields at a temperature $T = 40$ mK. We observe a well-defined magnetic Bragg peak at zero field with auxiliary field-induced intensity at $\mu_0 H = 4$ T and suppressed order around $\mu_0 H^* \approx 8$ T. Magnetic order reappears at a similar wave-vector for higher fields, where the intensity increases with increasing fields before it collapses between $\mu_0 H = 10.5$ and 12 T.

The magnetic Bragg peaks were fitted with a Gaussian line shape, providing evidence that the width of the reflections are long-range ordered and resolution-limited for all fields. In such cases the background-subtracted and position-optimized peak intensity, $I_p - I_{BG}$, is a direct measure of the integrated intensity, *i.e.*, $I_{int} \propto (I_p - I_{BG})\Gamma$. Γ is the width of the Bragg peak. The field dependence of I_p is displayed in Fig. 5.9a at $T = 40$ mK (orange circles) and overplotted with the background intensity (blue diamonds). The optimized peak positions have been obtained from a fit of all measured magnetic Bragg peaks. Its field dependence is shown in Fig. 5.9b. A linear decrease of the wavenumber from $q \approx 0.448$ at zero field to $q \approx 0.441$ at 10.5 T is found. The linear trend is not affected by the suppressed magnetic order around H^* and may be attributed to a robust Fermi surface topology.

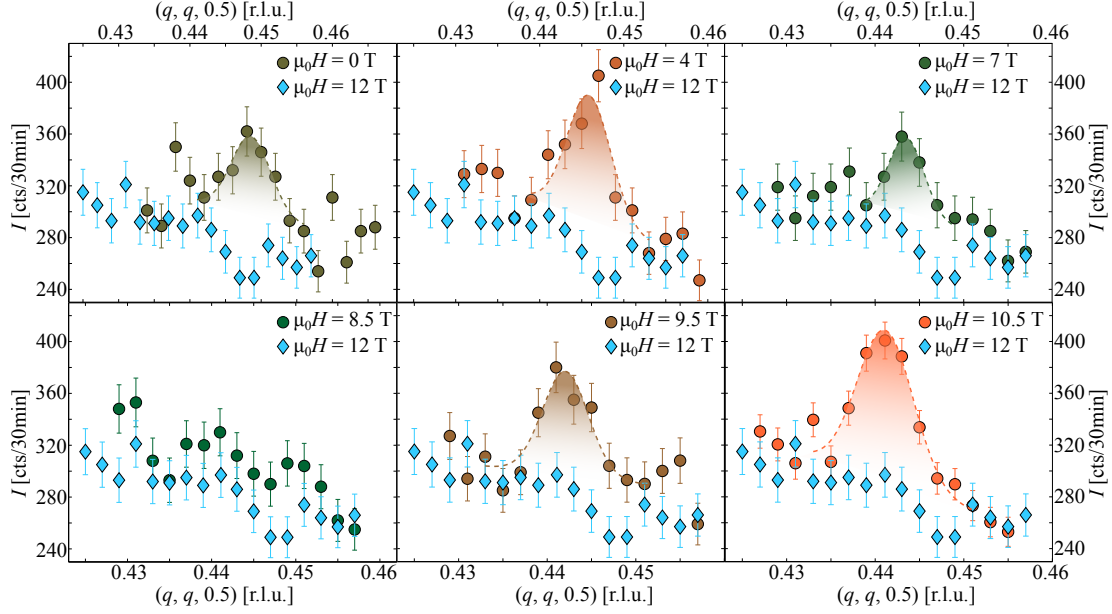


FIGURE 5.8: Two distinct Magnetic Phases in Nd_{0.05}Ce_{0.95}CoIn₅. Diffracted neutron intensity along the tetragonal plane $(q, q, 0.5)$ of Nd_{0.05}Ce_{0.95}CoIn₅ for different magnetic fields along $\mathbf{H} \parallel [1 - 1 0]$ and $T = 40$ mK. Modified from [28].

The field dependent peak intensity, I_p , provides evidence for two distinct magnetic phases that are separated by an instability. At small magnetic fields (SDW-phase), the magnetic intensity increases until it reaches a broad plateau around $\mu_0 H = 4$ T. At larger fields it linearly decreases and vanishes around $\mu_0 H^* \approx 8$ T. Above the field-induced instability the magnetic intensity increases with increasing magnetic field and collapses in a first-order transition together with superconductivity at $\mu_0 H = 11.0(2)$ T[‡]. The behavior of the high-field phase is similar to the one in the Q-phase of CeCoIn₅, hence, we denote this phase also Q-phase. The simultaneous collapse of magnetic order and superconductivity provides direct evidence for an intertwined cooperative ground state, where magnetic order and superconductivity are directly coupled [23, 88, 145].

The peak intensity remains finite in the critical region $H^* \approx 8$ T (see Fig. 5.9a). Neutron diffraction data along $(q, q, 0.5)$, however, show that long-range magnetic order is replaced by a diffuse signal (c.f. Fig. 5.8), which may arise from magnetic fluctuations and short-range order. Evidence for vanishing magnetic order around H^* is also found in the temperature dependent optimized peak intensity, which is displayed in Fig. 5.11 for magnetic fields between

[‡]It is noted that the field dependent electrical resistivity curve reveals $\mu_0 H_{c2} = 11.5$ T for $\mathbf{H} \parallel [1 0 0]$. Neutron diffraction data shown here are measured for $\mathbf{H} \parallel [1 - 1 0]$, where the upper critical field is expected to be 4% lower than for fields along the a -axis (see Fig. 4.5d and Ref. [21, 22]).

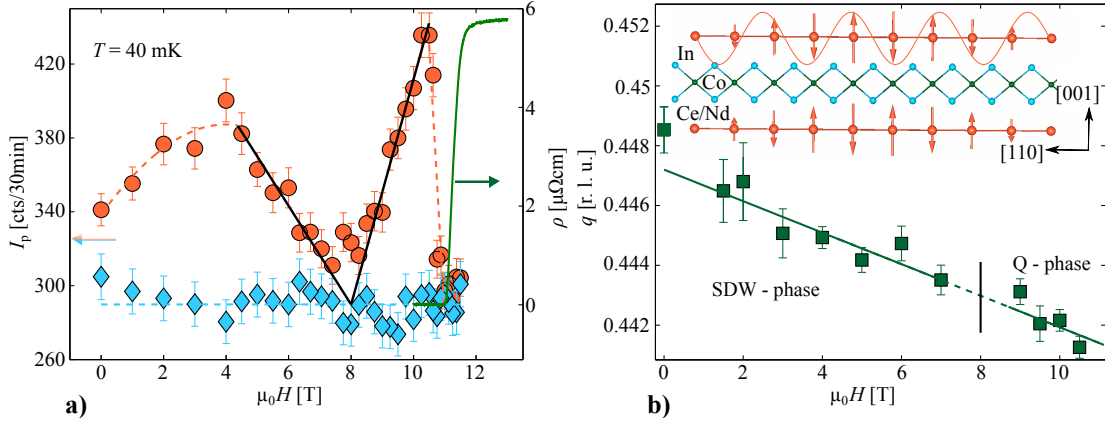


FIGURE 5.9: A Field-induced Magnetic Instability inside the Superconducting Condensate. a) Position optimized peak intensity, I_p as a function of magnetic field for $\mathbf{H}||[1 -1 0]$ in orange and background intensity in blue. The green color represents the resistivity measured along $\mathbf{H}||[1 0 0]$. b) Field dependent in-plane component of the propagation vector ($q, q, 0.5$). Inset: Magnetic structure refined from data that were measured at $\mu_0H = 0$ and 10.5 T. Taken from [28].

$\mu_0H = 7 - 9.5$ T. The magnetic intensity gradually decreases as the magnetic field is increased and disappears in the vicinity of H^* . The signal reappears at larger fields and continuously increases with increasing magnetic field strength. This demonstrates that 5% Nd doped CeCoIn_5 features a field-induced magnetic instability that separates the low-field SDW-phase from the high-field Q-phase.

The magnetic structure of $\text{Nd}_{0.05}\text{Ce}_{0.95}\text{CoIn}_5$ is an amplitude modulated SDW with magnetic moment oriented along the c -axis and ordered moment $\mu = 0.13(5)\mu_B$ at zero field (see chapter 5.2.3). Here, two equally populated domains were assumed, which is consistent with the neutron diffraction data from D10 and D23 and expected for a vanishing magnetic field that does not break the tetragonal space group symmetry (see also chapter 5.4). The field dependent intensity in the SDW-phase shows a broad maximum at $\mu_0H = 4$ T. The absence of the magnetic Bragg peak ($q, q, 2.5$) with $q \approx 0.445$ provides evidence that the moment orientation remains unchanged[§]. At this field the peak intensity doubles when compared to the zero field data, which may result from a constant ordered moment with nonuniform magnetic domain population under field[¶].

The magnetic structure at $\mu_0H = 10.5$ T was refined using six independent magnetic reflections. A refinement in the amplitude modulated representation with moment orientation along the c -axis yields $R_f = 12.6\%$, whereas $R_f > 30\%$ is obtained for other moment orientations.

[§]The magnetic structure factor of the Bragg peak at $(0.445, 0.445, 2.5)$ decreases by 85% if the moment is oriented along the c -axis, while it stays roughly constant for a planar moment orientation.

[¶]The field dependence of the two magnetic domains is discussed in detail in chapter 5.4 and demonstrates that this is the case for $\text{Nd}_{0.05}\text{Ce}_{0.95}\text{CoIn}_5$.

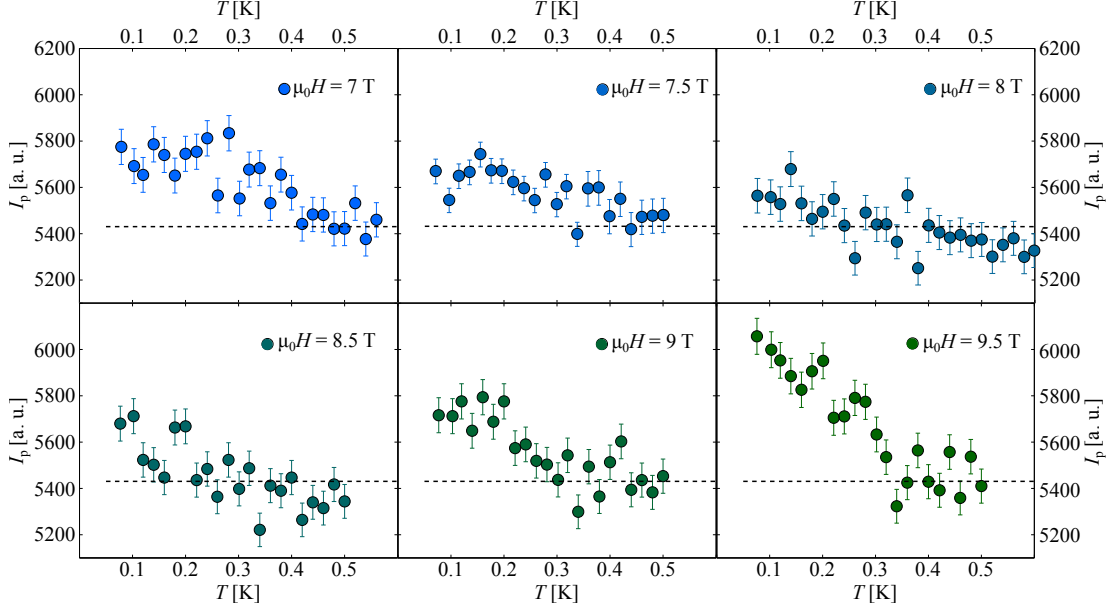


FIGURE 5.10: Temperature dependent Magnetic Intensity in the Critical Region. Temperature dependence of the optimized peak position, I_p , for magnetic fields $\mu_0 H = 7 - 9.5$ T. Modified from [28].

In the Q-phase of CeCoIn₅ one domain is populated while the other one is suppressed [24, 88]. Assuming one populated domain^{||} in the Q-phase of 5% Nd doped CeCoIn₅ leads to an ordered moment $\mu = 0.15(5)\mu_B$ that is consistent with the Q-phase of the undoped compound [23, 145]. Thus, the magnetic instability at H^* separates two antiferromagnetic phases with an identical symmetry inside the superconducting condensate.

5.3.4 Evidence for a Novel Quantum Phase Transition.

The magnetic Bragg peak intensity reveals a linear dependence on the magnetic field strength around H^* . The neutron intensity is proportional to the square of the magnetic moment (see Eq. 3.27 and 3.15). The best fit to the diffraction data yields a field dependent ordered moment $\mu = \mu_0 |H/H^* - 1|^\beta$, with $\beta \approx 0.5$, $\mu_0 H^* = 8.0(2)$ T and $\mu_0 = 0.19(1)$ for $H < H^*$ and $\mu_0 = 0.28(1)$ for $H > H^*$, respectively**. A critical mean-field exponent $\beta = 0.5$ is consistent with the field dependence of the Q-phase in CeCoIn₅ and is expected for a QPT (see chapter 2.2.2 and Ref. [62, 63, 88]).

Support for a field-induced QPT in the superconducting condensate of Nd_{0.05}Ce_{0.95}CoIn₅ is found in the HT -phase diagram that is shown in Fig. 5.11. The colorplots display the background-subtracted peak intensity as a function of temperature and magnetic field. The

^{||}As shown in chapter 5.4 only one domain is populated in the Q-phase of Nd_{0.05}Ce_{0.95}CoIn₅ for $\mathbf{H} || [1 -1 0]$.

**The prefactors result from refinements of the peak intensity shown in Fig. 5.9a

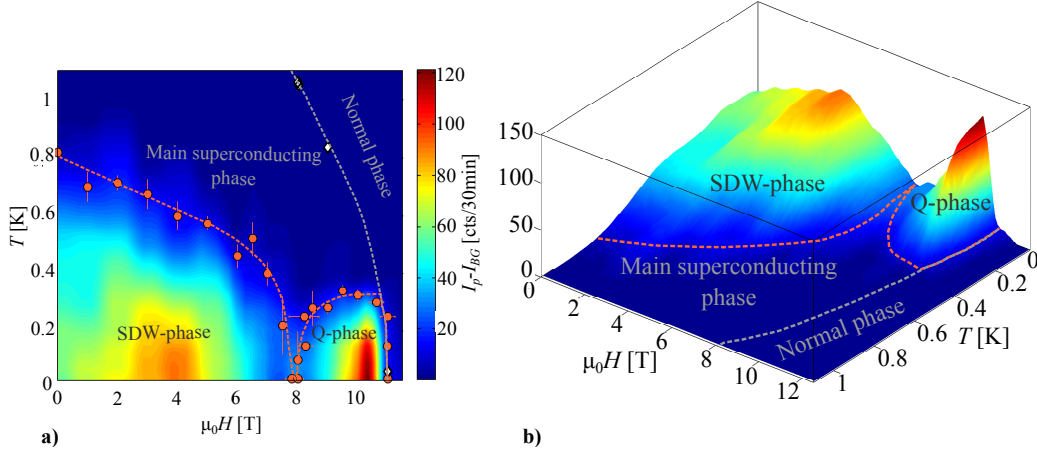


FIGURE 5.11: HT -phase Diagram of $\text{Nd}_{0.05}\text{Ce}_{0.95}\text{CoIn}_5$. **a)** and **b)** Background subtracted magnetic intensity for $\mathbf{H}||[1 \ -1 \ 0]$. Orange circles display magnetic phase boundaries (dashed lines are guides to the eyes). White diamonds represent the superconducting phase boundary that was measured via electrical resistivity and heat capacity. The white dashed line is the renormalized upper critical field curve of CeCoIn_5 . Modified from [28].

data were measured on IN12 and RITA-II and normalized to an intensity corrected standard monitor. The orange circles represent the phase boundary that was obtained from temperature and field scans on the optimized peak position and shown in Fig. 5.9a and 5.10 for $T = 40$ mK and $\mu_0H = 7 - 9.5$ T, respectively. The orange dashed line represents a guide to the eyes and the white line is the upper critical field curve that is normalized from CeCoIn_5 . The white diamonds are upper critical field values of 5% Nd doped CeCoIn_5 that were measured via electrical resistivity and heat capacity (see section 5.3.1).

The Figure displays the two antiferromagnetic phases inside the superconducting d -wave condensate with a fan-shaped critical region that is expanding at higher temperatures. Although we can not provide direct evidence for quantum critical fluctuations in the superconducting phase, the HT -phase diagram suggests a field-induced QPT at H^* .

The Q -phase of 5% Nd doped CeCoIn_5 is only stable for temperatures below $T < 300$ mK and collapses in a first-order transition together with superconductivity. This HT -dependence is similar to the Q -phase of CeCoIn_5 with a QPT that is shifted to lower fields by about 20% maintaining the ratio $\mu_0H^*/k_B T_c$ [28, 88]. These results, thus, demonstrate that the Q -phase is stable under a small perturbation of a 5% Nd concentration on the Ce-site of CeCoIn_5 .

The field-induced QPT separates two antiferromagnetic structures with an identical magnetic symmetry. This prevents the emergence of a magnetic order parameter in one of both phases. Thus, the magnetic instability that is observed at H^* cannot be driven purely by magnetic fluctuations. Charge valence fluctuations at the origin of the instability are excluded,

because a Kondo breakdown is expected for $x \approx 0.5$ in the series Nd_{1-x}Ce_xCoIn₅ (see Fig. 5.1a). In contrast, the two antiferromagnetic phases appear to differentiate in their coupling with superconductivity as the high-field SDW collapses at H_{c2} . We, therefore, suggest that the quantum-phase transition at H^* originates from fluctuations that are related to the superconducting condensate.

The concept of superconductivity-induced magnetism has been discussed for several Pauli-limited superconductors including CeCoIn₅ (c.f. chapter 2.4.3 and 4.3). A direct way to couple d -wave superconductivity with magnetic order in the Q-phase is the emergence of a supplementary superconducting order parameter of p -wave symmetry [153, 222]. This scenario has been supported by neutron diffraction and thermal conductivity measurements [88, 219]. Based on the idea of a non-magnetic primary order parameter a spatially modulated p -wave may induce SDW-order to maintain momentum conservation [153]. The conclusion for an emerging PDW in the Q-phase of CeCoIn₅ was, however, reached from the hypersensitivity of the spin-density modulation direction to in-plane rotations of the magnetic field (see chapter 4.3). This asks for an investigation of the magnetic domain population in the SDW- and Q-phase of 5% Nd doped CeCoIn₅ for various magnetic field directions (see chapter 5.4).

The diffuse signal that appears in proximity of H^* does not allow to conclude, whether the magnetic instability appears at a single quantum critical point (see Fig. 5.11a), or whether the two phases can separate for Nd_{1-x}Ce_xCoIn₅ with $x > 0.95$. The latter scenario is supported by a recent theoretical study on the field dependence of the SDW-phase. Here, a distribution RKKY-mediated Nd moments were assumed to be oriented along the c -axis [256]. The authors find that an in-plane field triggers a canting of the localized Nd moments that leads to the reduction of localized order. The critical field, where the SDW-phase is suppressed depends on the saturated ordered moment and can, thus, differentiate from the critical field where the Q-phase emerges. It is noted that the overlap of the SDW- and the Q-phase for experimental realizations with $x < 0.95$ may be complicated, since both phases involve the same low-energy quasiparticles along the superconducting node.

An increasing Nd concentration in the series weakens the hybridized bands and leads to a decreasing orbital limiting field $H_{c2}^{orb} \propto m^{*2}$. Since Pauli limiting effects are crucial for the development of the Q-phase (see chapter 4.3), it is likely to vanish at some critical Nd concentration, x_c , larger than 5%. In consequence, the superconducting phase may be embedded inside the SDW-phase for $x_c \leq x < 20\%$. Experimental investigations of the HT -phase diagram for Nd_{1-x}Ce_xCoIn₅ with $x \neq 0.95$ are required to clarify these open questions.

5.3.5 Summary.

The HT -phase diagram of Nd_{0.05}Ce_{0.95}CoIn₅ reveals a magnetic instability at $\mu_0 H^* \approx 8$ T that separates two antiferromagnetic phases with an identical symmetry inside the superconducting condensate [28]. In both phases, the low-field SDW-phase and the high-field Q-phase, an amplitude modulated SDW with a magnetic moment orientation along the c -axis is found that reveals $\mu(0 \text{ T}) = 0.13(5)\mu_B$ and $\mu(10.5 \text{ T}) = 0.15(5)\mu_B$, respectively. The Q-phase of 5% Nd doped CeCoIn₅ collapses at the upper critical field providing evidence for a direct coupling between superconductivity and magnetism, similar to the Q-phase of the undoped compound. Thus, our experiment demonstrates that the Q-phase is stable under a small amount of Nd concentration on the Ce-site. The field dependent Bragg peak intensity suggests a QPT at H^* that is driven by fluctuations related to the superconducting condensate [28].

5.4 DISTINCT DOMAIN SWITCHING IN $\text{Nd}_{0.05}\text{Ce}_{0.95}\text{CoIn}_5$ AT LOW AND HIGH MAGNETIC FIELDS

5% Nd doped CeCoIn_5 features a field-induced magnetic instability that may arise from a modification of the superconducting pairing symmetry [28]. Experimental evidence for an additional superconducting order parameter is, however, lacking. Furthermore, it is unclear why the material reveals an increasing intensity at $\mathbf{Q}_{ICM} = (q, q, 0.5)$ with $q \approx 0.445$ for magnetic field strengths between $\mu_0 H = 0 - 4$ T and $\mathbf{H} \parallel [1 -1 0]$ (see Fig. 5.11a).

The multicomponent ground state of the Q-phase in CeCoIn_5 is hypersensitive to the magnetic field direction in the tetragonal plane (see Fig. 4.5 and Ref. [88, 219]). Neutron diffraction studies show that only one of both spin-density modulation directions, $\mathbf{Q}_{1,2} = (q, \pm q, 0.5)$, is present for all in-plane field orientations and that it can be switched when the magnetic field is rotated around the $d_{x^2-y^2}$ -wave antinode ($\mathbf{H} \parallel [0 1 0]$) [88]. This behavior has been attributed in the past either to spin-orbit coupling, to an anisotropic spin susceptibility of a spin-triplet superconducting order parameter or to a field-sensitive FFLO-phase [88, 158, 220].

A careful investigation of the two magnetic domains, $\mathbf{Q}_{1,2}$, in the SDW- and Q-phase of $\text{Nd}_{0.05}\text{Ce}_{0.95}\text{CoIn}_5$ for different in-plane field orientations may shed more light onto these open questions [29].

5.4.1 Experimental Details.

The neutron diffraction experiments were carried out on D23 ($\lambda = 1.27 \text{ \AA}$) using a vertical magnet with a dilution insert at a base temperature of $T = 40$ mK and with a maximal field strength of $\mu_0 H = 11.9$ T. The single crystal was oriented in the scattering plane perpendicular to $[1 -1 0]$ or with a vertical axis around $[0 1 0]$. The magnetic Bragg peaks above the scattering plane were detected using the lifting-arm detector of the instrument. In the latter sample orientation the single crystal was mounted on a non-magnetic piezoelectric sample rotator (of type ANGt50 from attocube systems AG), which enabled a sample rotation of $\pm 3^\circ$ around the $[0 0 1]$ -direction inside the dilution refrigerator. Detailed information on the sample holder is found in the Supplementary Materials of Ref. [88] and Ref. [24]. The vertical sample tilt with respect to the field direction was determined by the out-of-plane angle of the nuclear $(2, 0, 0)$ Bragg peak. The angle between the magnetic field orientation in the tetragonal basal plane and the a -axis is denoted as ψ (see schematic illustration in Fig. 5.14 and 5.15).

5.4.2 Domain Switching in the SDW-phase.

The spin-density modulation direction $\mathbf{Q}_1 = (q, q, 0.5)$ is oriented in the plane perpendicular to a magnetic field along $[1 -1 0]$. The domain features an increasing magnetic intensity when the magnetic field is tuned from $\mu_0 H = 0$ to 4 T (see Fig. 5.9a) [28]. An antagonistic behavior is observed in the other modulation direction, $\mathbf{Q}_2 = (q, -q, 0.5)$, that is directed along the field. As shown in Fig. 5.12 the magnetic Bragg peak intensity of the \mathbf{Q}_2 -domain decreases with increasing magnetic field strength and is suppressed for fields larger than $\mu_0 H_d \approx 3.5$ T.

The field dependence of the integrated intensity in the two domains, $\mathbf{Q}_{1,2}$, is shown in Fig. 5.13 and compared to their total sum $I_{tot} = I_{Q_1} + I_{Q_2}$. The plot combines the integrated intensities I_{Q_1} and I_{Q_2} that are shown in Fig. 5.12 and 5.9a and that were measured at $T = 40$ mK and $\mathbf{H} \parallel [1 -1 0]$. The two data sets were normalized to equally populated domains at zero field, which is consistent with the observations on D10 and where the tetragonal crystal symmetry is

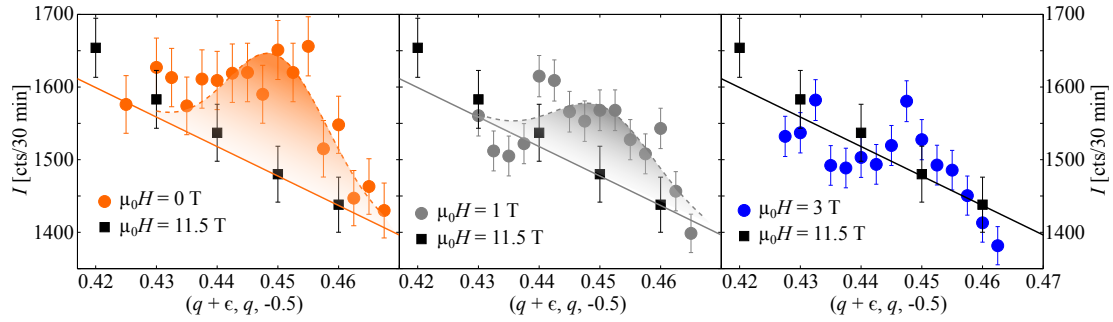


FIGURE 5.12: Field dependent Intensity in the SDW-phase. Diffracted neutron intensity on $\text{Nd}_{0.05}\text{Ce}_{0.95}\text{CoIn}_5$ along the tetragonal plane $(q+\epsilon, q, -0.5)$, for different magnetic fields along $\mathbf{H}||[1 -1 0]$ and $T = 40$ mK. ϵ was chosen such that the scan was centered at $(1, 0, 0) - \mathbf{Q}_2$, in accordance to the field dependence of the incommensuration q (see Fig. 5.9b).

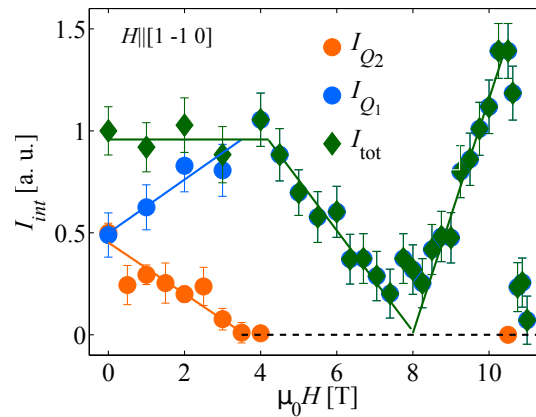


FIGURE 5.13: Field-induced Domain Imbalance. Field dependence of the two magnetic domains $\mathbf{Q}_{1,2}$ in $\text{Nd}_{0.05}\text{Ce}_{0.95}\text{CoIn}_5$ for $\mathbf{H}||[1 -1 0]$ and $T = 40$ mK. The total intensity, I_{tot} , represents the sum of the intensities in the two domains. Taken from [29].

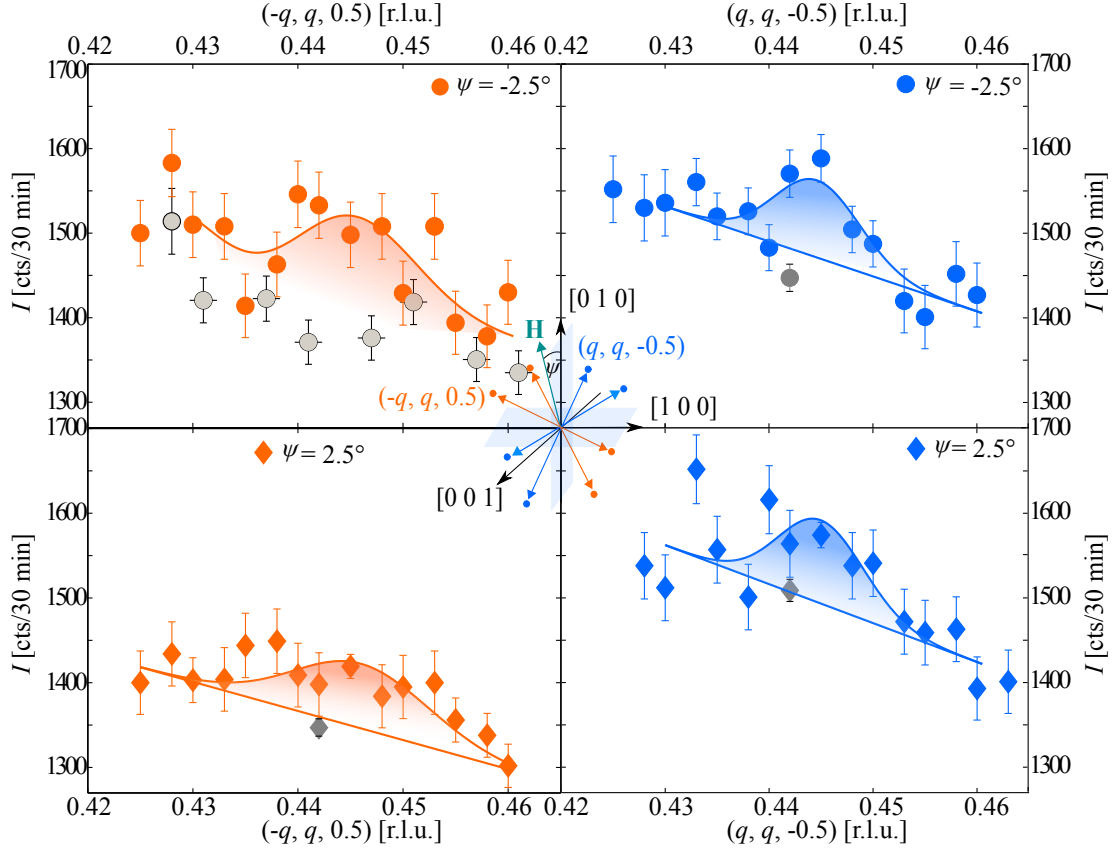


FIGURE 5.14: Switching in the SDW-phase. Diffracted neutron intensity of Q_1 (blue) and Q_2 (orange) in the SDW-phase for magnetic field orientations close to the a -axis. The magnetic signal at $\mu_0 H = 2$ T and $T = 40$ mK was measured along $(\pm q, q, \mp 0.5)$ and the background in gray was detected at $\mu_0 H = 11.9$ T. Taken from [29].

not broken by an in-plane field.

Our results reveal a redistribution of the intensity at low fields. While I_{Q_2} gradually decreases with increasing magnetic field strength, the magnetic intensity in Q_1 is enhanced, such that the total intensity remains constant. Fields larger than $\mu_0 H_d = 3.6(6)$ T yield a monodomain state, where only magnetic intensity of the Q_1 -domain contributes to the total intensity. A single modulation direction in the Q -phase is also observed in $CeCoIn_5$ [24, 88].

The field-induced change of the relative domain population in the SDW-phase yields $I_{Q_1}/I_{Q_2} \approx 4$ at $\mu_0 H = 2$ T for $H \parallel [1 -1 0]$. This is not the case for magnetic field orientations close to the tetragonal a -axis (see Fig. 5.14), where intensity in Q_1 and Q_2 was measured for a tilt of $\psi = \pm 2.5^\circ$. The results reveal two equally populated magnetic domains with an intensity that is robust for small field rotations around $H \parallel [0 1 0]$. The difference in the magnetic domain

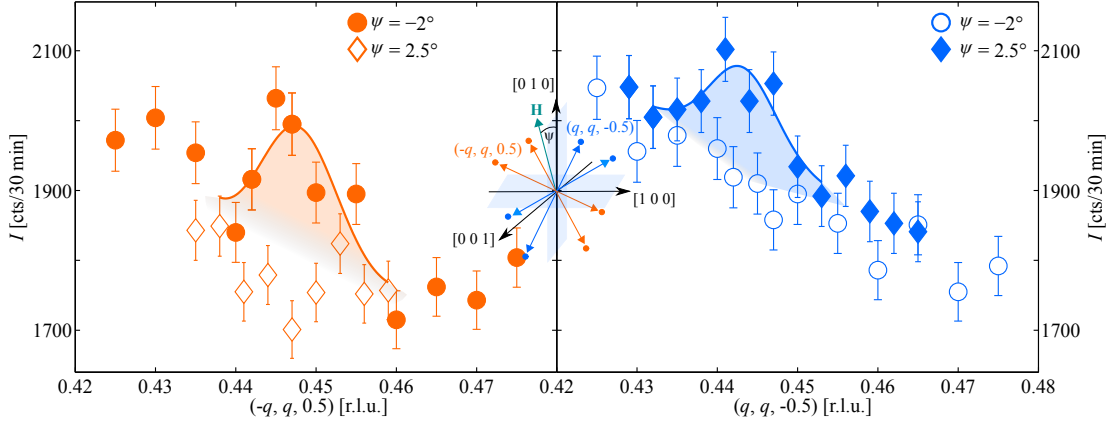


FIGURE 5.15: Switching in the Q-phase. Diffracted neutron intensity of Q_1 (blue) and Q_2 (orange) in the Q-phase for magnetic field orientations close to the a -axis. The magnetic signal at $\mu_0 H = 10.4$ T and $T = 40$ mK was measured along $(\pm q, q, \mp 0.5)$. Taken from [29].

population for $\mathbf{H} \parallel [0\ 1\ 0]$ and $\mathbf{H} \parallel [1\ -1\ 0]$ suggests that the magnetic field direction triggers a continuous change in the domain population as it is rotated from $\psi = 0$ to 45° .

5.4.3 Domain Switching in the Q-phase.

A distinct switching behavior is observed in the high-field Q-phase. Magnetic Bragg peaks that are measured at $\psi = 2.5$ and -2° are shown in Fig. 5.15. We find a populated Q_1 -domain with suppressed intensity in Q_2 for $\psi = 2.5^\circ$ and an opposed magnetic distribution for $\psi = -2^\circ$. This shows that for each field orientation in the Q-phase only the magnetic domain more perpendicular to the magnetic field is populated. As the magnetic field is rotated around the tetragonal a -axis, the domain population is switched.

A high sensitivity to the in-plane field orientation is also found in the Q-phase of CeCoIn_5 [88]. Here, the domain population is changed in a first-order transition at $\mathbf{H} \parallel [0\ 1\ 0]$ with a hysteretic region of about $\Delta\psi \approx 0.2^\circ$. Substituting the Ce-site with 5% Nd triggers a broadening of the first-order switch. Figure 5.16 displays the angular dependence of I_{Q_1} and I_{Q_2} for small misalignments of the magnetic field orientation with respect to the a -axis of $\text{Nd}_{0.05}\text{Ce}_{0.95}\text{CoIn}_5$. A continuous change of the relative domain population with a crossover region of $\Delta\psi \approx 5^\circ$ is observed.

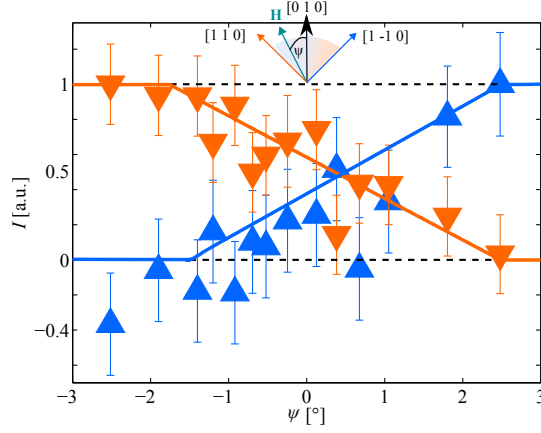


FIGURE 5.16: Domain Population in the Q-phase. Background subtracted peak intensity for fields in the proximity of the tetragonal a -axis and $\mu_0 H = 10.4$ T. The orange color represents the Q_2 - and the blue color the Q_1 -domain. Taken from [29].

5.4.4 Evidence for Spin-Orbit Interactions with Modified Magneto - Superconducting Coupling.

The magnetic moment in 5% Nd-doped $CeCoIn_5$ is oriented along the tetragonal c -axis, perpendicular to an in-plane field direction [28]. The Zeeman interaction, \mathbf{MH} , does not affect the magnetic order in Q_1 and Q_2 for such a configuration and cannot drive the observed domain imbalance.

An anisotropic spin susceptibility has been found previously in non-centrosymmetric materials, such as $CePt_3Si$, where it is thought to arise from spin-orbit interactions [261, 262]. $CeCoIn_5$ is a centrosymmetric multiband material [18, 19, 50, 188], but it has been shown that in such systems the spin-orbit coupling can reduce the tetragonal symmetry when a magnetic field is applied in the basal plane [220]. Based on this approach, recent reports model the material by means of a phenomenological Landau free energy density, F , in which a weak spin-orbit coupling is included [220, 263]:

$$F = -\frac{\alpha}{2}\mu^2 + \frac{\beta}{4}\mu^4 - \gamma(\nabla_{2d}\mu)^2 + \eta[(\partial_x^2\mu)^2 + (\partial_y^2\mu)^2] - \lambda[(\mathbf{H} \cdot \nabla_{2d})\mu]^2. \quad (5.1)$$

Here, the ordered moment, μ , is the order parameter, $\nabla_{2d} = (\partial_x, \partial_y)$ and α , β , γ , η and λ are phenomenological coefficients. α and β define the strength of the order parameter, γ and η account for its anisotropy and λ represents the spin-orbit coupling [263]. A magnetic structure that is amplitude modulated and oriented along the c -axis yields the domain dependent ordered moments [263]:

$$\mu_{1,2} = \sqrt{2} \sqrt{\frac{\alpha\eta + \gamma^2 + H^2\gamma\lambda[1 \pm \sin(2\psi)]}{3\beta\eta}}, \quad (5.2)$$

where $\mu_{1,2} \neq 0$ if $\sin(2\psi) \geq -G = -(\gamma^2 + \alpha\eta + H^2\gamma\lambda)/(H^2\gamma\lambda)$ and $\sin(2\psi) \leq G$, respectively.

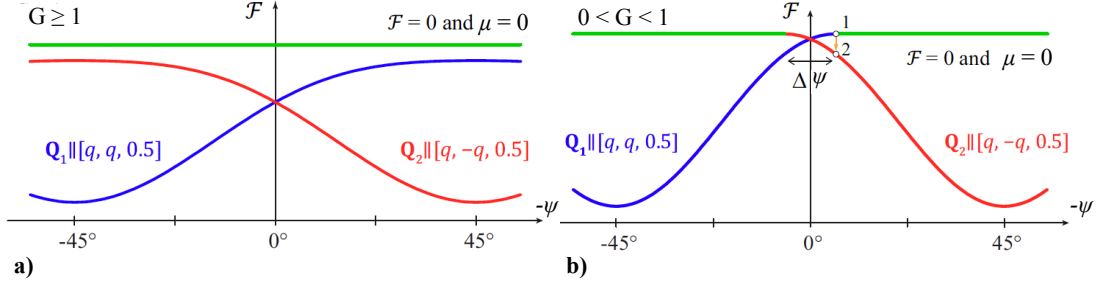


FIGURE 5.17: Free Energy of the Spin-Orbit coupled Landau Model. Landau Free energy density as a function of ψ for $G \geq 1$ in **a)** and $0 < G < 1$ in **b)**. The Free energy density of \mathcal{Q}_1 and \mathcal{Q}_2 are represented in blue and red, respectively. The green line represents the non-magnetic state. Modified from [263].

Depending on the size of G , the model distinguishes among the cases where no magnetic order exists ($G \leq -1$), where the change of the spin-density modulation direction involves a non-magnetic state around $\psi = 0$ ($-1 < G \leq 0$), where the domain switches in a first-order transition at $\psi = 0$ ($0 < G < 1$) or where two magnetic domains always coexist ($G \geq 1$) [263].

The free energy density of the latter scenario is depicted in Fig. 5.17a. It predicts two equally populated domains for $\psi = 0^\circ$ and a continuous change of the relative ordered moment, $\mu_{1,2}$, as the field is rotated away from the a -axis [263]. The largest difference in domain population is predicted at $\psi = \pm 45^\circ$. This is consistent with the behavior that is observed in the SDW-phase, where $I_{Q_1}/I_{Q_2} \approx 1$ and 4 is found at $\mu_0 H = 2$ T for $\mathbf{H} \parallel [0\ 1\ 0]$ and $[1\ -1\ 0]$, respectively (see Fig. 5.13 and 5.14). Furthermore, the model predicts a linear field dependence on I_{Q_1} and I_{Q_2} , which is in agreement with our experiment for field strengths smaller than H_d (see Fig. 5.13) [263]. This provides evidence that spin-orbit interactions trigger the anisotropic spin susceptibility in the SDW-phase and the coupling is described within a Landau model with $G \geq 1$.

In strong contrast, the case $G \geq 1$ does not allow to predict the behavior in the Q-phase, where a sharp switch is found (see Fig. 5.15). The Landau model describes this scenario for $0 < G < 1$, where the Free energy density features an angular dependence such as shown in Fig. 5.17b [263]. Here, the modulation direction changes in a first-order transition at $\mathbf{H} \parallel [0\ 1\ 0]$ that may be broadened by the Nd disorder in the material.

The neutron diffraction results demonstrate that the spin-orbit interactions present at low fields would have to be modified at high-fields. While the phenomenological Landau coefficients do not feature a field dependence that can directly account for this difference, they also reflect the microscopic interactions in the system [263]. We, thus, conclude that the coupling between magnetism and superconductivity is altered above the field-induced QPT and places the Q-phase within the scenario $0 < G < 1$. However, the Landau theory that is shown in Eq. 5.1 can not describe the order parameter in the Q-phase that reflects the modified magneto-

superconducting coupling.

5.4.5 A Spatially-Modulated Cooper Pair-Density Wave at the Origin of the Q-phase.

It has been proposed previously that magnetic order in the Q-phase is intertwined with superconductivity via an additional superconducting order parameter [221, 222]. Although these theories rely on spin-orbit interaction, they also require Pauli limiting properties of the superconducting condensate and lead to a different Landau theory with the two possible lowest linear-order coupling terms [221, 222]:

$$\begin{aligned} V_1 &\propto i\mu(\Delta_d^*\Pi_{-Q} - \Delta_d\Pi_Q^*) + c.c \\ V_2 &\propto H\mu(\Delta_d^*\Pi_{-Q} + \Delta_d\Pi_Q^*) + c.c. \end{aligned} \quad (5.3)$$

Here, the ordered moment, μ , represents the magnetic order parameter, Δ_d is the superconducting d -wave order parameter, Π_Q the supplementary superconducting order parameter that features spin-triplet pairing and H the magnetic field. It has been extensively debated in the past whether the Q-phase features a spin-triplet PDW that induces SDW order or a FFLO-state where spin-triplet superconductivity is triggered by SDW order [221, 222]. However, only the PDW scenario is consistent with a non-magnetic primary order parameter that is postulated by the robust magnetic symmetry in $\text{Nd}_{0.05}\text{Ce}_{0.95}\text{CoIn}_5$ [28].

The opening of an additional superconducting gap in the Q-phase is in agreement with thermal conductivity results of undoped CeCoIn_5 that provide evidence for a reduced quasiparticle excitation spectrum along the suppressed Q -domain (see Fig. 4.5d and e). A general symmetry analysis supports V_1 as the correct coupling term [24, 88]. It yields two possible sets of PDW Eigenvectors that represent a spatially modulated p -wave, which is aligned perpendicular to the present spin-density modulation direction [221]. The broadened first-order change in the domain population of 5% Nd doped CeCoIn_5 may, thus, result from the induced disorder that prevents a coherent switch of the p -wave representation at $\mathbf{H}||[0\ 1\ 0]$.

5.4.6 Summary.

The two magnetic domains, $\mathbf{Q}_{1,2} = (q, \pm q, 0.5)$, of $\text{Nd}_{0.05}\text{Ce}_{0.95}\text{CoIn}_5$ feature a distinct behavior in the SDW- and the Q-phase as the magnetic field is rotated in the tetragonal basal plane [29]. We find indistinguishable magnetic domains in the SDW-phase for $\mathbf{H}||[0\ 1\ 0]$ that continuously change their relative population as the magnetic field is turned to the d -wave node. Here, the intensity in the domain that is perpendicular to the applied field direction is linearly increasing upon increasing field strength, while the other one decreases and vanishes at $\mu_0 H_d \approx 3.5$ T. The results are consistent with the predictions of a phenomenological Landau model that includes spin-orbit interaction and that is valid for multiband metals with a centrosymmetric crystal symmetry [263].

The behavior in the SDW-phase is in contrast to the single spin-density modulation direction that is observed in the Q-phase and that can be switched by small field rotations around the tetragonal a -axis. The difference in the domain selectivity of the SDW- and the Q-phase cannot be explained solely by spin-orbit interaction and requires a modified magneto-superconducting coupling in the Q-phase. Based on a lowest-linear coupling approach that intertwines magnetism and superconductivity, our results suggest the emergence of a spatially-modulated p -wave order parameter at the field-induced QPT [29].

5.5 THE SPIN RESONANCE IN $\text{Nd}_{0.05}\text{Ce}_{0.95}\text{CoIn}_5$

The conclusion for an additional superconducting order parameter in the Q -phase is based on a phenomenological Landau theory that couples magnetism and d -wave superconductivity via a PDW [88, 221]. A promising microscopic theory at the origin of the Q -phase is the softening of a magnetic excitation related to superconductivity at the field-induced quantum phase transition [147]. A collective spin-1 excitation that arises at T_c has been found in several cuprates, HFs and pnictides and is often interpreted as a clear sign of magnetically-driven superconductivity^{††} [91, 92, 104]. When this exciton becomes soft an intertwined state can stabilize, in which static magnetic order is present only inside the superconducting phase. The fluctuations associated to the condensation of the excitation may create a novel superconducting condensate, in which mixed spin-singlet and spin-triplet Cooper pairs coexist.

The spin resonance of CeCoIn_5 reveals an energy gap of $\Delta E = 0.6$ meV ($= 3k_B T_c$) at lowest temperatures and zero field [92]. While its wave-vector has been unclear for some time, high resolution inelastic neutron scattering on about 80 coaligned single crystals has shown recently that it is identical to the propagation vector of static order in the Q -phase [201]. A polarization analysis of these neutron results suggest that the excitation features Ising-like moment fluctuations along the c -axis and, thus, acts as a dynamical precursor of the SDW order. Under magnetic field the resonance splits into two branches and the field dependence of the lower excitation supports the condensation scenario [223, 224, 264].

The Q -phase of 5% Nd doped CeCoIn_5 emerges at a magnetic field strength that is about 20% lower in field when compared to the undoped compound [28]. It features an additional magnetic phase at low fields with a distinct coupling to superconductivity [28, 29]. In this section we aim to answer the open question whether the energy gap of the resonance adjusts accordingly and how the magnetic fluctuations are affected when static order is stabilized at lower temperatures [30].

5.5.1 Experimental Details.

Because of the small cross section, inelastic neutron scattering experiments usually require large sample masses and long counting times. Thus, around fifty $\text{Nd}_{0.05}\text{Ce}_{0.95}\text{CoIn}_5$ single crystals were coaligned with an accuracy of one degree and with the vertical axis parallel to $[1 -1 0]$. A preliminary study on the cold triple-axis spectrometer PANDA at the Heinz Maier-Leibitz Zentrum in Munich, Germany showed a distribution of magnetic order in the sample. At zero energy transfer and zero field two magnetic wave-vectors at $\mathbf{Q}_{AF} = (0.5, 0.5, 0.5)$ and $\mathbf{Q}_{ICM} = (q, q, 0.5)$ with $q \approx 0.45$ were observed.

In a consecutive experiment we searched for the propagation vector of one single crystal with mass $m = 125$ mg and stoichiometry $\text{Nd}_{0.043(2)}\text{Ce}_{0.945(4)}\text{CoIn}_{4.9(1)}$ that was determined by in-beam neutron activation analysis. The measurement was carried out on the thermal triple-axis spectrometer IN22 at the ILL using a neutron wavelength $\lambda = 2.36$ Å. The single crystal was oriented in the scattering plane perpendicular to $[1 -1 0]$ and placed in an orange cryostat

^{††}The microscopic origin of this so-called spin resonance is currently debated within mainly two theoretical models in HF systems [94, 96, 98–100]. While a widespread interpretation assign the resonance to a superconducting exciton, it has also been associated to a magnetic excitation of the hybridized f -electrons (see chapter 2.3.2). The universal scaling behavior of the resonance energy, however, reveals a clear sing for a deep connection between the excitation and unconventional superconductivity [93].

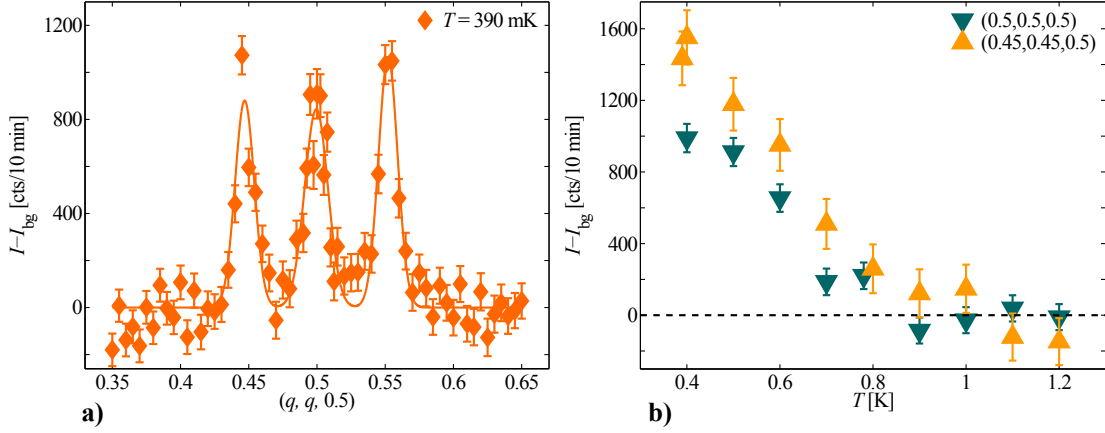


FIGURE 5.18: Two Coexisting Magnetic Wave-Vectors. **a)** Neutron diffraction intensity along $(q, q, 0.5)$ on $\text{Nd}_{0.043(2)}\text{Ce}_{0.945(4)}\text{CoIn}_{4.9(1)}$ with mass $m = 125 \text{ mg}$ at $T = 400 \text{ mK}$. **b)** Temperature dependent background subtracted peak intensity on the two propagation vectors $\mathbf{Q}_{AF} = (0.5, 0.5, 0.5)$ and $\mathbf{Q}_{ICM} = (q, q, 0.5)$ with $q \approx 0.45$.

with ^3He insert.

The neutron diffraction results along the wave-vector transfer $(q, q, 0.5)$ at $T = 400 \text{ mK}$ are displayed in Fig. 5.18a. The background-subtracted intensity^{‡‡} reveals magnetic Bragg peaks that are assigned to the two distinct wave-vectors \mathbf{Q}_{AF} and \mathbf{Q}_{ICM} . The ratio of the integrated intensities shows that the commensurate structure contributes $f \approx 20\%$ to the total intensity, when a similar moment along the c -axis is assumed. The temperature dependence of the two phases is similar and features an identical Néel temperature $T_N = 850(25) \text{ mK}$ (see Fig. 5.18b).

The emergence of the additional commensurate wave-vector $\mathbf{Q}_{AF} = (0.5, 0.5, 0.5)$ cannot arise from an inhomogeneous Nd distribution in the single crystal. In samples that consist of volume fractions with different stoichiometry, distinct ordering temperatures of the two magnetic phases are expected. Furthermore, in regions with higher Nd concentrations either \mathbf{Q}_{ICM} or $\mathbf{Q}_{CM} = (1/2, 0, 1/2)$ and $(0, 1/2, 1/2)$ should appear, as observed in the xT -phase diagram of $\text{Nd}_{1-x}\text{Ce}_x\text{CoIn}_5$ (see Fig. 5.6b).

The coexistence of two magnetic wave-vectors has been observed in other 115 compounds [248–250, 265]. While the case of $\text{CeCo}_y\text{Rh}_{1-y}\text{In}_5$ is still debated, a similar coexistence of two propagation vectors is reported for pure CeRhIn_5 . Here, it was shown that the commensurate phase weakens with improved sample quality, which suggests that the magnetic impurity phase arises from inner stress induced by crystal defects [265]. Although the origin of the additional wave-vector in some $\text{Nd}_{0.05}\text{Ce}_{0.95}\text{CoIn}_5$ single crystals remains elusive, the stabilization of \mathbf{Q}_{AF} may be related to a lower sample quality.

In consequence, the inelastic neutron scattering experiment on $\text{Nd}_{0.05}\text{Ce}_{0.95}\text{CoIn}_5$ was car-

^{‡‡}Background was measured at $T = 0.9 \text{ K} > T_N$ to exclude $\lambda/2$ contribution.

ried out solely on the well-characterized single crystal that has been used for all previous diffraction experiments (see chapter 5.1, 5.2, 5.3 and 5.4 and Ref. [28–30, 251]). The cold triple-axis spectrometer ThALES at the ILL is currently the only instrument, where such an experiment on a single crystal with mass $m = 64$ mg is possible. The sample was oriented in the scattering plane perpendicular to $[1 -1 0]$ and placed in an orange cryostat with ^3He insert. After a clean neutron wavelength was obtained from the velocity selector, the incoming neutron beam was diffracted from a vertical and horizontal focused silicon monochromator. The neutrons were scattered at the sample and then diffracted on the vertical and horizontal focused pyrolytic graphite analyzer that was fixed at $k_f = 1.45 \text{ \AA}^{-1}$. The remaining neutrons passed a radial collimator in front of the detector. The instrument was used in a W -configuration, as depicted in Fig. 3.2b.

The double-focussing option of the instrument ensures a high neutron flux in the detector, but reduces the spacial resolution drastically. The experimental setup did not allow to distinguish whether an excitation is attributed to $\mathbf{Q}_{SR} = (0.5, 0.5, 0.5)$ or \mathbf{Q}_{ICM} . We remind the reader that the incommensurate propagation vector of the spin resonance in CeCoIn_5 was resolved in a high-resolution setup, where the curvature of the monochromator and the analyzer was flat [201].

5.5.2 Observation of the Spin Resonance.

The crystal features static magnetic order at $\mathbf{Q}_{ICM} = (q, \pm q, 0.5)$ with $q \approx 0.45$ below $T_N = 0.8$ K inside the superconducting phase with $T_c = 2.3$ K [28, 251]. Its low-energy excitation spectrum, measured at \mathbf{Q}_{SR} and $T = 0.44, 1.2$ and 2.5 K, is displayed in Fig. 5.19a. The background was estimated at $T = 0.44$ K, because paramagnetic scattering above T_c may contribute to the detected signal. It was measured at reciprocal lattice positions that are sufficiently far from \mathbf{Q}_{SR} , and denotes the averaged signal detected at $(0.41, 0.41, 0.83)$ and $(0.54, 0.54, 0.08)$. The spectrum reveals a well-defined magnetic excitation at $\Delta E = 0.43(2)$ meV with similar intensity at $T = 0.44$ and 1.2 K and suppressed signal at $T = 2.5$ K.

Figure 5.19b displays rocking ω -scans that were measured at an energy transfer $\Delta E = 0.4$ meV for $T = 0.44, 1.2$ and 2.5 K. The scans are centered around \mathbf{Q}_{SR} and perform a rotation of the sample around the axis that is perpendicular to the scattering plane. The corresponding cut in reciprocal space is shown in the inset. We find an excitation that is peaked at $\omega = 42(1)^\circ$ and that vanishes above T_c . The center of the Gaussian fit corresponds to a reciprocal lattice position that is attributed either to \mathbf{Q}_{SR} or \mathbf{Q}_{ICM} .

The temperature dependence of the magnetic excitation was measured at \mathbf{Q}_{SR} for an energy transfer $\Delta E = 0.4$ meV (see right axis of Fig. 5.20). We find a saturated neutron intensity for $T < 1.2$ K that decreases with increasing temperatures. The signal is suppressed around $T_c = 1.8$ K. The background intensity (dashed line) was determined self-consistently from the data shown in Fig. 5.19b and 5.20. The solid line represents a BCS-fit as guideline to the eyes that reveals a similar behavior. The suppression of the magnetic excitation around T_c provides strong evidence that we found the spin resonance of 5% Nd doped CeCoIn_5 .

5.5.3 Decoupling of Magnetic Order and Antiferromagnetic Fluctuations.

The energy gap of the resonance, $\Delta E/k_B T_c = 2.8(1)$, in $\text{Nd}_{0.05}\text{Ce}_{0.95}\text{CoIn}_5$ scales with the one of CeCoIn_5 [92]. The normalized spectral weight derived from the data shown in

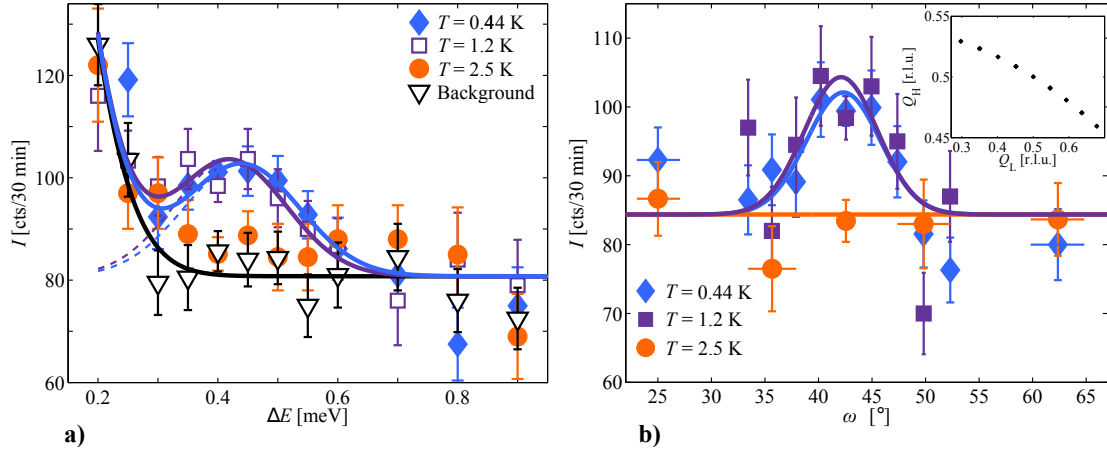


FIGURE 5.19: Spin Resonance of $\text{Nd}_{0.05}\text{Ce}_{0.95}\text{CoIn}_5$. **a)** Low-energy excitation spectrum measured at $Q_{SR} = (0.5, 0.5, 0.5)$ and $T = 0.44, 1.2$ and 2.5 K. **b)** Rocking ω -scan measured at an energy transfer $\Delta E = 0.4$ meV. Inset shows the corresponding cut along (Q_H, Q_H, Q_L) . Taken from [30].

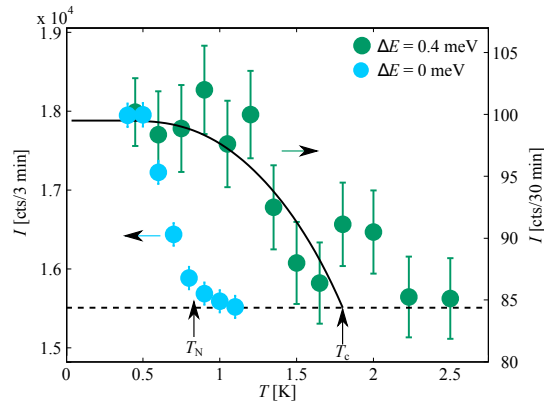


FIGURE 5.20: Decoupling of Static Order and Antiferromagnetic Fluctuations. Temperature dependence of the magnetic excitation at Q_{SR} and $\Delta E = 0.4$ meV in comparison with the temperature dependence of static magnetic order at Q_{ICM} and $\Delta E = 0$ meV (taken from Ref. [251]). The solid line is a BCS-fit as guideline to the eyes. The dashed line denotes the background that was obtained self-consistently from these data and the ones shown in Fig. 5.19b. Taken from [30].

Fig. 5.19 is consistent with the one of the pure compound that features a fluctuating moment $\langle \mu_{eff}^2 \rangle \approx 0.38\mu_B^2$. This supports the scenario that the observed excitation is related to the antiferromagnetic fluctuations leading to superconductivity and not to static magnetism. The temperature dependent intensity of the static magnetic order is displayed in Fig. 5.20 (data taken from Ref. [251]), where it is overplotted with the temperature evolution of the spin resonance. Their comparison shows that the resonance intensity is not affected by the SDW order below $T_N = 0.8$ K. In addition, the size of its gap remains unchanged for temperatures between $T = 0.44$ and 1.2 K. This suggests that the SDW order at zero field is decoupled from the spin resonance and, consequently, from superconductivity.

Static magnetic order breaks the rotational symmetry, which feeds back into the symmetry of the magnetic fluctuations. In an isotropic Heisenberg system, for instance, transverse fluctuations yield a Goldstone mode below the Néel temperature that restores the broken symmetry. In analogy, the spin resonance of an unconventional spin-singlet superconductor is expected to be isotropic above T_N , if spin rotational symmetry preserving magnetic interactions were considered. Antiferromagnetic order breaks this symmetry and forces the resonance into a state with anisotropic moment fluctuations. The magnetic structure of 5% Nd doped CeCoIn_5 shows a moment orientation along the tetragonal c -axis [30]. The spin resonance, however, remains unchanged at the antiferromagnetic phase boundary, suggesting that the magnetic excitation is polarized mainly along the SDW order. Such a fluctuating moment orientation is supported by recent neutron results on CeCoIn_5 that propose a spin resonance with Ising-like fluctuations [201].

We are not aware of a similar experimental or theoretical study on another CeCoIn_5 -substituted series that posses antiferromagnetic order in the superconducting phase. Nevertheless, the family of iron-based superconductors feature a spin resonance that is isotropic for overdoped and anisotropic for optimally and underdoped members [266]. The anisotropy manifests in a longitudinal mode that is substantially larger than the transverse ones and that is thought to arise from the proximity to static antiferromagnetic order [266, 267]. The effect of magnetic order on the spin resonance has been theoretically studied in this family via a three-band model in a random phase approximation [266]. The authors show that while the longitudinal component is resistant to antiferromagnetic order, the transverse modes soften into spin-waves at $T_N < T_c$. Although the Fermi surface topology and the superconducting gap symmetry is different in $\text{Nd}_{0.05}\text{Ce}_{0.95}\text{CoIn}_5$, we expect that the general phenomenology is similar. The spin resonance remains unchanged below T_N , which suggests the absence of moment fluctuations perpendicular to the magnetic moment orientation.

The robustness of longitudinal magnetic fluctuations is supported by polarized inelastic neutron scattering measurements on the iron pnictide $\text{Ba}(\text{Fe}_{0.955}\text{Co}_{0.045})_2\text{As}_2$ [268]. The material represents a case, where superconductivity emerges inside an antiferromagnetically ordered phase. Below T_c the resonance appears as an additional signal in the transverse low-energy excitation spectrum, while the fluctuations along the magnetic moment remain unchanged. This additional spectral weight perpendicular to the moment orientation is consistent with the reduction of the static magnetic moment below T_c [82, 268, 269]. The antithetic behavior of the spin fluctuations and magnetism is interpreted as a sign for competition between magnetic order and superconductivity in the material. This is in contrast to our results on $\text{Nd}_{0.05}\text{Ce}_{0.95}\text{CoIn}_5$, where no effect of the antiferromagnetic order on the superconducting spin resonance is found, but which may be assigned to an absent fluctuating transverse component.

The normalized gap energy, $\Delta E/k_B T_c \approx 3$, in doped and pure CeCoIn_5 is in line with the doping dependence of the quantum critical field, H^* , that features a constant $\mu_0 H^*/k_B T_c$ ratio (see chapter 5.3.4). Thus, a condensation of the resonance is expected at $\mu_0 H \approx 7.7$ T in $\text{Nd}_{0.05}\text{Ce}_{0.95}\text{CoIn}_5$ if the field dependence features a similar behavior as in CeCoIn_5 . This is in agreement with $\mu_0 H^* \approx 8$ T and suggests that the softening of longitudinal moment fluctuations leads to the emergence of the Q-phase, while the SDW-phase remains decoupled from the superconducting condensate.

5.5.4 Summary.

$\text{Nd}_{0.05}\text{Ce}_{0.95}\text{CoIn}_5$ reveals a collective magnetic excitation that emerges below the superconducting critical temperature, $T_c = 1.8$ K, at a wave-vector transfer in the vicinity of $\mathbf{Q}_{SR} = (0.5, 0.5, 0.5)$ [30]. This superconducting spin resonance saturates at $\Delta E/k_B T_c = 2.8(1)$ and features a spectral weight that is consistent with the resonance of the undoped compound. The key result of our study is that the excitation remains unaffected by the static magnetic order at $T_N = 0.8$ K. This suggests a decoupling of the SDW-phase from the magnetic fluctuations associated to superconductivity. The interpretation is consistent with the distinct switching behavior that is observed in the SDW- and Q-phase [29]. It postulates a modified magneto-superconducting coupling in the Q-phase of the material (see chapter 5.4). Based on polarized neutron scattering results on CeCoIn_5 and theoretical studies on the iron-pnictides we propose that the resonance of 5% Nd doped CeCoIn_5 consists of Ising-like fluctuations along the tetragonal c -axis [30].

Chapter 6

Conclusion and Outlook

The correlated ground states in the series $\text{Nd}_{1-x}\text{Ce}_x\text{CoIn}_5$ and, in particular, the interplay between magnetism and superconductivity for $x = 0.95$ have been studied by means of elastic and inelastic neutron scattering.

The series reveals a competition between the RKKY and Kondo interaction that yields an Ising-like magnetic structure along the tetragonal c -axis for members $x \leq 0.61$. In contrast, the structure is amplitude modulated for $x \geq 0.75$ and features a magnetic wave-vector that is rotated around the tetragonal axis. Here, the SDW order is populated along the superconducting $d_{x^2-y^2}$ -node and shows a competing coexistence between the two ground states. Thus, the substitution of Nd for Ce in CeCoIn_5 allows a controllable tuning of the Kondo coupling between the $4f$ -electrons and the conduction band.

Our results suggest that magnetic order arises from unscreened localized moments. In addition, we argue that the change in the magnetic structure is a consequence of the modified Fermi surface topology as the HF ground state is stabilized. The change in the magnetic symmetry appears at $x \approx 68\%$ and may be attributed to crystal field effects. This could be clarified by the investigation of the lowest crystal electric field multiplet for different members of the family. Such investigations have already provided insight in the underlying physics of $\text{CeCo}_y\text{Rh}_{1-y}\text{In}_5$ using x-ray absorption spectroscopy and could also play a key role in this series [196].

Nd substitution in CeCoIn_5 turns the HF ground state into a small Fermi surface for Nd concentrations larger than 50% [27]. It is, however, unclear whether the volume of the Fermi surface changes gradually or whether a quantum critical Kondo breakdown occurs in the proximity of $\text{Nd}_{0.5}\text{Ce}_{0.5}\text{CoIn}_5$. The Fermi surface of CeCoIn_5 has been investigated extensively over the recent years [54, 188–193]. Hybridized bands were observed mainly around the Γ -point and show a direct Kondo gap $v \approx 30$ meV (see Fig. 4.2) [54]. In contrast, the Fermi surface of the series $\text{Nd}_{1-x}\text{Ce}_x\text{CoIn}_5$ has not been studied yet and is unknown even for pure NdCoIn_5 . The doping dependent evolution of the Fermi surface topology can be studied by means of angle-resolved photoemission and de Haas-van Alphen spectroscopy. Such measurements could give access to modifications of the associated effective masses and the size of the Kondo gap as HF properties are suppressed. In addition, experimental results that are supported by theoretical band structure calculations may clarify how the hybridized $4f$ -bands are pushed below the Fermi surface as the Nd concentration is increased.

CeCoIn_5 reveals an anomalous behavior of the Grüneisen parameter that places the material close to a SDW quantum critical point [20]. In fact, magnetic order has been proposed recently

even in the undoped material [270]. De Haas-van Alphen measurements down to $T = 2$ mK recorded a magnetic signal below $T_N = 16$ mK. The doping dependence of the Grüneisen parameter may locate the quantum critical point and help to understand how magnetic order in $\text{Nd}_{1-x}\text{Ce}_x\text{CoIn}_5$ is correlated to the SDW-instability.

5% Nd doping on the Ce side of CeCoIn_5 reflects a small perturbation to the superconducting ground state of the pure compound. The material features a HT -phase diagram that, most likely, hosts a field-induced QPT at $\mu_0 H^* \approx 8$ T [28]. The instability separates two antiferromagnetic phases with an identical symmetry inside the superconducting condensate, preventing pure magnetic fluctuations at its origin. The magnetic order above H^* collapses in a first-order transition together with superconductivity. This provides evidence for a direct coupling between magnetic order and superconductivity in this high-field Q-phase, similar to the undoped compound.

The two spin-density modulation directions, $\mathbf{Q}_{1,2} = (q, \pm q, 0.5)$ with $q \approx 0.445$, reveal a distinct behavior in the low-field SDW-phase and the Q-phase, as the magnetic field is rotated from the $d_{x^2-y^2}$ -gap to its node [29]. In the SDW-phase a continuous change from equally populated domains for $\mathbf{H} \parallel [1\ 0\ 0]$ to a major difference in the domain population for $\mathbf{H} \parallel [1\ -1\ 0]$ is observed. In the latter configuration, the domain that is oriented along the magnetic field direction depopulates for increasing field strengths and is suppressed at $\mu_0 H_d \approx 3.5$ T. In contrast, the domain perpendicular to the magnetic field shows an antithetic behavior, such that a constant magnetic moment is maintained for $\mu_0 H \leq 4$ T. This behavior may be driven by spin-orbit interaction, which is predicted to be finite in multiband metals with a centrosymmetric crystal symmetry [220, 263]. This is in contrast to the hypersensitivity of the spin-density modulation direction in the Q-phase [29]. Here, a mono-domain state can be switched by small field rotations around the tetragonal a -axis. The difference in the domain selectivity of the SDW- and the Q-phase requires a modified magneto-superconducting coupling in the Q-phase. Based on a lowest-linear phenomenological Landau model that intertwines magnetism and superconductivity, the emergence of a spatially-modulated p -wave order parameter at the field-induced QPT is suggested.

A promising microscopic theory at the origin of the Q-phase is the softening of a magnetic excitation related to superconductivity at the field-induced quantum phase transition [147]. $\text{Nd}_{0.05}\text{Ce}_{0.95}\text{CoIn}_5$ reveals a collective magnetic excitation below $T_c = 1.8$ K at a wave-vector transfer close to $\mathbf{Q}_{1,2}$ [30]. The superconducting spin resonance saturates at $\Delta E/k_B T_c = 2.8(1)$ with a spectral weight that is similar to the resonance of the undoped compound. The excitation remains unaffected as static magnetic order develops at $T_N = 0.8$ K, suggesting a decoupling of the SDW-phase from the magnetic fluctuations associated to superconductivity. Based on previous experimental and theoretical studies, the resonance of 5% Nd doped CeCoIn_5 may consist of Ising-like fluctuations along the tetragonal c -axis. We postulate that the longitudinal mode splits under magnetic field and condenses into the ground state at H^* . This may create a novel superconducting ground state, in which spin-triplet Cooper pairs yield a spatially modulated p -wave superconducting order parameter that intertwines magnetic order with spin-singlet d -wave superconductivity.

The experimental investigation of the spin resonance under magnetic field allows to test this hypothesis. The enhanced background arising from incoherently scattered neutrons on the cryogenic magnet will, however, require large counting times and is not feasible for a measurement on one single crystal only. Prior to an experimental study where a multi-assembly

of coaligned single crystals is used, the emergence of the additional commensurate wave-vector $\mathbf{Q}_{AF} = (0.5, 0.5, 0.5)$ needs to be understood. It is noted that the coexistence of the magnetic wave-vectors $\mathbf{Q}_{1,2}$ and \mathbf{Q}_{AF} in some $\text{Nd}_{0.05}\text{Ce}_{0.95}\text{CoIn}_5$ crystals has been correlated recently to different resonances at the corresponding propagation vectors [271]. It has been argued that a sensitive balance between different energy scales may yield the condensation of either $\mathbf{Q}_{1,2}$ or \mathbf{Q}_{AF} at zero field that triggers the static magnetic order. Other possible scenarios concerning the two coexistent wave-vectors are related to the sample quality or static magnetism at \mathbf{Q}_{AF} for $\text{Nd}_{1-x}\text{Ce}_x\text{CoIn}_5$ with $0.95 < x < 1$. Further studies on experimental realizations with different Nd concentrations are needed to shed light on this open question.

The observation of the Q-phase in 5% Nd doped CeCoIn_5 enables to test several theories that have been proposed for CeCoIn_5 . It is thought that Pauli paramagnetic effects are crucial for the existence of the Q-phase as revealed, for instance, by its suppression upon rotating the magnetic field 17° towards the tetragonal c -axis [218]. At this angle the superconducting upper critical field decreases below the Pauli limiting field, $\mu_0 H^p = 9.8$ T, that coincides with the Q-phase boundary [88, 188]. Upon 5% Nd doping the field-induced QPT is reduced to $\mu_0 H^* = 8.0(2)$ T, while H_{c2} is suppressed by about 5%. The upper critical field of $\text{Nd}_{0.05}\text{Ce}_{0.95}\text{CoIn}_5$ intersects with H^* at an out-of-plane angle of 21° , below which the Q-phase is expected to be stable.

Microscopic evidence for Pauli limited superconductivity has been found via small-angle neutron scattering in the mixed state of CeCoIn_5 [209, 210]. The measurements show an increasing scattering cross section with magnetic fields that are oriented along the basal plane and perpendicular to it (see Fig. 4.3c). Moreover, the vortex lattice geometry features a cascade of phase transitions for an increasing field applied along the tetragonal c -axis (see Fig. 4.3d) [206]. Most importantly, it reveals a reentrant triangular structure below the upper critical field that is thought to arise from paramagnetic or antiferromagnetic effects. The comparison of the vortex lattice phase diagram in 5% Nd doped CeCoIn_5 with the pure material could test some of these conclusions.

A 5% Nd substitution for Ce in CeCoIn_5 yields a reduction of the field-induced QPT by about 20%, maintaining the ratio $\mu_0 H^*/k_B T_c$ [28, 88]. In addition, it weakens the hybridized bands, which results in a decreasing orbital limiting field $H_{c2}^{orb} \propto m^{*2}$. Thus, the Pauli limiting properties may be lost at a certain Nd concentration $0.78 < x_c < 0.95$, for which the Q-phase is expected to be suppressed. The experimental investigation of the HT -phase diagram for $\text{Nd}_{1-x}\text{Ce}_x\text{CoIn}_5$ with $x \neq 0.95$ will provide insight in the energy scale that is required to stabilize the Q-phase. Moreover, it will clarify whether the SDW- and the Q-phase can be separated for $x > 0.95$.

Thermal conductivity measurements in the Q-phase of CeCoIn_5 reveal reduced quasiparticle excitations perpendicular to the populated spin-density modulation direction (see Fig. 4.5) [219]. These results have been interpreted as evidence for the existence of a supplementary superconducting p -wave order parameter in the Q-phase that features a maximal gap that is about 20% of the d -wave order parameter. A similar measurement in the Q- and SDW-phase of $\text{Nd}_{0.05}\text{Ce}_{0.95}\text{CoIn}_5$ is required to test our interpretation of a PDW of p -wave type as a primary order parameter of the Q-phase.

The enhanced spin susceptibility of the proposed spin-triplet component in the Q-phase and the quantum critical fluctuations at the field-induced QPT may be observable with muon spin rotation (μSR). Such an experiment is currently not possible for CeCoIn_5 . The maximal

field that can be achieved on a low-temperature μ SR spectrometer at the Paul Scherrer Institut is $\mu_0 H_{max} = 9.5$ T, which is below the Q-phase boundary [272]. In $\text{Nd}_{0.05}\text{Ce}_{0.95}\text{CoIn}_5$ the QPT is reduced to $\mu_0 H^* \approx 8$ T and, thus, accessible on the instrument.

In fact, we do not have direct evidence for quantum fluctuations at the field-induced QPT, but our results suggest that they are not purely magnetic [28, 29]. The role of such fluctuations could be studied with a sub- μeV resolution using neutron spin echo spectroscopy [273].

The SDW-phase of $\text{Nd}_{0.05}\text{Ce}_{0.95}\text{CoIn}_5$ is suppressed at a magnetic field of $\mu_0 H^* \approx 8$ T when the magnetic field is applied in the tetragonal basal plane. The field and temperature dependence of the magnetic order for $\mathbf{H} \parallel [0\ 0\ 1]$ has, however, not been measured and is required to complete the phase diagram. Particularly interesting is the open question of a supplementary phase below the upper critical field that has been suggested in CeCoIn_5 by means of heat capacity [22].

We suggest that spin-orbit interactions drives the switching behavior in the SDW-phase of 5% Nd doped CeCoIn_5 . A similar measurement above and below the superconducting transition temperature of $\text{Nd}_{0.17}\text{Ce}_{0.83}\text{CoIn}_5$ or in the correlated metal $\text{Nd}_{0.25}\text{Ce}_{0.75}\text{CoIn}_5$ would clarify the role of superconductivity in this behavior. In particular, it may shed light on the question whether all centrosymmetric multiband materials feature a spin-orbit interaction that triggers a field dependent redistribution of magnetic domains in incommensurate antiferromagnetic structures.

A multitude of research groups have started to investigate the microscopic properties of the series $\text{Nd}_{1-x}\text{Ce}_x\text{CoIn}_5$ and related 115 compounds [27–30, 251, 255–257, 260]. Rare-earth elements different than Nd may lead to a similar impact as in the investigated series. Most prominent is the series $\text{Gd}_{1-x}\text{Ce}_x\text{CoIn}_5$ that has been synthesized recently and that also shows a coexistence of magnetic order and superconductivity at zero field [257]. It is likely that the Q-phase is found for low Gd concentrations on the Ce-site of CeCoIn_5 .

The tuning of the ground state properties with pressure may lead to further insight in the underlying physics of the Q-phase. The phase is stable up to at least $p = 1.4$ GPa under hydrostatic pressure [227, 228]. The external parameter has, however, an anomalous impact on the tetragonal a - and c -axis and the pressure cell enhances the background in a neutron diffraction experiment [226]. The application of uniaxial pressure along the a -axis would allow a controlled tuning of the ground state and is feasible for neutron diffraction. This tuning parameter is an alternative way to break the tetragonal crystal symmetry and may affect the Q-phase. The reduction of the tetragonal symmetry to an orthorhombic space group is crucial, for instance, in the interplay of magnetism and superconductivity in the iron-pnictides [82].

One step towards the microscopic description of the Q-phase may be found in the switching behavior of the spin-resonance. High-resolution inelastic neutron scattering has shown that the resonance features an incommensurate wave-vector similar to the one of static magnetic order in the Q-phase [201]. If the resonance acts as a dynamic predecessor of the Q-phase, it should show a similar behavior in a magnetic field that is rotated in the tetragonal basal plane. Inelastic neutron scattering on CeCoIn_5 under rotating magnetic field could be performed with a piezoelectric sample rotator using a time of flight spectrometer [274].

Bibliography

- [1] S. Sachdev. *Quantum Phase Transitions*. Cambridge University Press, 2011.
- [2] P. Coleman, and A. J. Schofield. Quantum criticality. *Nature* **422**, 226 (2005).
- [3] D. E. Sands. *Introduction to Crystallography*. Dover edition, 1993.
- [4] G. Grüner. The dynamics of spin-density waves. *Rev. Mod. Phys.* **66**, 1 (1994).
- [5] S. Blundel. *Magnetism in Condensed Matter*. Oxford University Press, 2001.
- [6] P. Monthoux, D. Pines, and G. G. Lonzarich. Superconductivity without phonons. *Nature* **450**, 1177 (2007).
- [7] M. Fiebig, T. Lottermoser, D. Meier, and M. Trassin. The evolution of multiferroics. *Nat. Rev. Mat.* **1**, 16046 (2016).
- [8] H. K. Onnes. *Commun. Phys. Lab. Univ. Leiden* **12**, 120 (1911).
- [9] A. Schilling, M. Cantoni, J. D. Guo, and H. R. Ott. Superconductivity above 130 K in the Hg-Ba-Ca-Cu-O system. *Nature* **363**, 56 (1993).
- [10] M. R. Norman. The Challenge of Unconventional Superconductivity. *Science* **332**, 196 (2011).
- [11] N. D. Mathur, F. M. Grosche, S. R. Julian, I. R. Walker, D. M. Freye, R. K. W. Haselwimmer, and G. G. Lonzarich. Magnetically mediated superconductivity in heavy fermion compounds. *Nature* **394**, 39 (1998).
- [12] P. Gegenwart, Q. Si, and F. Steglich. Quantum criticality in heavy fermion metals. *Nat. Phys.* **4**, 186 (2008).
- [13] Q. Si, and F. Steglich. Heavy Fermions and Quantum Phase Transitions. *Science* **329**, 1161 (2010).
- [14] A. Furrer, J. Mesot, and Th. Strässle. *Neutron Scattering in Condensed Matter Physics*. World Scientific Publishing, 2009.
- [15] G. L. Squires. *Introduction to the Theory of Thermal Neutron Scattering*. Dover Publications, 1996.
- [16] G. Shirane, S. M. Shapiro, and J. M. Tranquada. *Neutron Scattering with a Triple-Axis Spectrometer*. Cambridge University Press, 2002.
- [17] C. Petrovic, P. G. Pagliuso, M. F. Hundley, R. Movshovich, J. L. Sarrao, J. D. Thompson, Z. Fisk, and P. Monthoux. Heavy-fermion superconductivity in CeCoIn₅ at 2.3 K. *J. Phys.: Condens. Matter* **13**, L337 (2001).
- [18] M. P. Allan, F. Masee, D. K. Morr, J. Van Dyke, A. W. Rost, A. P. Mackenzie, C. Petrovic, and J. C. Davis. Imaging Cooper pairing of heavy fermions in CeCoIn₅. *Nat. Phys.* **9**, 468 (2013).

- [19] B. B. Zhou, S. Misra, E. H. da Silva Neto, P. Aynajian, R. E. Baumbach, J. D. Thompson, E. D. Bauer, and A. Yazdani. Visualizing nodal heavy fermion superconductivity in CeCoIn₅. *Nat. Phys.* **9**, 474 (2013).
- [20] Y. Tokiwa, E. D. Bauer, and P. Gegenwart. Zero-Field Quantum Critical Point in CeCoIn₅. *Phys. Rev. Lett.* **111**, 107003 (2013).
- [21] A. Bianchi, R. Movshovich, C. Capan, P. G. Pagliuso, and J. L. Sarrao. Possible Fulde-Ferrell-Larkin-Ovchinnikov Superconducting State in CeCoIn₅. *Phys. Rev. Lett.* **91**, 187004 (2003).
- [22] A. Bianchi, R. Movshovich, I. Vekhter, P. G. Pagliuso, and J. L. Sarrao. Avoided Antiferromagnetic Order and Quantum Critical Point in CeCoIn₅. *Phys. Rev. Lett.* **91**, 257001 (2003).
- [23] M. Kenzelmann, Th. Strässle, C. Niedermayer, M. Sigrist, B. Padmanabhan, M. Zolliker, A. D. Bianchi, R. Movshovich, E. D. Vauer, J. L. Sarrao, and J. D. Thompson. Coupled Superconducting and Magnetic Order in CeCoIn₅. *Science* **321**, 1652 (2008).
- [24] S. Gerber. *Interplay of Unconventional Superconductivity and Magnetism in CeCoIn₅*. PhD thesis, ETH Zürich and Paul Scherrer Insitut, 2013.
- [25] M. Kenzelmann. Exotic magnetic states in Pauli-limited superconductors. *Rep. Prog. Phys.* **80**, 034501 (2017).
- [26] Y. Tokiwa, R. Movshovich, F. Ronning, E. D. Bauer, A. D. Bianchi, Z. Fisk, and J. D. Thompson. Anomalous effect of doping on the superconducting state of CeCoIn₅ in high magnetic fields. *Phys. Rev. B* **82**, 220502(R) (2010).
- [27] R. Hu, Y. Lee, J. Hudis, V. F. Mitrovic, and C. Petrovic. Composition and field-tuned magnetism and superconductivity in Nd_{1-x}Ce_xCoIn₅. *Phys. Rev. B* **77**, 165129 (2008).
- [28] D. G. Mazzone, S. Raymond, J. L. Gavilano, E. Ressouche, C. Niedermayer, J. O. Birk, B. Ouladdiaf, G. Bastien, G. Knebel, D. Aoki, G. Lapertot, and M. Kenzelmann. Field-induced magnetic instability within a superconducting condensate *Sci. Adv.* **3**, e1602055 (2017).
- [29] D. G. Mazzone, R. Yadav, M. Bartkowiak, J. L. Gavilano, S. Raymond, E. Ressouche, G. Lapertot, and M. Kenzelmann. Distinct domain switching in Nd_{0.05}Ce_{0.95}CoIn₅ at low and high fields. *Sci. Rep.* **8**, 1295 (2018).
- [30] D. G. Mazzone, S. Raymond, J. L. Gavilano, P. Steffens, A. Schneidewind, G. Lapertot, and M. Kenzelmann. Spin Resonance and Magnetic Order in an Unconventional Superconductor. *Phys. Rev. Lett.* **119**, 187002 (2017).
- [31] F. Bloch. Über die Quantenmechanik der Elektronen in Kristallgittern. *Z Phys.* **52**, 555 (1928).
- [32] E. Dagotto. Complexity in Strongly Correlated Electron Systems. *Science* **309**, 257 (2005).
- [33] G. Grüner. The dynamics of charge-density waves. *Rev. Mod. Phys.* **60**, 1129 (1988).
- [34] P. W. Anderson. Absence of Diffusion in Certain Random Lattices. *Phys. Rev.* **109**, 1492 (1958).
- [35] D. J. P. Gingras. Observing monopoles in a magnetic analogue of ice. *Science* **326**, 411 (2009).
- [36] V. Zapf, M. Jaime, and C. D. Bastia. Bose-Einstein condensation in quantum magnets. *Rev. Mod. Phys.* **86**, 563 (2014).
- [37] D. Hsieh, D. Qian, L. Wray, Y. Cia, Y. S. Hor, R. J. Cava, and M. Z. Hasan. A topological Dirac insulator in a quantum spin Hall phase. *Nature* **452**, 970 (2008).
- [38] M. Dzero, J. Xia, V. Falitski, and P. Coleman. Topological Kondo Insulators. *Annu. Rev. of Conden. Ma. P.* **7**, 249 (2016).

- [39] T. Park, F. Ronning, H. Q. Yuan, M. B. Salamon, R. Movshovich, L. Sarrao, and J. D. Thompson. Hidden magnetism and quantum criticality in the heavy fermion superconductor CeRhIn₅. *Nature* **440**, 65 (2006).
- [40] H. Q. Yuan, F. M. Grosche, M. Deppe, C. Geibel, G. Sparn, and F. Steglich. Observation of Two Distinct Superconducting Phases in CeCu₂Si₂. *Science* **302**, 2104 (2003).
- [41] N. Dorion-Leyraud, I. R. Walker, L. Taillefer, M. Steiner, S. R. Julian, and G. G. Lonzarich. Fermi-liquid breakdown in the paramagnetic phase of a pure metal. *Nature* **425**, 595 (2003).
- [42] H. A. Kramers. Théorie générale de la rotation paramagnétique dans les cristaux. *Proc. Amsterdam Acad.* **33**, 959 (1930).
- [43] P. Allenspach, and U. Gasser. Rare earth magnetism in high-temperature and borocarbide superconductors. *J. Alloys Compd.* **311**, 1 (2000).
- [44] M. A. Rudermann, and C. Kittel. Indirect Exchange Coupling of Nuclear Magnetic Moments by Conduction Electrons. *Phys. Rev.* **96**, 99 (1954).
- [45] T. Kasuya. A Theory of Metallic Ferro- and Antiferromagnetism on Zener's Model. *Prog. Theor. Phys.* **16**, 45 (1956).
- [46] K. Yosida. Magnetic Properties of Cu-Mn Alloys. *Phys. Rev.* **106**, 893 (1957).
- [47] M. Sigrist. *Solid State Theory*. Lecture, ETH Zürich, 2012.
- [48] J. Kondo. Resistance Minimum in Dilute Magnetic Alloys. *Prog. Theor. Phys.* **32**, 37 (1964).
- [49] P. Coleman. *Heavy Fermions and the Kondo Lattice: a 21st Century Perspective*. arXiv:1509.05769 (2015).
- [50] P. Aynajian, E. H. da Silva Neto, A. Gyenis, R. E. Baumbach, J. D. Thompson, Z. Fisk, E. D. Bauer, and A. Yazdani. Visualizing heavy fermions emerging in a quantum critical Kondo lattice. *Nature* **484**, 201 (2012).
- [51] C. Lacroix. Coherence effects in the Kondo lattice. *J. Magn. Magn. Mater.* **60**, 2 (1986).
- [52] N. Xu, C. E. Matt, E. Pomjakushina, J. H. Dil, G. Landolt, J. -Z. Ma, X. Shi, R. S. Dhaka, N. C. Plumb, M. Radovic, V. N. Strocov, T. K. Kim, M. Hoesch, K. Conder, J. Mesot, H. Ding, and M. Shi. *Surface vs bulk electronic structures of a moderately correlated topological insulator YbB₆ revealed by ARPES*. arXiv:1405.0165 (2014).
- [53] N. Xu, P. Biswas, J. H. Dil, R. S. Dhaka, G. Landolt, S. Muff, C. E. Matt, X. Shi, N. C. Plumb, M. Radovic, E. Pomjakushina, K. Conder, A. Amato, S. V. Borisenko, R. Yu, H. -M. Weng, Z. Fang, X. Dai, J. Mesot, H. Ding, and M. Shi. Direct observation of the spin texture in SmB₆ as evidence of the topological insulator. *Nat. Commun.* **5**, 4566 (2014).
- [54] Q. Y. Chen, D. F. Xu, X. H. Niu, J. Jiang, R. Peng, H. C. Xu, C. H. P. Wen, Z. F. Ding, K. Huang, L. Shu, Y. J. Zhang, H. Lee, V. N. Strocov, M. Shi, F. Bisti, T. Schmitt, Y. B. Hunag, P. Dudin, X. C. Lai, S. Kirchner, H. Q. Yuan, and D. L. Fen. Direct observation of how the heavy fermion state develops in CeCoIn₅. *Phys. Rev. B* **96**, 045107 (2017).
- [55] K. Andres, J.E. Graebner, and H.R. Ott. 4f-virtual-bound-state formation in CeAl₃ at low temperatures. *Phys. Rev. Lett.* **35**, 1779 (1975).
- [56] C. Ye, W. Zongfa, M. Smidman, L. Xin, and Y. Huiqi. High-pressure studies on heavy fermion systems. *Chinese Physics B* **25**, 077401 (2016).
- [57] Q. Si, S. Rabello, K. Ingersent, and J. L. Smith. Locally critical quantum phase transitions in strongly correlated metals. *Nature* **413**, 804 (2001).

- [58] Q. Si, S. Rabello, K. Ingersent, and J. L. Smith. Local fluctuations in quantum critical metals. *Phys. Rev. B* **68**, 115103 (2003).
- [59] S. Doniach. The Kondo lattice and weak antiferromagnetism. *Physica B+C* **91**, 231 (1977).
- [60] S. -K. Ma. *Modern Theory of Critical Phenomena*. Addison-Wesley, Redwood City, Ca, 1976.
- [61] K. G. Wilson and J. Kogut. The renormalization group and the ϵ expansion. *Phys. Rep.* **12**, 75 (1974).
- [62] J. A. Hertz. Quantum critical phenomena. *Phys. Rev. B* **14**, 1165 (1976).
- [63] A. J. Millis. Effect of a nonzero temperature on quantum critical points in itinerant fermion systems. *Phys. Rev. B* **48**, 7183 (1993).
- [64] P. Coleman, C. Pépin, Q. Si, and R. Ramazashvili. How do Fermi liquids get heavy and die? *J. Phys.: Condens. Matter* **13**, R723 (2001).
- [65] T. Senthil, M. Vojta, and S. Sachdev. Weak magnetism and non-Fermi liquids near heavy-fermion critical points. *Phys. Rev. B* **69**, 035111 (2004).
- [66] S. Burdin, D. R. Grempel, and A. Georges. Heavy-fermion and spin-liquid behavior in a Kondo lattice with magnetic frustration. *Phys. Rev. B* **66**, 045111 (2002).
- [67] S. Friedemann, T. Westerkamp, M. Brando, N. Oeschler, S. Wirth, P. Gegenwart, C. Krellner, C. Geibel, and F. Steglich. Detaching the antiferromagnetic quantum critical point from the Fermi-surface reconstruction in YbRh_2Si_2 . *Nat. Phys.* **5**, 465 (2009).
- [68] A. Schröder, G. Aeppli, R. Coldea, M. Adams, O. Stockert, H.v. Löhneysen, E. Bucher, R. Ramazashvili, and P. Coleman. Magnetic Fluctuations at a Field-Induced Quantum Phase Transition. *Phys. Rev. Lett.* **99**, 237203 (2007).
- [69] O. Stockert, M. Enderle, and H.v. Löhneysen. Onset of antiferromagnetism in heavy-fermion metals. *Nature* **407**, 351 (2000).
- [70] H. Shishido, R. Settai, H. Harima, and Y. Ōnuki. A drastic change of the Fermi surface at a critical pressure in CeRhIn_5 : dH-vA study under pressure. *J. Phys. Soc. Jpn.* **74**, 1103 (2005).
- [71] S. Nakatsuji, D. Pines, and Z. Fisk. Two fluid description of the Kondo lattice. *Rev. Phys. Lett.* **92**, 016401 (2005).
- [72] Y. -F. Yang, Z. Fisk, H.-O. Lee, J. D. Thompson, and D. Pines. Scaling the Kondo lattice. *Nature* **454**, 611 (2008).
- [73] Y. -F. Yang, and D. Pines. Emergence of superconductivity in heavy electron materials. *P. Natl. Acad. Sci. USA* **111**, 18178 (2014).
- [74] Y. -F. Yang. Two-fluid model for heavy electron physics. *Rep. Prog. Phys.* **79**, 074501 (2016).
- [75] F. Steglich, J. Aart, C. D. Bredl, W. Lieke, D. Meschede, W. Franz, and H. Schäfer. Superconductivity in the presence of strong Pauli paramagnetism: CeCu_2Si_2 . *Phys. Rev. Lett.* **43**, 1892 (1979).
- [76] H. Fröhlich. Theory of the Superconducting State. I. The Ground State at the Absolute Zero of Temperature. *Phys. Rev.* **79**, 845 (1950).
- [77] L. N. Cooper. Bound Electron Pairs in a Degenerate Fermi Gas. *Phys. Rev.* **104**, 1189 (1956).
- [78] J. Bardeen, L. Cooper, and J. Schrieffer. Theory of Superconductivity. *Phys. Rev.* **108**, 1175 (1957).

- [79] A. J. Leggett. A Theoretical Description of the New Phases of Liquid ^3He . *Rev. Mod. Phys.* **47**, 331 (1975).
- [80] A. T. Holmes, D. Jaccard, and M. Miyake. Signatures of valence fluctuations in CeCu_2Si_2 under high pressure. *Phys. Rev. B* **69**, 024508 (2004).
- [81] M. Hashimoto, I. M. Vishik, R.-H. He, T. P. Devereaux, and Z. -X Shen. Energy gaps in high-transition-temperature cuprate superconductors. *Nat. Phys.* **10**, 483 (2014).
- [82] P. Dai. Antiferromagnetic order and spin dynamics in iron-based superconductors. *Rev. Mod. Phys.* **87**, 855 (2015).
- [83] D. Jérôme, A. Mazaud, M. Ribault and K. Bechgaard. Superconductivity in a synthetic organic conductor $(\text{TMTSF})_2\text{PF}_6$. *J. Phys. Lett.* **41**, L95 (1980).
- [84] J. F. Annett. *Superconductivity, Superfluids and Condensates*. Oxford University Press, 2005.
- [85] M. Tinkham. *Introduction to Superconductivity*. Dover Publications, Inc., 2008.
- [86] R. Joynt and L. Taillefer. The superconducting phases of UPt_3 . *Rev. Mod. Phys.* **74**, 235 (2002).
- [87] G. R. Stewart. Unconventional Superconductivity. *Adv. Phys.* **66**, 75 (2017).
- [88] S. Gerber, M. Bartkowiak, J. L. Gavilano, E. Ressouche, N. Egetenmeyer, C. Niedermayer, A. D. Bianchi, R. Movshovich, E. D. Bauer, J. D. Thompson, and M. Kenzelmann. Switching of magnetic domains reveals evidence for spatially inhomogeneous superconductivity. *Nat. Phys.* **10**, 126 (2014).
- [89] J. H. Pixley, L. Deng, K. Ingersent, and Q. Si. Pairing correlations near a Kondo-destruction quantum critical point. *Phys. Rev. B* **91**, 201109(R) (2015).
- [90] A. D. Christianson, E. A. Goremychkin, R. Osborn, S. Rosenkranz, M. D. Lumsden, C. D. Malliakas, I. S. Todorov, H. Claus, D. Y. Chung, M. G. Kanatzidis, R. I. Bewley, and T. Guidi. Unconventional superconductivity in $\text{Ba}_{0.6}\text{K}_{0.4}\text{Fe}_2\text{As}_2$ from inelastic neutron scattering. *Nature* **456**, 930 (2008).
- [91] T. Moriya, and K. Ueda. Spin fluctuations and high temperature superconductivity. *Adv. Phys.* **49**, 555 (2000).
- [92] C. Stock, C. Broholm, J. Hudis, H. J. Kang, and C. Petrovic. Spin Resonance in the d-Wave Superconductor CeCoIn_5 . *Phys. Rev. Lett.* **100**, 087001 (2008).
- [93] G. Yu, Y. Li, E. M. Motoyama, and M. Greven. A universal relationship between magnetic resonance and superconducting gap in unconventional superconductors. *Nat. Phys.* **5**, 873 (2009).
- [94] I. Eremin, G. Zwicknagl, P. Thalmeier, and P. Fulde. Feedback Spin Resonance in Superconducting CeCu_2Si_2 and CeCoIn_5 . *Phys. Rev. Lett.* **101**, 187001 (2008).
- [95] P. Thalmeier, I. Eremin, A. Akbari, and P. Fulde. Feedback Spin Exciton Formation in Unconventional Superconductors. *J. Supercond. Nov. Magn.* **23**, 729 (2010).
- [96] M. Eschrig. The effect of collective spin-1 excitations on electronic spectra in high-Tc superconductors. *Adv. Phys.* **55**, 47 (2006).
- [97] V. Simonet, B. Canals, J. Robert, S. Petit, and H. Mutka. *Neutrons et Magnétisme*. Les Ulis: EDP sciences, 2014.
- [98] D. K. Morr, and D. Pines. The Resonance Peak in Cuprate Superconductors. *Phys. Rev. Lett.* **81**, 1086 (1998).
- [99] A. V. Chubokov, and L. P. Gor'kov. Spin resonance in three-dimensional superconductors: the case of CeCoIn_5 . *Phys. Rev. Lett.* **101**, 147004 (2008).

- [100] Y. Song, J. Van Dyke, I. K. Lum, B. D. White, S. Jang, D. Yazici, L. Shu, A. Schneidewind, P. Čermak, Y. Qiu, M.B. Maple, D. K. Morr, and P. Dai. Robust upward dispersion of the neutron spin resonance in the heavy fermion superconductor $\text{Ce}_{1-x}\text{Yb}_x\text{CoIn}_5$. *Nat. Commun.* **7**, 12774 (2016).
- [101] L. Taillefer. Scattering and Pairing in Cuprate Superconductors. *Annu. Rev. Condens. Ma. P.* **1**, 51 (2010).
- [102] P. W. Anderson. Heavy-electron superconductors, spin fluctuations, and triplet pairing. *Phys. Rev. B* **30**, 1549 (1984).
- [103] C. M. Varma. Phenomenological Aspects of Heavy Fermions. *Phys. Rev. Lett.* **55**, 2723 (1985).
- [104] K. Miyake, S. Schmitt-Rink, and C. M. Varma. Spin-fluctuation-mediated even-parity pairing in heavy-fermion superconductors. *Phys. Rev. B* **34**, 6554(R) (1986).
- [105] D. J. Scalapino, E. Loh, Jr., and J. E. Hirsch. d -wave pairing near a spin-density-wave instability. *Phys. Rev. B* **34**, 8190(R) (1986).
- [106] M. R. Norman. Hund's rule theory for heavy fermion superconductors. *Phys. Rev. Lett.* **72**, 2077 (1994).
- [107] D. J. Scalapino. The case for $d_{x^2-y^2}$ pairing in the cuprate superconductors. *Phys. Rep.* **250**, 320 (1995).
- [108] P. W. Anderson. Is There Glue in Cuprate Superconductors? *Science* **316**, 1705 (2007).
- [109] K. Hattory. Meta-Orbital Transition in Heavy-Fermion Systems: Analysis by Dynamical Mean Field Theory and Self-Consistent Renormalization Theory of Orbital Fluctuations. *J. Phys. Soc. Jpn.* **79**, 114717 (2010).
- [110] L. V. Pourovskii, P. Hansmann, M. Ferrero, and A. Georges. Theoretical Prediction and Spectroscopic Fingerprints of an Orbital Transition in CeCu_2Si_2 . *Phys. Rev. Lett.* **112**, 106407 (2014).
- [111] V. L. Ginzburg. Ferromagnetic superconductors. *Zh. Eksp. Teor. Fiz.* **31**, 202 (1956).
- [112] B. T. Matthias, H. Suhl, and E. Corenzwit. Spin Exchange in Superconductors. *Phys. Rev. Lett.* **1**, 92 (1958).
- [113] W. A. Fertig, D. C. Johnston, L. E. DeLong, R. W. Mc. Callum, M. B. Maple, and B. T. Matthias. Destruction of Superconductivity at the Onset of Long-Range Magnetic Order in the Compound ErRh_4B_4 . *Phys. Rev. Lett.* **38**, 987 (1977).
- [114] M. Ishikawa, and Ø. Fisher. Destruction of Superconductivity by Magnetic-ordering in $\text{Ho}_{1.2}\text{Mo}_6\text{S}_8$. *Solid State Commun.* **23**, 37 (1977).
- [115] H. Eisaki, H. Takagi, R. J. Cava, B. Batlogg, J. J. Krajewski, W. F. Peck, Jr., K. Mizuhashi, J. O. Lee, and S. Uchida. Competition between magnetism and superconductivity in rare-earth nickel boride carbides. *Phys. Rev. B* **50**, 647(R) (1994).
- [116] R. J. Cava, H. Takagi, H. W. Zandbergen, J. J. Krajewski, W. F. Peck Jr., T. Sigrüst, B. Batlogg, R. B. Van Dover, R. J. Felder, K. Mizuhashi, J. O. Lee, O. Eisaki, and S. Uchida. Superconductivity in the quaternary intermetallic compounds $\text{LnNi}_2\text{B}_2\text{C}$. *Nature* **367**, 252 (1994).
- [117] R. J. Cava, H. Takagi, B. Batlogg, H. N. Zandbergen, J. J. Krajewski, W. F. Peck Jr., R. B. Van Dover, R. J. Felder, T. Sigrüst, K. Mizuhashi, J. O. Lee, O. Eisaki, and S. Uchida. Superconductivity at 23 K in yttrium palladium boride carbide. *Nature* **367**, 146 (1994).
- [118] L. C. Gupta. Superconductivity and magnetism and their interplay in quaternary borocarbides $\text{RNi}_2\text{B}_2\text{C}$. *Adv. Phys.* **55**, 691 (2006).

- [119] M. B. Maple. Three decades of progress on superconductivity and magnetism in novel materials. *Physica C* **341**, 47 (2000).
- [120] W. Baltensperger, and S. Strässler. Superconductivity in antiferromagnets. *Phys. Kondens. Materie* **1**, 20 (1963).
- [121] T. Matsubara, and A. Kontani. *Superconductivity in Magnetic and Exotic Materials*. Sixth Taniguchi International Symposium, Springer-Verlag, Berlin/Heidelberg/New York/Tokyo, 1984.
- [122] C. T. Wolowiec, B. D. White, and M. B. Maple. Conventional magnetic superconductors. *Physica C* **513**, 113 (2015).
- [123] K. H. Müller, and V. N. Narozhnyi. Interaction of superconductivity and magnetism in borocarbide superconductors. *Rep. Prog. Phys.* **64**, 943 (2001).
- [124] O. Stockert, J. Arndt, E. Faulhaber, C. Geibel, H. S. Jeevan, S. Kirchner, M. Loewenhaupt, K. Schmalzl, W. Schmidt, Q. Si, F. Steglich. Magnetically driven superconductivity in CeCu₂Si₂. *Nat. Phys.* **7**, 119 (2011).
- [125] W. Assmus, M. Herrmann, U. Rauschwalbe, S. Riegel, W. Lieke, H. Spille, S. Horn, G. Weber, F. Steglich, and G. Cordier. Superconductivity in CeCu₂Si₂ Single Crystals. *Phys. Rev. Lett.* **52**, 469 (1984).
- [126] O. Stockert, D. Andreica, A. Amato, H. S. Jeevan, C. Geibel, and F. Steglich. Magnetic order and superconductivity in single-crystalline CeCu₂Si₂. *Physica B* **67**, 167 (2006).
- [127] O. Stockert, E. Faulhaber, G. Zwicknagl, N. Stässer, H. S. Jeevan, M. Deppe, R. Borth, R. Küchler, M. Loewenhaupt, C. Geibel, and F. Steglich. Nature of the A phase in CeCu₂Si₂. *Phys. Rev. Lett.* **92**, 136401 (2004).
- [128] H. A. Vieyra, N. Oeschler, S. Seiro, H. S. Jeevan, C. Geibel, F. Steglich. Determination of gap symmetry from angle-dependent Hc₂ measurements on CeCu₂Si₂. *Phys. Rev. Lett.* **106**, 207001 (2011).
- [129] H. Ikeda, M. T. Suzuki, R. Arita. Emergent loop-nodal s±-wave superconductivity in CeCu₂Si₂: similarities to the iron-based superconductors. *Phys. Rev. Lett.* **114**, 147003 (2015).
- [130] H. Yamaoka, Y. Ikeda, I. Jarrige, N. Tsujii, Y. Zekko, Y. Yamamoto, J. Mizuki, J.-F. Lin, N. Hiraoka, H. Ishii, K.-D. Tsuei, T. C. Kobayashi, F. Honda, and Y. Ōnuki. Role of Valence Fluctuations in the Superconductivity of Ce122 Compounds. *Phys. Rev. Lett.* **113**, 086403 (2014).
- [131] C. Pfeleiderer. Superconducting phases of *f*-electron compounds. *Rev. Mod. Phys.* **81**, 1551 (2009).
- [132] B. D. White, J. D. Thompson, and M. B. Maple. Unconventional superconductivity in heavy-fermion compounds. *Physica C* **514**, 246 (2015).
- [133] N. Harrison, S. E. Sebastian, C. H. Mielke, A. Paris, M. J. Gordon, C. A. Swenson, D. G. Rickel, M. D. Pacheco, P. F. Ruminer, J. B. Schillig, J. R. Sims, A. H. Lacerda, M.-T. Suzuki, H. Harima, and T. Ebihara. Fermi surface of CeIn₃ above the Néel critical field. *Phys. Rev. Lett.* **99**, 056401 (2007).
- [134] N. K. Sato, N. Aso, K. Miyake, R. Shiina, P. Thalmeier, G. Varelogiannis, C. Geibel, F. Steglich, P. Fulde, and T. Komatsubara. Strong coupling between local moments and superconducting 'heavy' electrons in UPd₂Al₃. *Nature* **410**, 340 (2001).
- [135] Y. Ōnuki, I. Ukon, S. W. Yun, I. Umehara, K. Satoh, T. Fukuhara, H. Sato, S. Takayanagi, M. Shikama, and A. Ochiai. Magnetic and Electrical Properties of U-Ge Intermetallic Compounds. *J. Phys. Soc. Jpn.* **61**, 293 (1992).

- [136] G. Oomi, T. Kagayama, K. Nishimura, S.W. Yun, and Y. Ōnuki. Electrical resistivity of single crystalline UGe_2 at high pressure and high magnetic field. *Physica B* **206-207**, 515 (1995).
- [137] A. Huxley, E. Ressouche, B. Grenier, D. Aoki, J. Flouquet, and C. Pfleiderer. The co-existence of superconductivity and ferromagnetism in actinide compounds. *J. Phys.: Condens. Matter* **15**, 28 (2003).
- [138] A. Huxley, I. Sheikin, E. Ressouche, N. Kernavanois, D. Braithwaite, R. Calemczuk, and J. Flouquet. UGe_2 : A ferromagnetic spin-triplet superconductor. *Phys. Rev. B* **63**, 144519 (2001).
- [139] S. S. Saxena, P. Agarwal, K. Ahilan, F. M. Grosche, R. K. W. Haselwimmer, M. J. Steiner, E. Pugh, I. R. Walker, S. R. Julian, P. Monthoux, G. G. Lonzarich, A. Huxley, I. Sheikin, D. Braithwaite, and J. Flouquet. Superconductivity on the border of itinerant-electron ferromagnetism in UGe_2 . *Nature* **406**, 587 (2000).
- [140] R Vollmer, C Pfleiderer, H.v Löhneysen, E.D Bauer, and M. B. Maple. Low temperature specific heat of polycrystalline UGe_2 at high pressure. *Physica B* **312**, 112 (2002).
- [141] A. B. Shick, V. Janiš, V. Drchal, and W. E. Pickett Spin and orbital magnetic state of UGe_2 under pressure. *Phys. Rev. B* **70**, 134506 (2004).
- [142] R. C. Werthamer, R. Helfand, and P. C. Hohenberg. Temperature and Purity Dependence of the Superconducting Critical Field, H_{c2} . III. Electron Spin and Spin-Orbit Effects. *Phys. Rev.* **147**, 295 (1966).
- [143] K. Maki. Effect of Pauli Paramagnetism on Magnetic Properties of High-Field Superconductors. *Phys. Rev.* **148**, 362 (1966).
- [144] B. -L. Young, R. R. Urbano, N. J. Curro, J. D. Thompson, J. L. Sarrao, A. B. Vorontsov, and M. J. Graf. Microscopic evidence for field-induced magnetism in CeCoIn_5 . *Phys. Rev. Lett.* **98**, 036402 (2007).
- [145] M. Kenzelmann, S. Gerber, N. Egetenmeyer, J. L. Gavilano, Th. Strässle, A. D. Bianchi, E. Ressouche, R. Movshovich, E. D. Bauer, J. L. Sarrao, and J. D. Thompson. Evidence for a Magnetically Driven Superconducting Q Phase of CeCoIn_5 . *Phys. Rev. Lett.* **104**, 127001 (2010).
- [146] G. Koutroulakis, M. D. Stewart, Jr., V. F. Mitrović, M. Horvatić, C. Berthier, G. Lapertot, and J. Flouquet Field evolution of coexisting superconducting and magnetic orders in CeCoIn_5 . *Phys. Rev. Lett.* **104**, 087001 (2010).
- [147] V. P. Michal, and V. P. Mineev. Field-induced spin-excitation, condensation in the $d_{x^2-y^2}$ -wave superconductor CeCoIn_5 . *Phys. Rev. B* **84**, 052508 (2011).
- [148] P. Fulde, and R. A. Ferrell. Superconductivity in strong spin-exchange field. *Phys. Rev.* **135**, A550 (1964).
- [149] A. I. Larkin, and Y. N. Ovchinnikov. Inhomogeneous state of superconductors. *Sov. Phys. JETP-USSR* **20**, 762 (1965).
- [150] G. C. Psaltakis, and E. C. Fenton. Superconductivity and spin-density waves: organic superconductors. *J. Phys. C* **16**, 3913 (1984).
- [151] H. Shimahara. Coexistence of singlet and triplet attractive channels in the pairing interactions mediated by antiferromagnetic fluctuations. *J. Phys. Soc. Jpn.* **69**, 1966 (2000).
- [152] A. G. Lebed. Cooper Pairs with Broken Parity and Spin-Rotational Symmetries in d-Wave Superconductors. *Phys. Rev. Lett.* **96**, 037002 (2006).
- [153] A. Aperis, G. Varelogiannis, and P. B. Littlewood. Magnetic-Field-Induced Pattern of Coexisting Condensates in the Superconducting State of CeCoIn_5 . *Phys. Rev. Lett.* **104**, 216403 (2010).

- [154] K. Yang, and S. L. Sondhi. Response of a $d_{x^2-y^2}$ superconductor to a Zeeman magnetic field. *Phys. Rev. B* **57**, 8566 (1998).
- [155] Y. Yanase and M. Sigrist. Antiferromagnetic order and π -triplet pairing in the Fulde-Ferrell-Larkin-Ovchinnikov state. *J. Phys. Soc. Jpn.* **78**, 114715 (2009).
- [156] Y. Kato, C. D. Batista, and I. Vekhter. Antiferromagnetic order in Pauli-limited superconductors. *Phys. Rev. Lett.* **107**, 096401 (2011).
- [157] K. M. Suzuki, M. Ichioka, and K. Machida. Theory of an inherent spin-density-wave instability due to vortices in superconductors with strong Pauli effects. *Phys. Rev. B* **83**, 140503(R) (2011).
- [158] Y. Hatakeyama, and R. Ikeda. Antiferromagnetic order oriented by Fulde-Ferrell-Larkin-Ovchinnikov superconducting order. *Phys. Rev. B* **91**, 094504 (2015).
- [159] J. -L. Basdevant, J. Rich, and M. Spiro. *Fundamentals in Nuclear Physics*. Springer, p. 155, 2005.
- [160] Institut Laue-Langevin. Description of the ILL HFR (High-Flux Reactor). <https://www.ill.eu/reactor-environment-safety/high-flux-reactor/technical-characteristics/> 20, July 2017.
- [161] Paul Scherrer Institut. Accelerator and proton beam line. <https://www.psi.ch/bsq/proton-accelerator> 20, July 2017.
- [162] Paul Scherrer Institut. Spallation Target. <https://www.psi.ch/bsq/spallation-target> 20, July 2017.
- [163] Swiss Neutronics Neutron Optical Components and Instruments. Concept of Neutron Mirror / Supermirror. www.swissneutronics.ch/index.php?id=20, July 2017.
- [164] NIST Center for Neutron Research. Neutron scattering lengths and cross sections. <https://www.ncnr.nist.gov/resources/n-lengths/> 21, July 2017.
- [165] T. Kimura, T. Goto, H. Shintani, K. Ishizaka, T. Arima, and Y. Tokura. Magnetic control of ferroelectric polarization. *Nature* **426**, 55 (2003).
- [166] A. Wills. Magnetic structures and their determination using group theory. *J. Phys. IV France* **11**, 133 (2001).
- [167] C. J. Bradley, and A. P. Cracknell. *The Mathematical Theory of Symmetry in Solids*. Clarendon Press, Oxford, 1972.
- [168] bilbao crystallographic server. Irreducible representations of the Space Groups. <http://www.cryst.ehu.es/cgi-bin/cryst/programs/representations.pl?tipogrupospg> 31, July 2017.
- [169] J. Rodríguez-Caravajal. Recent advances in magnetic structure determination by neutron powder diffraction. *Physica B* **192**, 55 (1993).
- [170] Paul Scherrer Institut. HRPT: High-Resolution Powder Diffractometer for Thermal Neutrons. <http://sinq.web.psi.ch/sinq/instr/hrpt/index.html> 1, August 2017.
- [171] Institut Laue-Langevin. D10 - Four-circle diffractometer with three-axis energy analysis. <https://www.ill.eu/instruments-support/instruments-groups/instruments/d10/description/instrument-layout/> 1, August 2017.
- [172] H. M. Rietveld. A profile refinement method for nuclear and magnetic structures. *J. Appl. Cryst.* **2**, 65 (1969).
- [173] J. Rodríguez-Caravajal. An introduction to the program FullProf 2000. <https://www.psi.ch/sinq/dmc/ManualsEN/fullprof.pdf> 1, August 2017.

- [174] Institut Laue-Langevin. D23 - Thermal neutron lifting-counter two-axis diffractometer. <https://www.ill.eu/instruments-support/instruments-groups/instruments/d23/description/instrument-layout/> 2, August 2017.
- [175] Institut Laue-Langevin. IN12 - Cold neutron three-axis spectrometer. <https://www.ill.eu/instruments-support/instruments-groups/instruments/in12/description/instrument-layout/> 2, August 2017.
- [176] E. Ressouche. *Private communication*.
- [177] Paul Scherrer Institut. RITA-II: Triple axis spectrometer. <https://www.psi.ch/sinq/ritaii/rita-ii> 2, August 2017.
- [178] Paul Scherrer Institut. MA15 Specifications. <http://lns00.psi.ch/sinqwiki/Wiki.jsp?page=MA15Specifications> 2, August 2017.
- [179] F. Pobell. *Matter and Methods at Low Temperatures*. Springer, 2007.
- [180] Scientific Products. Cryostats introduction. <http://www.asscientific.co.uk> 3, August 2017.
- [181] I. F. Bailey. A review of sample environments in neutron scattering. *Z. Kristallogr.* **218**, 84 (2003).
- [182] Institut Laue-Langevin. Helium flow. <https://www.ill.eu/instruments-support/sample-environment/about-us/history/cryogenics/helium-flow/> 3, August 2017.
- [183] Oxford instruments. Superconducting magnets. <https://www.oxford-instruments.com/products/cryogenic-environments/superconducting-magnet-systems> 3, August 2017.
- [184] G. J. McIntyre, B. Ouladdiaf, C. M. E. Zeyen, F. Thomas, A. Benoit, and S. Pujol. textit Four-circle single-crystal diffractometry at mK temperatures on D10. The ILL Millenium Symposium & European User Meeting, p. 189 (2001).
- [185] L. Howald, G. Seyfarth, G. Knebel, D. Aoki, and G Lapertot. Behavior of the quantum critical point and the Fermi-liquid domain in the heavy fermion superconductor CeCoIn₅ studied by resistivity. *J. Phys. Soc. Jpn.* **80**, 024710 (2011).
- [186] Y. Kasahara, Y. Nakajima, K. Izawa, Y. Matsuda, K. Behnia, H. Shishido, R. Settai, and Y. Ōnuki. Anomalous Quasiparticle Transport in the Superconducting State of CeCoIn₅. *Phys. Rev. B* **72**, 214515 (2005).
- [187] G. D. Morris, R. H. Heffner, N. O. Moreno, P. G. Pagliuso, J. L. Sarrao, S. R. Dunsiger, G. J. Nieuwenhuys, D. E. MacLaughlin, and O. O. Bernal. Random spin freezing in Ce₂MIn₈ ($M = \text{Co, Rh, Ir}$) heavy-fermion materials. *Phys. Rev. B* **69**, 214415 (2004).
- [188] R. Settai, H. Shishido, S. Ikeda, Y. Murakawa, M. Nakashima, D. Aoki, Y. Haga, H. Harima, and Y. Ōnuki. Quasi-two-dimensional Fermi surfaces and the de Haas van Alphen oscillation in both the normal and the superconducting mixed states of CeCoIn₅. *J. Phys.: Condens. Matter* **13**, L627 (2001).
- [189] D. Hall, E. C. Palm, T. P. Murphy, S. W. Tozer, Z. Fisk, U. Alver, R. G. Goodrich, J. L. Sarrao, P. G. Pagliuso, and T. Ebihara. Fermi surface of the heavy-fermion superconductor CeCoIn₅: The de Haas-van Alphen effect in the normal state. *Phys. Rev. B* **64**, 212508 (2001).
- [190] A. Koitzsch, S. V. Borisenko, D. Inosov, J. Geck, V. B. Zabolotnyy, H. Shiozawa, M. Knupfer, J. Fink, B. Büchner, E. D. Bauer, J. L. Sarrao, and R. Follath. Hybridization effects in CeCoIn₅ observed by angle-resolved photoemission. *Phys. Rev. B* **77**, 155128 (2008).

- [191] A. Koitzsch, I. Opahle, S. Elgazzar, S. V. Borisenko, J. Geck, V. B. Zabolotnyy, D. Inosov, H. Shiozawa, M. Richter, M. Knupfer, J. Fink, B. Büchner, E. D. Bauer, J. L. Sarrao, and R. Follath. Electronic structure of CeCoIn₅ from angle-resolved photoemission spectroscopy. *Phys. Rev. B* **79**, 075104 (2009).
- [192] A. Koitzsch, T. K. Kim, U. Treske, M. Knupfer, B. Büchner, M. Richter, I. Opahle, R. Follath, E. D. Bauer, and J. L. Sarrao. Band-dependent emergence of heavy quasiparticles in CeCoIn₅. *Phys. Rev. B* **88**, 035124 (2013).
- [193] S. Fujimori, A. Fujimori, K. Shimada, T. Narimura, K. Kobayashi, H. Namatame, M. Taniguchi, H. Harima, H. Shishido, S. Ikeda, D. Aoki, Y. Tokiwa, Y. Haga, and Y. Ōnuki. Direct observation of a quasiparticle band in CeIrIn₅: An angle-resolved photoemission spectroscopy study. *Phys. Rev. B* **73**, 224517 (2006).
- [194] A. Benoit, J. X. Boucherle, P. Convert, J. Flouquet, J. Palleau, and J. Schweizer. Magnetic structure of the compound CeIn₃. *Solid State. Comm.* **34**, 293 (1980).
- [195] K. Haule, C. -H. Yee, and K. Kim. Dynamical mean-field theory within the full-potential methods: Electronic structure of CeIrIn₅, CeCoIn₅, and CeRhIn₅. *Phys. Rev. B* **81**, 195107 (2010).
- [196] T. Willers, F. Strigari, Z. Hu, V. Sessi, N. B. Brookes, E. D. Bauer, J. L. Sarrao, J. D. Thompson, A. Tanaka, S. Wirth, L. H. Tjeng, and A. Severing. Correlation between ground state and orbital anisotropy in heavy fermion materials. *Proc. Natl Acad. Sci. USA* **112**(8), 2384 (2015).
- [197] W. K. Park, J. L. Sarrao, J. D. Thompson, and L. H. Greene. Andreev Reflection in Heavy-Fermion Superconductors and Order Parameter Symmetry in CeCoIn₅. *Phys. Rev. Lett.* **100**, 177001 (2008).
- [198] R. Movshovich, M. Jaime, J. D. Thompson, C. Petrovic, Z. Fisk, P. G. Pagliuso, and J. L. Sarrao. Unconventional superconductivity in CeIrIn₅ and CeCoIn₅: specific heat and thermal conductivity studies. *Phys. Rev. Lett.* **86**, 5152 (2001).
- [199] K. Izawa, H. Yamaguchi, Y. Matsuda, H. Shishido, R. Settai R, and Y. Ōnuki. Angular position of nodes in the superconducting gap of quasi-2D heavy-fermion superconductor CeCoIn₅. *Phys. Rev. Lett.* **87**, 057002 (2001).
- [200] K. An, T. Sakakibara, R. Settai, Y. Ōnuki, M. Hiragi, M. Ichioka, and K. Machida. Sign reversal of field-angle resolved heat capacity oscillations in a heavy fermion superconductor CeCoIn₅ and d_{x²-y²} pairing symmetry. *Phys. Rev. Lett.* **104**, 037002 (2010).
- [201] S. Raymond, and G. Lapertot. Ising Incommensurate Spin Resonance of CeCoIn₅: A Dynamical Precursor of the Q Phase. *Phys. Rev. Lett.* **115**, 037001 (2015).
- [202] J. Paglione, M. A. Tanatar, D. G. Hawthorn, E. Boaknin, R. W. Hill, F. Ronning, M. Sutherland, L. Taillefer, C. Petrovic and P. C Canfield. Field-induced quantum critical point in CeCoIn₅. *Phys. Rev. Lett.* **91**, 246405 (2003).
- [203] J. S. Kim, J. Alwood, G. R. Stewart, J. L. Sarrao, and J. D. Thompson. Specific heat in high magnetic fields and non-Fermi-liquid behavior in CeMIn₅ (M = Ir, Co). *Phys. Rev. B* **64**, 134524 (2001).
- [204] Y. Kohori, Y. Yamato, Y. Iwamoto, T. Kohara, E. D. Bauer, M. B. Maple, and J. L. Sarrao,. NMR and NQR studies of the heavy fermion superconductors CeTIn₅ (T = Co, Ir). *Phys. Rev. B* **64**, 134526 (2001).
- [205] S. Gerber. *Interplay of Superconductivity and Magnetism in Unconventional Superconductors*. Msc thesis, ETH Zürich and Paul Scherrer Insitut, 2009.

- [206] A. D. Bianchi, M. Kenzelmann, L. DeBeer-Schmitt, J. S. White, E. M. Forgan, J. Mesot, M. Zolliker, J. Kohlbrecher, R. Movshovich, E. D. Bauer, J. L. Sarrao, Z. Fisk, C. Petrovic, and M. R. Eskildsen. Superconducting Vortices in CeCoIn₅: Toward the Pauli-Limiting Field. *Science* **319**, 177 (2008).
- [207] A. M. Clogston. Upper limit for the critical field in hard superconductors. *Phys. Rev. Lett.* **9**, 266 (1962).
- [208] A. McCollam, S. R. Julian, P. M. C. Rourke, D. Aoki, and J. Flouquet. Anomalous de Haas-van Alphen Oscillations in CeCoIn₅. *Phys. Rev. Lett.* **94**, 186401 (2005).
- [209] J. S. White, P. Das, M. R. Eskildsen, L. DeBeer-Schmitt, E. M. Forgan, A. D. Bianchi, M. Kenzelmann, M. Zolliker, S. Gerber, J. L. Gavilano, J. Mesot, R. Movshovich, E. D. Bauer, J. L. Sarrao, and C. Petrovic. Observations of Pauli paramagnetic effects on the flux line lattice in CeCoIn₅. *New J. Phys.* **12**, 023026 (2010).
- [210] P. Das, J. S. White, A. T. Holmes, S. Gerber, E. M. Forgan, A. D. Bianchi, M. Kenzelmann, M. Zolliker, J. L. Gavilano, E. D. Bauer, J. L. Sarrao, C. Petrovic, and M. R. Eskildsen. Vortex Lattice Studies in CeCoIn₅ with $H \perp c$. *Phys. Rev. Lett.* **108**, 087002 (2012).
- [211] M. R. Eskildsen, E. M. Forgan, and H. Kawano-Furukawa. Vortex structures, penetration depth and pairing in iron-based superconductors studied by small-angle neutron scattering. *Rep. Prog. Phys.* **74**, 124504 (2011).
- [212] M. Ichioka, and K. Machida. Vortex states in superconductors with strong Pauli-paramagnetic effect. *Phys. Rev. B* **76**, 064502 (2007).
- [213] M. Ichioka, and K. Machida. Flux line lattice form factor and paramagnetic effects in type-II superconductors. *J. Phys. Conf. Ser.* **150**, 052074 (2009).
- [214] V. P. Michal, and V. P. Mineev. Paramagnetic effects in vortex lattice field distribution in strongly type-II superconductors. *Phys. Rev. B* **82**, 104505 (2010).
- [215] K. Aoyama, and R. Ikeda. Fluctuations and order of antiferromagnetism induced by paramagnetic pair breaking in superconducting vortex lattices. *Phys. Rev. B* **84**, 184516 (2011).
- [216] K. Aoyama, and R. Ikeda. Flux distribution in vortex lattice states in d-wave and paramagnetic superconductors. *J. Phys. Conf. Ser.* **273**, 012026 (2011).
- [217] N. Hiasa, and R. Ikeda. Instability of square vortex lattice in d-wave superconductors is due to paramagnetic depairing. *Phys. Rev. Lett.* **101**, 027001 (2008).
- [218] E. Blackburn, P. Das, M. R. Eskildsen, E. M. Forgan, M. Laver, C. Niedermayer, C. Petrovic, and J. S. White. Exploring the Fragile Antiferromagnetic Superconducting Phase in CeCoIn₅. *Phys. Rev. Lett.* **105**, 187001 (2010).
- [219] D. Y. Kim, S. -Z. Lin, F. Weickert, M. Kenzelmann, E. D. Bauer, F. Ronning, J. D. Thompson, and R. Movshovich. Intertwined Orders in Heavy-Fermion Superconductor CeCoIn₅. *Phys. Rev. X* **6**, 041059 (2016).
- [220] V. P. Mineev. Antiferromagnetic order in CeCoIn₅ oriented by spin-orbital coupling. *Low Temp. Phys.* **43**, 11 (2017).
- [221] D. F. Agterberg, M. Sigrist, and H. Tsunetsugu. Order parameter and vortices in the superconducting Q phase of CeCoIn₅. *Phys. Rev. Lett.* **102**, 207004 (2009).
- [222] K. -I. Hosoya, and R. Ikeda. Possible Triplet Superconducting Order in Magnetic Superconducting Phase induced by Paramagnetic Pair-Breaking. *Phys. Rev. B* **95**, 224513 (2017).

- [223] C. Stock, C. Broholm, Y. Zhao, F. Demmel, H. J. Kang, K. C. Rule, and C. Petrovic. Magnetic Field Splitting of the Spin Resonance in CeCoIn₅. *Phys. Rev. Lett.* **109**, 167207 (2012).
- [224] S. Raymond, K. Kaneko, A. Hiess, P. Steffens, and G. Lapertot. Evidence for Three Fluctuation Channels in the Spin Resonance of the Unconventional Superconductor CeCoIn₅. *Phys. Rev. Lett.* **109**, 237210 (2012).
- [225] G. Knebel, D. Aoki, J. -P. Brison, L. Howald, G. Lapertot, J. Panarin, S. Raymond, and J. Flouquet. Competition and/or coexistence of antiferromagnetism and superconductivity in CeRhIn₅ and CeCoIn₅. *Phys. Stat. Solidi. B* **247**, 557 (2010).
- [226] H. Yamaoka, Y. Yamamoto, E. F. Schwier, F. Honda, Y. Zekko, Y. Ohta, J. -F. Lin, M. Nakatake, H. Iwasawa, M. Arita, K. Shimada, N. Hiraoka, H. Ishii, K. -D. Tsuei, and J. Mizuki. Pressure and temperature dependence of the Ce valence and *c-f* hybridization gap in CeTIn₅ (*T* = Co, Rh, Ir) heavy-fermion superconductors. *Phys. Rev. B* **92**, 235110 (2015).
- [227] C. F. Miclea, M. Nicklas, D. Parker, K. Maki, J. L. Sarrao, J. D. Thompson, G. Sparrn, and F. Steglich. Pressure Dependence of the Fulde-Ferrell-Larkin-Ovchinnikov State in CeCoIn₅. *Phys. Rev. Lett.* **96**, 117001 (2006).
- [228] T. Tayama, Y. Namai, T. Sakakibara, M. Hedo, Y. Uwatoko, H. Shishido, R. Settai and Y. Ōnuki. Pressure Dependence of the First-Order Superconducting Phase Transition in CeCoIn₅. *J. Phys. Soc. Jpn.* **74**, 1115 (2005).
- [229] C. H. Booth, E. D. Bauer, and J. N. Mitchell. A moving target: responding to magnetic and structural disorder in lanthanide- and actinide-based superconductors. *IOP Conf. Ser-Mat. Sci.* **9**, 012087 (2010).
- [230] C. H. Booth, E. D. Bauer, A. D. Bianchi, F. Ronning, J. D. Thompson, J. L. Sarrao, J. Y. Cho, J. Y. Chan, C. Capan, and Z. Fisk. Local structure and site occupancy of Cd and Hg substitutions in CeTIn₅ (*T* = Co, Rh, and Ir). *Phys. Rev. B* **79**, 144519 (2009).
- [231] M. Nicklas, O. Stockert, T. Park, K. Habicht, K. Kiefer, L. D. Pham, J. D. Thompson, Z. Fisk, and F. Steglich. Magnetic structure of Cd-doped CeCoIn₅. *Phys. Rev. B* **76**, 052401 (2007).
- [232] S. Seo, Xin Lu, J. -X. Zhu, R. R. Urbano, N. Curro, E. D. Bauer, V. A. Sidorov, L. D. Pham, T. Park, Z. Fisk, and J. D. Thompson. Disorder in quantum critical superconductors. *Nat. Phys.* **10**, 120 (2014).
- [233] L. Howald, E. Stimp, P. Dalmás de Réotier, A. Yaouanc, S. Raymond, C. Piamonteze, G. Lapertot, C. Baines, and H. Keller. Evidence for Coexistence of Bulk Superconductivity and Itinerant Antiferromagnetism in the Heavy Fermion System CeCo(In_{1-x}Cd_x)₅. *Sci. Rep.* **5**, 12528 (2015).
- [234] M. Yokoyama, H. Mashiko, R. Otaka, Y. Sakon, and K. Fujimura. Pauli-limited superconductivity and antiferromagnetism in the heavy-fermion compound CeCo(In_{1-x}Zn_x)₅. *Phys. Rev. B* **92**, 184509 (2015).
- [235] S. M. Ramos, M. B. Fontes, E. N. Hering, M. A. Continentino, E. Baggio-Saitovich, F. D. Neto, E. M. Bittar, P. G. Pagliuso, E. D. Bauer, J. L. Sarrao, and J. D. Thompson. Superconducting Quantum Critical Point in CeCoIn_{5-x}Sn_x. *Phys. Rev. Lett.* **105**, 126401 (2010).
- [236] M. N. Ou, K. Gofryk, R. E. Baumbach, S. S. Stoyko, J. D. Thompson, J. M. Lawrence, E. D. Bauer, F. Ronning, A. Mar, and Y. Y. Chen. Hole doping effect on superconductivity in Ce(Co_{1-x}Ru_x)In₅. *Phys. Rev. B* **88**, 195134 (2013).
- [237] H. Kim, M. A. Tanatar, R. Flint, C. Petrovic, R. Hu, B. D. White, I. K. Lum, M. B. Maple, and R. Prozorov. Nodal to Nodeless Superconducting Energy-Gap Structure Change Concomitant with Fermi-Surface Reconstruction in the Heavy-Fermion Compound CeCoIn₅. *Phys. Rev. Lett.* **114**, 027003 (2015).

- [238] Y. Xu, J. K. Dong, I. K. Lum, J. Zhang, X. C. Hong, L. P. He, K. F. Wang, Y. C. Ma, C. Petrovic, M. B. Maple, L. Shu, and S. Y. Li. Universal heat conduction in $Ce_{1-x}Yb_xCoIn_5$: Evidence for robust nodal d -wave superconducting gap. *Phys. Rev. B* **93**, 064502 (2016).
- [239] L. Shu, R. E. Baumbach, M. Janoschek, E. Gonzales, K. Huang, T. A. Sayles, J. Paglione, J. O'Brien, J. J. Hamlin, D. A. Zocco, P. -C. Ho, C. A. McElroy, and M. B. Maple. Correlated Electron State in $Ce_{1-x}Yb_xCoIn_5$ Stabilized by Cooperative Valence Fluctuations. *Phys. Rev. Lett.* **106**, 156403 (2011).
- [240] Y. P. Singh, D. J. Haney, X. Y. Huang, I. K. Lum, B. D. White, M. Dzero, M. B. Maple, and C. C. Almasan. From local moment to mixed-valence regime in $Ce_{1-x}Yb_xCoIn_5$ alloys. *Phys. Rev. B* **89**, 115106 (2014).
- [241] C. H. Booth, T. Durakiewicz, C. Capan, D. Hurt, A. D. Bianchi, J. J. Joyce, and Z. Fisk. Electronic structure and f -orbital occupancy in Yb-substituted $CeCoIn_5$. *Phys. Rev. B* **83**, 235117 (2011).
- [242] M. A. Tanatar, J. Paglione, S. Nakatsuji, D. G. Hawthorn, E. Boaknin, R. W. Hill, F. Ronning, M. Sutherland, L. Taillefer, C. Petrovic, P. C. Canfield, and Z. Fisk. Unpaired Electrons in the Heavy-Fermion Superconductor $CeCoIn_5$. *Phys. Rev. Lett.* **95**, 067002 (2005).
- [243] C. Petrovic, S. L. Bud'ko, V. G. Kogan, and P. C. Canfield. Effects of La substitution on the superconducting state of $CeCoIn_5$. *Phys. Rev. B* **66**, 054534 (2002).
- [244] W. Bao, P. G. Pagliuso, J. L. Sarrao, J. D. Thompson, and Z. Fisk. Incommensurate magnetic structure of $CeRhIn_5$. *Phys. Rev. B* **62**, 14621(R) (2000).
- [245] D. M. Fobes, E. D. Bauer, J. D. Thompson, A. Sazonov, V. Hutanu, S. Zhang, F. Ronning, and M. Janoschek. Low temperature magnetic structure of $CeRhIn_5$ by neutron diffraction on absorption-optimized samples. *J. Phys.: Condens. Matter* **29**, 17LT01 (2017).
- [246] A. Llobet, A. D. Christianson, Wei Bao, J. S. Gardner, I. P. Swainson, J. W. Lynn, J.-M. Mignot, K. Prokes, P. G. Pagliuso, N. O. Moreno, J. L. Sarrao, J. D. Thompson, and A. H. Lacerda. Novel Coexistence of Superconductivity with Two Distinct Magnetic Orders. *Phys. Rev. Lett.* **95**, 217002 (2005).
- [247] S. Kawasaki, M. Yashima, Y. Mugino, H. Mukuda, Y. Kitaoka, H. Shishido, and Y. Ōnuki. Enhancing the Superconducting Transition Temperature of $CeRh_{1-x}Ir_xIn_5$ due to the Strong-Coupling Effects of Antiferromagnetic Spin Fluctuations: An ^{115}In Nuclear Quadrupole Resonance Study. *Phys. Rev. Lett.* **96**, 147001 (2006).
- [248] S. Ohira-Kawamura, H. Shishido, A. Yoshida, R. Okazaki, H. Harima, and Y. Matsuda. Competition between unconventional superconductivity and incommensurate antiferromagnetic order in $CeRh_{1-x}Co_xIn_5$. *Phys. Rev. B* **76**, 132507 (2007).
- [249] M. Yokoyama, N. Oyama, H. Amitsuka, S. Oinuma, I. Kawasaki, K. Tenya, M. Matsuura, K. Hirota, and T. J. Sato. Change of antiferromagnetic structure near a quantum critical point in $CeRh_{1-x}Co_xIn_5$. *Phys. Rev. B* **77**, 224501 (2008).
- [250] M. Yokoyama, N. Oyama, H. Amitsuka, S. Oinuma, I. Kawasaki, K. Tenya, M. Matsuura, and K. Hirota. Polarized neutron scattering study on antiferromagnetic states in $CeRh_{0.6}Co_{0.4}In_5$. *Physica B* **403**, 812 (2008).
- [251] S. Raymond, S. M. Ramos, D. Aoki, G. Knebel, V. P. Mineev, and G. Lapertot. Magnetic Order in $Ce_{0.95}Nd_{0.05}CoIn_5$: The Q-Phase at Zero Magnetic Field. *J. Phys. Soc. Jpn.* **83**, 013707 (2014).
- [252] G. L. Molnár. *Handbook of Prompt Gamma Activation Analysis with Neutron Beams*. Kluwer Academic Publishers, 2004.

- [253] P. Čermák, P. Javorský, M. Kratochvílová, K. Pajskr, M. Klicpera, B. Ouladdiaf, M. -H. Lemée-Cailleau, J. Rodriguez-Carvajal, and M. Boehm. Magnetic structures of non-cerium analogues of heavy-fermion Ce_2RhIn_8 : The case of Nd_2RhIn_8 , Dy_2RhIn_8 , and Er_2RhIn_8 . *Phys. Rev. B* **89**, 184409 (2014).
- [254] S. Chang, P. G. Pagliuso, W. Bao, J. S. Gardner, I. P. Swainson, J. L. Sarrao, and H. Nakotte. Magnetic structure of antiferromagnetic NdRhIn_5 . *Phys. Rev. B* **66**, 132417 (2002).
- [255] J. H. J. Martiny, M. N. Gastiasoro, I. Vekhter, and B. M. Andersen. Impurity-induced antiferromagnetic order in Pauli-limited nodal superconductors: Application to heavy-fermion CeCoIn_5 . *Phys. Rev. B* **92**, 224510 (2015).
- [256] S. -Z. Lin, and J. -X. Zhu. Impurity-induced magnetic droplet in unconventional superconductors near magnetic instability: Application to Nd-doped CeCoIn_5 . *Phys. Rev. B* **96**, 224502 (2017).
- [257] P. F. S. Rosa, J. Kang, Y. Luo, N. Wakeham, E. D. Bauer, F. Ronning, Z. Fisk, R. M. Fernandes, and J. D. Thompson. Competing magnetic orders in the superconducting state of heavy-fermion CeRhIn_5 under pressure. *Proc. Natl Acad. Sci. USA* **114**, 5384 (2017).
- [258] N. Van Hieu, T. Takeuchi, H. Shishido, C. Tonohiro, T. Yamada, H. Nakashima, K. Sugiyama, R. Settai, T. D. Matsuda, Y. Haga, M. Hagiwara, K. Kindo, S. Araki, Y. Nozue, and Y. Ōnuki. Magnetic Properties and Crystalline Electric Field Scheme in RRhIn_5 (R: Rare Earth). *J. Phys. Soc. Jpn.* **76**, 064702 (2007).
- [259] T. Willers, Z. Hu, N. Hollmann, P. O. Körner, J. Gegner, T. Burnus, H. Fujiwara, A. Tanaka, D. Schmitz, H. H. Hsieh, H. -J. Lin, C. T. Chen, E. D. Bauer, J. L. Sarrao, E. Goremychkin, M. Koza, L. H. Tjeng, and A. Severing. Crystal-field and Kondo-scale investigations of CeMIn_5 ($M = \text{Co, Ir, and Rh}$): A combined x-ray absorption and inelastic neutron scattering study. *Phys. Rev. B* **81**, 195114 (2010).
- [260] P. F. S. Rosa, A. Oostra, J. D. Thompson, P. G. Pagliuso, and Z. Fisk. Unusual Kondo-hole effect and crystal-field frustration in Nd-doped CeRhIn_5 . *Phys. Rev. B* **94**, 045101 (2016).
- [261] P. A. Frigeri, D. F. Agterberg, A. Koga, and M. Sigrist. Superconductivity without Inversion Symmetry: MnSi versus CePt_3Si . *Phys. Rev. Lett.* **92**, 097001 (2004).
- [262] B. Fåk, D. T. Adroja, M. Enderle, M. Böhm, G. Lapertot, and V. P. Mineev. Anomalous Spin Response in the Non-Centrosymmetric Metal CePt_3Si . *J. Phys. Soc. Jpn.* **83**, 063703 (2014).
- [263] D. Y. Kim, S. -Z. Lin, E. D. Bauer, F. Ronning, J. D. Thompson, and R. Movshovich. Switching dynamics of the spin density wave in superconducting CeCoIn_5 . *Phys. Rev. B* **95**, 241110(R) (2017).
- [264] A. Akbari, and P. Thalmeier. Field-induced spin exciton doublet splitting in $d_{x^2-y^2}$ -wave CeMIn_5 ($M = \text{Rh, Ir, Co}$) heavy-electron superconductors. *Phys. Rev. B* **86**, 134516 (2012).
- [265] M. Yashima, H. Mukuda, Y. Kitaoka, H. Shishido, R. Settai, and Y. Ōnuki. Strong coupling between antiferromagnetic and superconducting order parameters of CeRhIn_5 studied by ^{115}In nuclear quadrupole resonance spectroscopy. *Phys. Rev. B* **79**, 214528 (2009).
- [266] W. Lv, A. Moreo, and E. Dagotto. Double magnetic resonance and spin anisotropy in Fe-based superconductors due to static and fluctuating antiferromagnetic orders. *Phys. Rev. B* **89**, 104510 (2014).
- [267] M. Liu, C. Lester, J. Kulda, X. Lu, H. Luo, M. Wang, S. M. Hayden, and P. Dai. Polarized neutron scattering studies of magnetic excitations in electron-overdoped superconducting $\text{BaFe}_{1.85}\text{Ni}_{0.15}\text{As}$. *Phys. Rev. B* **85**, 214516 (2012).

- [268] F. Wasser, C.H. Lee, K. Kihou, P. Steffens, K. Schmalzl, N. Qureshi, M. Braden, Anisotropic resonance modes emerging in an antiferromagnetic superconducting state. *Sci. Rep.* **7**, 10307 (2017).
- [269] D. K. Pratt, W. Tian, A. Kreyssig, J. L. Zarestky, S. Nandi, N. Ni, S. L. Bud'ko, P. C. Canfield, A. I. Goldman, and R. J. McQueen. Coexistence of Competing Antiferromagnetic and Superconducting Phases in the Underdoped $\text{Ba}(\text{Fe}_{0.953}\text{Co}_{0.047})_2\text{As}_2$ Compound Using X-ray and Neutron Scattering Techniques. *Phys. Rev. Lett.* **103**, 087001 (2009).
- [270] H. Shishido, S. Yamada, K. Sugii, M. Shimozawa, Y. Yanase, and M. Yamashita. dHvA measurements of CeCoIn_5 at ultra-low temperatures. *Conference on Strongly Correlated Electron Systems* (2017).
- [271] P. Dai. *Private communication*.
- [272] Paul Scherrer Institut. High-field And Low temperature instrument (HAL-9500). <https://www.psi.ch/smus/hal-9500> 13, September 2017.
- [273] J. Kindervater, N. Martin, W. Häussler, M. Krautloher, C. Fuchs, S. Mühlbauer, J. A. Lim, E. Blackburn, P. Böni, and C. Pfleiderer. Neutron spin echo spectroscopy under 17T magnetic field at RESEDA. *EPJ Web. Conf.* **83**, 03008 (2015).
- [274] S. Raymond. *Private communication*.

Acknowledgments

This thesis results from contributions of many people. Firstly, I want to thank Joël Mesot, Michel Kenzelmann and Jorge Gavilano for their supervision. Their constant support, motivation, advice and faith in me triggered the intention to give my best on a daily basis. Their effective balance between guidance and independence had a tremendous impact on my development as a scientist.

I thank Joël Mesot for taking the responsibility as my doctoral advisor and for giving me the opportunity to work in such a fruitful and friendly environment. As the director of the Paul Scherrer Institut (PSI) he created an optimal scientific and social atmosphere that sparks a plethora of ideas. I enjoyed to come to work on every day for the last four years. Under the guidance of Michel Kenzelmann and Jorge Gavilano, I experienced the unique fortune of having two diverse and complementary supervisors. I sincerely thank Michel in encouraging me to tackle scientific questions in a deductive way, to think outside the box, to write in a simple and effective way and to sustainably promote our work outside the institute. I appreciate his constructive criticism, his enthusiasm and deep love for physics, all discussions about science and the honest personal advices. I thank him for the trust in me when I replaced him in scientific talks. It gave me a huge opportunity to promote our work and me as a scientist. I thank Jorge Gavilano for his constant support in any question about solid state and low-temperature physics. I appreciate his patience, optimism and the discussions during all beamtimes. I will be a lucky man, if I share the same enthusiasm as Jorge does close to his retirement. I thank both of them for the valuable inputs on every manuscript, beamtime proposal and application that we have planned.

I thank Manfred Sigrist for all the fruitful scientific discussions at the ETH Zürich. Moreover, he was always willing to help me with every administrative question in connection with the ETH, which cannot be taken for granted. I am thankful that such an expert in the field accepted to co-examine my Ph.D defense.

I would like to address special thanks to Stéphane Raymond. It is his merit that we have such a close collaboration between the Commissariat à l’Energie Atomique et aux Energies Alternatives (CEA) and the PSI with respect to this project. I thank for his tremendous support, for sharing his immense knowledge about neutron scattering and the 115-family with me and for his guidance in any non-scientific question at the Institut Laue-Langevin. I experienced Grenoble as a second home and we always managed that at least one of us was optimistic during the experiments.

My research outcome is a result of a multitude of close collaborations. I would like to acknowledge all people that are involved at PSI, *i.e.*, Nicolas Gauthier, Romain Sibille, Marek Bartkowiak, Christian Matt, Marisa Medarde, Oksana Zaharko, Christof Niedermayer, Lukas

Keller, Volodja Pomjakushin, Jürg Schefer, Urs Gasser, Ekaterina Pomjakushina, Kazmirez Conder, Jonas Birk, Damaris Tartarotti, Ruchika Yadav, Mahesh Ramakrishnan, Martin Neugebauer, Christian Wessler, Ludovic Howald, Robert Scheuermann, Tatsuo Goko, Chris Baines, Bernard Delley Nicola Casati, Antonio Cervellino, Ming Shi and Nicholas Plumb. Special thank is directed to Nicolas Gauthier, Romain Sibille, Marek Bartkowiak. Nicolas' programming skills are excellent and I enjoyed every single debate about the 115s with him. Under the guidance of Romain I was introduced to the world of solid state chemistry. I appreciate that he always kept his sense of humor, even when I lost mine. I also acknowledge Romain for the critical proofreading of this document. Marek's knowledge and technical skills are peerless. It was exciting to develop novel methods with him. In the beginning I often had no idea how the devices should even work.

I want to thank all collaborating people from the CEA and the Institut Laue-Langevin including Eric Ressouche, Bachir Ouladdiaf, Gaël Bastien, Georg Knebel, Dai Aoki, Paul Steffens, Martin Böhm, Louis-Pierre Regnault, Frédéric Bourdarot, Teresa Fernandez-Diaz, Chris Dewhurst, Pierre Dalmas de Réotier, Alain Young and Gérard Lapertot. Astrid Schneidewind, Petr Čermák, Bjørn Petersen and Zlot Revay from the Heinz Maier-Leibnitz Zentrum are acknowledged. Small-angle neutron scattering experiments were conducted in collaboration with Mark Laver and Ted Forgan. In addition, I thank Yasmine Sassa, Martin Månsson and Ola Forslund. Yasmine and Martin are not only collaborators, but guided me towards PSI while I was studying at ETH. I owe my deep thanks to them.

Inputs with respects to the published manuscripts, given by Manfred Sigrist, Simon Gerber, Duk Kim, Roman Movshovich, Yvan Sidis, Malte Grosche and John White are appreciated. I would like to address special thanks to Simon Gerber. As my Ph.D. predecessor he had always an open ear for me and supported me in countless issues.

I immensely profited from discussions with Joe Thompson, Eric Bauer, Mark Janoschek, Pengcheng Dai, Tuson Park, Daniel Agterberg, Peter Fulde, Oliver Stockert, Chris Stock, Jeoren Custers as well as Bertram Batlogg, Peter Böni, Luc Patthey, Christopher Mudry, Markus Müller, Desmond McMorrow, Mark Dean, Ignace Jarrige, Stuart Wilkins, Ghiacomo Ghiringhelli, Lucio Braicovich, Stephan Rosenkranz, Johan Chang and Oscar Thernberg.

I appreciate the excellent working atmosphere that arose/arises under the leadership of Kurt Clausen and Christian Rüegg in the department of research with neutrons and muons at PSI. I am thankful for both, the scientific discussions and the challenging ski races with Christian. I would like to thank my group leader Joachim Kolbrecher as well as Kazmirez Conder and Ekaterina Pomjakushina for letting me work in the chemistry lab. I received invaluable technical support from Markus Zolliker, Marek Bartkowiak, Stefan Fischer, Paul Schurter, Silvan Stamm, Walter Latscha, Christian Kägi and Jan Krebs at SINQ as well as Pascal Fouilloux and Bruno Vettard from CEA. I would also like to mention the radio protection group including Markus Häfeli for the great support when I had to transport an activated sample to Grenoble. Special thanks is addressed to the administrative work completed by Pamela Knupp and Renate Bercher.

I am thankful for the support of my constant office mate Saumya Mukherjee and would like to acknowledge Simon Ward, Shang Gao, Martin Rumini, Alun Biffin, Emmanuel Canévet, Cheptiakov Denis, Tom Fennell, Felix Goitl, Kaur Guratinder, Sumit Maity, Juan Mora, Jochen Stahn, Bertrand Roessli, Mark Koennecke, Sandor Toth, Katharina Rolfs, Dariusz Gawryluk, Voraksmay Ban, Gregory Tucker, Björn Wehinger, Mickaël Morin, Alexandra Turrini and all

friends I made on the various experiments, schools and conferences.

Last but not least, I would like to thank my family, friends and my wife Fabienne. I thank them for their constant support, for helping me back onto my feet when I fell down and pulling me to the ground, when it was necessary. I am thankful that they distracted me when I needed some distance to my work and that they accepted when my mind drifted away, because I was chasing a physical question.

The time I spent with all these people shaped me to become the person I am today and opened my eyes in various aspects. I owe them my deepest gratefulness!

Curriculum Vitae

Name Daniel Gabriel Mazzone
Nationality Swiss
Date of birth 15th December 1988
Email dani.mazzone@gmail.com
ResearcherID D-3824-2017
ORCID ID 0000-0002-0421-0625

Education

- 10/2013-10/2017 **Ph.D in Physics**
Paul Scherrer Institut (PSI), Villigen and Department of Physics, ETH Zürich, Switzerland
Group: Laboratory for Neutron Scattering and Imaging
Doctoral advisor: Prof. Dr. Joël Mesot
Supervisor: Prof. Dr. Michel Kenzelmann, Dr. Jorge Gavilano
Date of defense: 30.10.2017
Swiss National Science Foundation (SNSF) grant No.: 200021_147071
- 02/2012-10/2013 **Master of Science ETH in Physics**
Eidgenössische Technische Hochschule (ETH), Zürich, Switzerland
Average grade: 5.97/6
Master thesis: "Vortex Lattice Studies of the Mixed State of Yb₃Rh₄Sn₁₃ and β -Bi₂Pd"
- 09/2011-02/2012 **Research Traineeship**
Paul Scherrer Institut (PSI), Villigen Switzerland
Group: SwissFEL-CLS
Supervisor: Prof. Dr. Christoph Hauri
- 09/2008-03/2012 **Bachelor of Science ETH in Physics**
Eidgenössische Technische Hochschule (ETH), Zürich, Switzerland
Average grade: 5.77/6

- Winner of the "Polya-Preis" founded by "Polya-Fonds" of the ETH Zürich
- 08/2003-06/2008 **Matura**
 Kollegium Spiritus Sanctus, Brig, Switzerland
 Average grade: 5.1/6
 Main subject: Physics and Applied Mathematics
 Complementary subject: Chemistry
 Matriculation project: "Spieltheorie - Strategie und Anwendung"
 Winner of the "Moritz-Kämpfen-Stiftung" award.

Participation to scientific schools/conferences

- | | | |
|-------------------|---|-------------------|
| 13-17.07.2017 | International Conference on Neutron Scattering, <i>Daejeon, Korea</i> | conference |
| 28.08-01.09.2016 | 30 th Meeting of the European Crystallographic Association, <i>Basel, Switzerland</i> . | conference |
| 23-25.08.2016 | Annual Meeting of the Swiss Physical Society, <i>Lugano, Switzerland</i> . | conference |
| 08-13.05.2016 | International Conference on Strongly Correlated Electron Systems, <i>Hangzhou, China</i> . | conference |
| 30.08- 04.09.2015 | 6 th European Conference on Neutron Scattering, <i>Zaragoza, Spain</i> . | conference |
| 23-28.08.2015 | 11 th Materials and Mechanisms of Superconductivity 2015, <i>Geneva, Switzerland</i> . | conference |
| 05-10.07.2015 | 20 th International Conference on Magnetism, <i>Barcelona, Spain</i> . | conference |
| 18-23.01.2015 | MaNEP Winter School "Shedding light on correlated electrons", <i>Saas-Fee, Switzerland</i> . | school |
| 30.06-01.07.2014 | Annual Meeting of the Swiss Physical Society, <i>Fribourg, Switzerland</i> | conference |
| 01-06.06.2014 | 13 th International Conference on Muon Spin Rotation, Relaxation and Resonance, <i>Grindelwald, Switzerland</i> . | conference |
| 23.02-26.03.2014 | Higher European Research Course for Users of Large Experimental Systems "HERCULES", <i>Grenoble and Saclay, France</i> . | school |
| 17-23.08.2013 | Paul Scherrer Institut's Summer School on Condensed Matter Research "Materials-Structure and Magnetism", <i>Zuoz, Switzerland</i> . | school |

Employment history

- 10/2013-10/2017 **Ph.D in Physics**
Paul Scherrer Institut (PSI), Villigen and Department of Physics, ETH Zürich, Switzerland
Group: Laboratory for Neutron Scattering and Imaging
Doctoral advisor: Prof. Dr. Joël Mesot
Supervisors: Prof. Dr. Michel Kenzelmann, Dr. Jorge Gavilano
Swiss National Science Foundation (SNSF) grant No.: 200021_147071
- 09/2011-02/2012 **Research Traineeship**
Paul Scherrer Institut (PSI), Villigen
Group: SwissFEL-CLS
Supervisor: Prof. Dr. Cristoph Hauri
- 06/2005-01/2009 **Traineeship**
BBT SOFTWARE⁺ IT⁺INSURANCE, Zermatt, Switzerland
Supervisor: Dr. Hermann Biner

Institutional responsibilities

- 05/2015-05/2017 Co-responsible for neutron diffraction aligning instrument ORION at the Swiss Spallation Neutron Source (SINQ), Paul Scherrer Institut (PSI), Villigen, Switzerland
- 05/2015-02/2017 Ph.D representative of the Paul Scherrer Institut (PSI) at the Department of Physics, ETH Zürich, Switzerland

Supervision of junior researchers

- 04-08/2015 Co-supervision of semester project
Student: Christian Wessler
Principle supervisors: Prof. Dr. Michel Kenzelmann and Dr. Marek Bartkowiak
Title: "Heat conductivity of Pr₂Pt₃Ge₅"
- 04-09/2014 Co-supervision of master thesis
Student: Kosova Kreka
Principle supervisors: Dr. Jorge Gavilano, Dr. Wolfgang W. Schmal, Dr. Guntram Jordan
Title: "Phase transitions in Telluride Materials by Neutron and X-ray Scattering"

04-08/2014 Co-supervision of semester project
Student: Nadja Hartmann
Principle supervisor: Prof. Dr. Christan Rüegg
Title: "Powder Diffraction Studies of $\text{Pd}_x\text{Ir}_{1-x}\text{Te}_2$ "

Teaching activities

05/2015-05/2017 Teaching assistant of the practicum "The vortex lattice of a type-II superconductor studied by small angle neutron scattering (SANS)" in "Advanced Physics Lab (VP)" of the ETH Zürich, Switzerland

Active memberships in scientific societies, fellowships in renowned academies

Since 09/2017 Scientific reviewing for the American Physical Society (APS)
03-07/2015 Scientific reviewing for the peer-reviewed journal "Superconductor Science and Technology"

Memberships in panels, boards, etc., and individual reviewing activities

since 02/2017 Member of the "Swiss Neutron Scattering Society"
since 07/2016 Member of the "Swiss Physical Society"
since 10/2013 Member of the network "Materials with Novel Electronic Properties (MaNEP)"

Prizes, awards, fellowships

24.06.2017 Swiss National Science Foundation (SNSF) Early Postdoc.Mobility fellowship on "Static and time-resolved resonant inelastic X-ray scattering on strongly correlated electron systems"
01/2013 "Polya-Preis" founded by "Polya-Fonds" of the ETH Zürich
08/2008 "Moritz-Kämpfen-Stiftung" award

Research output list

Publications in peer-reviewed scientific journals

- 1) **Distinct domain switching in $\text{Nd}_{0.05}\text{Ce}_{0.95}\text{CoIn}_5$ at low and high fields.**
D. G. Mazzone, R. Yadav, M. Bartkowiak, J. L. Gavilano, S. Raymond, E. Ressouche, G. Lapertot, and M. Kenzelmann.
Sci. Rep. **8**, 1295 (2018). Also found in open source: arXiv:1709.00195 (2017).
- 2) **Spin resonance and magnetic order in an unconventional superconductor.**
D. G. Mazzone, S. Raymond, J. L. Gavilano, P. Steffens, A. Schneidewind, G. Lapertot, and M. Kenzelmann.
Phys. Rev. Lett. **119**, 187002 (2017). Also found in open source: arXiv:1705.01255 (2017).
- 3) **Field-induced magnetic instability within a superconducting condensate.**
D. G. Mazzone, S. Raymond, J. L. Gavilano, E. Ressouche, C. Niedermayer, J. O. Birk, B. Ouladdiaf, G. Bastien, G. Knebel, D. Aoki, G. Lapertot, and M. Kenzelmann.
Sci. Adv. **3**, e1602055 (2017).
- 4) **Fully gapped superconductivity in the topological superconductor $\beta\text{-PdBi}_2$.**
P. K. Biswas, D. G. Mazzone, R. Sibille, E. Pomjakushina, K. Conder, H. Luetkens, C. Baines, J. L. Gavilano, M. Kenzelmann, A. Amato, and E. Morenzoni.
Phys. Rev. B **93**, 220504(R) (2016). Also found in open source: arXiv:1606.01050
- 5) **Crystal structure and phonon softening in $\text{Ca}_3\text{Ir}_4\text{Sn}_{13}$.**
D. G. Mazzone, S. Gerber, J. L. Gavilano, R. Sibille, M. Medarde, B. Delley, M. Ramakrishnan, M. Neugebauer, L. P. Regnault, D. Chernyshov, A. Piovano, T. M. Fernandez-Diaz, L. Keller, A. Cervelino, E. Pomjakushina, K. Conder, and M. Kenzelmann.
Phys. Rev. B **92**, 024101 (2015). Also found in open source: arXiv:1503.08102
- 6) **Distinct vortex-glass phases in $\text{Yb}_3\text{Rh}_4\text{Sn}_{13}$ at high and low magnetic fields.**
D. G. Mazzone, J. L. Gavilano, R. Sibille, M. Ramakrishnan, C. D. Dewhurst, and M. Kenzelmann
J. Phys.: Condens. Matter **27**, 245701 (2015). Also found in open source: arXiv:1407.0569

- 7) **Small-angle neutron scattering study of the mixed state of $\text{Yb}_3\text{Rh}_4\text{Sn}_{13}$.**
D. Mazzone, J. L. Gavilano, R. Sibille, M. Ramakrishnan, and M. Kenzelmann
Phys. Rev. B **90**, 020507(R) (2014). Also found in open source: arXiv:1405.7712

Peer-reviewed books/monographs

- 1) D. G. Mazzone, *Vortex Lattice Studies of the Mixed State of $\text{Yb}_3\text{Rh}_4\text{Sn}_{13}$ and $\beta\text{-Bi}_2\text{Pd}$* , Master thesis, ETH Zürich and Paul Scherrer Institut, 2013.

Oral contributions to conferences and invited talks/seminars

- | | | |
|----|--|-------------------------|
| 1) | Evidence for a novel quantum phase transition.
<u>D. G. Mazzone</u> , S. Raymond, J. Gavilano, E. Ressouche, C. Niedermayer, J. O. Birk, B. Ouladdiaf, G. Bastien, G. Knepel, D. Aoki, G. Lapertot, and M. Kenzelmann.
International Conference on Neutron Scattering, <i>Daejeon, Korea</i> , 09-13.07.2017 | contributed talk |
| 2) | Discovery of a superconducting quantum critical point.
<u>D. G. Mazzone</u> , 20 years SINQ, <i>Villigen, Switzerland</i> , 18.04.2017 | invited talk |
| 3) | Evidence for a novel quantum phase transition.
<u>D. G. Mazzone</u> , Seminar, <i>Uppsala University, Sweden</i> , 03.03.2017 | invited seminar |
| 4) | Evidence for a novel quantum phase transition.
<u>D. G. Mazzone</u> , Seminar, <i>KTH Stockholm, Sweden</i> , 02.03.2017 | invited seminar |
| 5) | Possible quantum critical point in Nd-doped CeCoIn_5.
<u>D. G. Mazzone</u> , Quantum Criticality and Novel Phases 2017, <i>Berlin, Germany</i> , 27.02.2017 | invited talk |
| 6) | Evidence for a novel quantum phase transition.
<u>D. G. Mazzone</u> , Seminar, <i>Brookhaven National Laboratory, USA</i> , 03.02.2017 | invited seminar |
| 7) | Evidence for a novel quantum phase transition.
<u>D. G. Mazzone</u> , Seminar, <i>Milan, Italy</i> , 11.01.2017 | invited seminar |
| 8) | Discovery of a superconducting quantum critical point.
<u>D. G. Mazzone</u> , S. Raymond, J. Gavilano, E. Ressouche, C. Niedermayer, J. O. Birk, B. Ouladdiaf, G. Bastien, G. Knepel, D. Aoki, G. Lapertot, and M. Kenzelmann.
Annual Meeting of the Swiss Physical Society, <i>Lugano, Switzerland</i> , 23-25.08.2016 | invited talk |

- 9) **A superconducting quantum critical point at the origin of the spin-triplet pair density-wave order in the Q-phase.** invited talk
 D. G. Mazzone, FFLO-Phase in Quantum Liquids, Quantum Gases, and Nuclear Matter, *Dresden, Germany*, 23.06.2016
- 10) **Unconventional interplay between magnetism and superconductivity in $\text{Pr}_2\text{Pt}_3\text{Ge}_5$ and $\text{Nd}_{0.05}\text{Ce}_{0.95}\text{CoIn}_5$.** invited seminar
 D. G. Mazzone, Seminar in Neutron Scattering, *PSI Villigen, Switzerland*, 20.05.2016
- 11) **Discovery of a superconducting quantum critical point.** contributed talk
 D. G. Mazzone, S. Raymond, J. Gavilano, E. Ressouche, C. Niedermayer, J. O. Birk, B. Ouladdiaf, G. Bastien, G. Knepel, D. Aoki, G. Lapertot, and M. Kenzelmann.
 International Conference on Strongly Correlated Electron Systems, *Hangzhou, China*, 08-13.05.2016
- 12) **Complete decoupling of magnetic order and superconductivity in a conventional superconductor.** invited seminar
 D. G. Mazzone, Condensed Matter Theory Seminar, *Villigen, Switzerland*, 10.11.2015
- 13) **Distinct interplay between magnetism and superconductivity in $\text{Nd}_x\text{Ce}_{1-x}\text{CoIn}_5$.** contributed talk
 D. G. Mazzone, S. Raymond, J. Gavilano, E. Ressouche, G. Lapertot, and M. Kenzelmann.
 6th European Conference on Neutron Scattering, *Zaragoza, Spain*, 30.09-04.09.2015

Outreach activities

- 09/2017 Discussion with young Ph.D students of the SwedNess program about my experiences from the Ph.D.
- 09/2017 Podium discussion with students of the gymnasium Neufeld Bern during their visit at the Paul Scherrer Institut.
- 02/2017 Invited members of the "Cold atom group" at ETH Zürich for a seminar at the Paul Scherrer Institut to trigger scientific knowledge transfer.
- 12.11.2015 Accompanied and worked with the 14-year-old Lukas Schmid during the "Nationaler Zukunftstag" at the Paul Scherrer Institut (PSI).
- 18.10.2015 Contribution to the "Tag der offenen Tür am PSI" as part of the "Kleinwinkelstreuung und Reflektometrie" group.
- 10/2013-10/2017 Guided visitors around the campus of the Paul Scherrer Institut (PSI).

General contributions to science

- 03-07/2016 Contributed to a in-house heat conductance setup under the guidance of Dr. Marek Bartkowiak using the one-heater-two-thermometer method.
- 05/2015-05/2017 Co-responsible of the neutron diffraction aligning instrument ORION at the Swiss Spallation Neutron Source SINQ, PSI.
- 13-18/08/2014 Local contact on the SANS-I instrument at the Swiss Spallation Neutron Source SINQ.
- 07/2013-02/2014 Contributed to a electrical resistivity setup under the guidance of Dr. Marek Bartkowiak using pulsed electrical currents.
- 05/2013 and 2014 Contributed to the calibration of the SANS-I instrument at the Swiss Spallation Neutron Source SINQ.
- 05/2013-05/2017 Technical assistance on the beamline SANS-I at the Swiss Spallation Neutron Source SINQ for setup changes.
- 05/2013-10/2017 Main proposer of more than 35 accepted beamtime proposals at international large-scale facilities (neutron, muon and synchrotron X-rays sources).

Other artifacts with documented use

- 1) **Complete decoupling of magnetic order and superconductivity in a conventional superconductor.**
D. G. Mazzone, R. Sibille, M. Bartkowiak, J. L. Gavilano, C. Wessler, M. Månsson, M. Frontzek, O. Zaharko, J. Schefer, and M. Kenzelmann.
arXiv:1508.02649 (2015).

Manuscripts in preparation

- 1) **Detaching Magnetic Order from the Kondo Coupling.**
D. G. Mazzone, N. Gauthier, D. T. Maimone, R. Yadav, M. Bartkowiak, J. L. Gavilano, S. Raymond, V. Pomjakushin, N. Casati, Z. Revay, G. Lapertot, R. Sibille, and M. Kenzelmann.
- 2) **Foucault Pendulum in Reciprocal Space.**
D. G. Mazzone, M. Laver, J. L. Gavilano, E. M. Forgan, R. Sibille, and M. Kenzelmann.

Poster presentation at conferences

- 1) **Complete decoupling of magnetic order and superconductivity in a conventional superconductor.**
D. G. Mazzone, R. Sibille, J. Gavilano, M. Bartkowiak, M. Månsson, M. Frontzek, O. Zaharko, J. Schefer, and M. Kenzelmann.
30th Meeting of the European Crystallographic Association, *Basel, Switzerland*, 28.08-01.09.2016
- 2) **Complete decoupling of magnetic order and superconductivity in a conventional superconductor.**
D. G. Mazzone, R. Sibille, J. Gavilano, M. Bartkowiak, M. Månsson, M. Frontzek, O. Zaharko, J. Schefer, and M. Kenzelmann.
6th European Conference on Neutron Scattering, *Zaragoza, Spain*, 30.08-04.09.2015
- 3) **Distinct interplay between magnetism and superconductivity in $\text{Nd}_x\text{Ce}_{1-x}\text{CoIn}_5$.**
D. G. Mazzone, S. Raymond, J. Gavilano, E. Ressouche, G. Lapertot, and M. Kenzelmann.
11th Materials and Mechanisms of Superconductivity 2015, *Geneva, Switzerland*, 23-28.08.2015
- 4) **Complete decoupling of magnetic order and superconductivity in a conventional superconductor.**
D. G. Mazzone, R. Sibille, J. Gavilano, M. Bartkowiak, M. Månsson, M. Frontzek, O. Zaharko, J. Schefer, and M. Kenzelmann.
11th Materials and Mechanisms of Superconductivity 2015, *Geneva, Switzerland*, 23-28.08.2015
- 5) **Distinct interplay between magnetism and superconductivity in $\text{Nd}_x\text{Ce}_{1-x}\text{CoIn}_5$.**
D. G. Mazzone, S. Raymond, J. Gavilano, E. Ressouche, G. Lapertot, and M. Kenzelmann.
20th International Conference on Magnetism, *Barcelona, Spain*, 05-10.07.2015
- 6) **A neutron scattering study of the mixed state of $\text{Yb}_3\text{Rh}_4\text{Sn}_{13}$.**
D. G. Mazzone, J. Gavilano, R. Sibille, M. Ramakrishnan, and M. Kenzelmann.
Annual Meeting of the Swiss Physical Society, *Fribourg, Switzerland*, 30.06-01.07.2014
- 7) **Study of the superconducting state of $\beta\text{-Bi}_2\text{Pd}$.**
D. G. Mazzone, J. Gavilano, R. Sibille, C. Baines, and M. Kenzelmann.
13th International Conference on Muon Spin Rotation, Relaxation and Resonance, *Grindelwald, Switzerland*, 01-06.06.2014

- 8) **Phase transitions in ternary intermetallic stannides.**
D. G. Mazzone, J. Gavilano, R. Sibille, S. Gerber, M. Bartowiak, M. Ramakrishnan, M. Medarde, E. Pomjakushina, D. Chernyshov, L-P. Regnault, T. Fernandez-Diaz, and M. Kenzelmann.
Higher European Research Course for Users of Large Experimental Systems "HERCULES", *Grenoble and Saclay, France*, 23.02-26.03.2014
- 9) **Phase transitions in ternary intermetallic stannides.**
M. Ramakrishnan, D. Mazzone, J. L. Gavilano, R. Sibille, S. Gerber, M. Medarde, E. Pomjakushina, D. Chernyshov, L. P. Regnault, T. Fernandez-Diaz, and M. Kenzelmann.
PSI's Summer School on Condensed Matter Research "Materials-Structure and Magnetism", *Zuoz, Switzerland*, 17-23.08.2013